DUAL-MODALITY PHOTOACOUSTIC AND ULTRASOUND IMAGING FOR MURINE ATHEROSCLEROSIS CHARACTERIZATION

by

Gurneet S. Sangha

A Dissertation

Submitted to the Faculty of Purdue University

In Partial Fulfillment of the Requirements for the degree of

Doctor of Philosophy

Weldon School of Biomedical Engineering

West Lafayette, Indiana

December 2019

THE PURDUE UNIVERSITY GRADUATE SCHOOL
STATEMENT OF COMMITTEE APPROVAL

Dr. Craig J. Goergen, Chair

Weldon School of Biomedical Engineering

Dr. Young L. Kim

Weldon School of Biomedical Engineering

Dr. Keith M. Stantz

School of Health Sciences

Dr. Johnathan D. Tune

School of Medicine, Indiana University

Approved by:

Dr. George R. Wodicka

To my mother Preetinder Kaur and father Rattan S. Sangha;
per aspera ad astra

ACKNOWLEDGMENTS

First and foremost, I would like to express my deepest gratitude to my advisor Dr. Craig J. Goergen. Thank you for cultivating curiosity, confidence, and creativity. I also am grateful for all the support and constructive criticism provided by the members of the CardioVascular Research Imaging Laboratory, as well as the undergraduate student's that I have been fortunate to mentor over the past five years. The motivation and drive all of all these people have helped me develop into a better researcher and individual.

The time and effort provided by my mentors and collaborators has also been invaluable. I would also like to thank my very first mentor Mr. Raymond Bangs, as well as my undergraduate advisors Drs. Laura Fabris, William Craelius, and Timothy McGuire. Thank you for instilling the initial seeds of scientific curiosity in me. I would also like to extend my gratitude to my thesis committee members Drs. Young Kim, Keith M. Stantz, and Johnathan M. Tune and research collaborators Drs. J. Quincy Brown, Albert Busch, Ji-Xen Cheng, and Alyssa Panitch for all of their scientific feedback regarding my work

Completion of this dissertation would not be possible without the help my family and some close friends. Dr. Katherine N. Clayton, Dr. Richard Lie, and (soon to be Dr.) Samarth Mathur have all kept me laughing throughout graduate school; I will forever cherish our scientific and philosophical discussions. My powerlifting training partners Val Schull, David Wieten, and all the members of Purdue Barbell have provided me a sense of community and have pushed me to be better both mentally and physically. Lastly, but certainly not least, the culmination of this work would not be possible with the love and support of my family; especially my mother Preetinder Kaur who has instilled the quality of tenacity and determination in me.

I am particularly grateful to the Rutgers Educational Opportunity Fund and Ronald E. McNair Scholar programs for preparing me for graduate school, as well as my funding sources from the NIH T32 Diabetes Training Grant and National Science Foundation Graduate Research Fellowship Program.

PREFACE

Chapters one through four of this dissertation have been published in peer-reviewed journals and chapter five is currently under preparation. Moreover, chapters one, three, four, and five of this dissertation focuses on advancements in photoacoustic tomography and chapter two focuses on the capabilities of ultrasound imaging for cardiovascular disease characterization. Photoacoustic topics in these chapters include a review of the literature for atherosclerosis imaging (Chapter 1), *in vivo* methods for murine lipid imaging (Chapter 3), instrument development for penetration depth improvement, (Chapter 4) and a comprehensive study of murine atherosclerosis progression (Chapter 5). Please see publication section for a comprehensive list of published journal articles and their scientific impact. Finally, minor wording edits have been made to the published manuscript text for nomenclature consistency throughout the dissertation.

TABLE OF CONTENTS

LIST OF FIGURES 10
ABSTRACT 18
1. INTRODUCTION 19
2. CURRENT APPLICATIONS IN ATHEROSCLEROSIS PHOTOACOUSTICS 21
2.1 Abstract 21
2.2 Introduction 22
2.3 Methods of Literature Review 23
2.4 Discussion of Literature 23
2.4.1 Atherosclerosis Progression 23
2.4.2 Current Diagnostic Techniques 25
2.4.3 Photoacoustic Imaging 33
2.5 Preclinical and Clinical Directions 42
2.6 Conclusion 43
2.7 Acknowledgement 44
3. ULTRASOUND CAPABILITIES FOR MURINE VASCULAR IMAGING 45
3.1 Abstract 45
3.2 Introduction 46
3.3 Materials and Methods 47
3.3.1 Elastase Infusion Surgery 47
3.3.2 Ultrasound Imaging 48
3.3.3 3D Segmentation and Centerline Deviation Quantification 49
3.3.4 Histology, Gene Expression, and Immunohistochemistry Experiments 49
3.3.5 Human AAA Tissue Acquisition 50
3.3.6 Statistical Analysis 50
3.4 Results 50
3.4.1 Morphological Changes in Murine PPE-infused Aortae 50
3.4.2 Murine Histology, Gene Expression, and Immunohistochemistry 54
3.4.3 Human AAA Centerline, Histology, and Immunohistochemistry 57
3.5 Discussion 58

3.6 Conclusion 61
3.7 Acknowledgments 62
4. PHOTOACOUSTIC METHODOLOGY FOR IN VIVO LIPID IMAGING 63
4.1 Abstract 63
4.2 Introduction 64
4.3 Materials and Methods 65
4.4 Results 67
4.5 Discussion 69
4.6 Conclusion 71
4.7 Acknowledgements 71
5. OPTIMIZATION OF PHOTOACOUSTIC IMAGE QUALITY 72
5.1 Abstract 72
5.2 Introduction 72
5.3 Methods 75
5.3.1 Photoacoustic Tomography System Design 75
5.3.2 Photoacoustic Tomography Fiber-Adjusting Apparatus Design 75
5.3.3 Monte Carlo Multilayer Simulation Study 76
5.3.4 *Ex Vivo* Validation Study 78
5.3.5 *In Vivo* Validation Study 79
5.3.6 Photoaccoustic Reflection Artifact Removal 79
5.3.7 Statistical Analysis 80
5.4 Results 80
5.4.1 Monte Carlo Simulation Results 80
5.4.2 *Ex vivo* Validation Results 81
5.4.3 *In vivo* Validation Results 82
5.4.4 Photoacoustic Reflection Artifact Removal Results 83
5.5 Discussion 84
5.6 Conclusion 88
5.7 Acknowledgment 88
6. PHOTOACOUSTIC TOMOGRAPHY FOR MURINE ATHEROSCLEROSIS 89
6.1 Abstract 89

6.2 Introduction 91
6.3 Methods 92
6.3.1 Photoacoustic Tomography System Specifications 92
6.3.2 Photoacoustic Tomography Resolution Characterization 92
6.3.3 Small Animal Atherosclerosis Induction 93
6.3.4 Murine Atherosclerotic Plaque Lipid Burden Validation 93
6.3.5 Cross-Sectional Photoacoustic and Longitudinal Ultrasound Plaque Assessment 94
6.3.6 Statistical Analysis 97
6.4 Results 98
6.4.1 Photoacoustic Tomography Resolution Characterization 98
6.4.2 *Ex Vivo* Carotid Artery Lipid Burden Results 98
6.4.3 Hemodynamic and Kinematic Characterization Results 99
6.4.4 Morphological and Compositional Characterization Results 101
6.4.5 Histology 103
6.5 Discussion 104
6.6 Conclusions 108
6.7 Acknowledgements 109
7. CONTRIBUTIONS TO SCIENTIFIC KNOWLEDGE 110
8. FUTURE WORK 111
APPENDIX A 114
APPENDIX B 123
PUBLICATIONS 152

LIST OF TABLES

Table 2.1: Sensitivity and specificity range for clinically relevant diagnostic techniques for atherosclerosis detection. 27

Table 2.2: Summary of advantages and disadvantages of clinically adopted, optical, and PA techniques in the diagnosis of atherosclerosis-related disease. Table adopted and modified from Lin et al. [21] 30

Table 2.3: Summary of currently available nanoparticles for PA imaging, their targets, and implications for atherosclerosis imaging. 40

Table 4.1: Summary of the Characteristics for Experimental Mouse Groups 65

Table 5.1: Summary of optical properties and geometry of the simulated water and PVA. τ denotes calculated value. 78

Table 6.1: Summary of experimental animal groups and ultrasound imaging timepoints. Light blue box, dark blue box, and E denote ultrasound, PAT, and euthanize timepoints, respectively. 95

Appendix A Table 1: Summary of iliac artery mean velocities for the standard PPE, as well as modified left and right PPE groups at day 56. Standard PPE group shows slightly greater and more variable mean velocities in the left and right iliac arteries. 120

Appendix A Table 2: Day 28 and 56 centerline deviation results showing magnitude and direction of AAA growth in standard PPE, as well as left and right modified PPE groups. 120

LIST OF FIGURES

Figure 2.1: Early Type I-IV plaque progression of atherosclerosis beginning with endothelial dysfunction and ending with lipid core formation. Figure adapted and modified from Lin et al.[21] 24

Figure 2.2: A gray-scale long-axis ultrasound image of the distal common carotid artery (left). Calcification (arrowhead) and plaque (arrow) can be clearly visualized within the artery. A short-axis ultrasound image of the distal common carotid artery (right). The more lucent plaque (arrow) is typically associated with higher risk of plaque rupture. Figure adapted from Lee et al. [29] 26

Figure 2.3: A) Coronary CTA maximum intensity projection images reveal plaque in proximal segment of left anterior descending artery (LAD) with calcification (white arrow). B) Volume rendering show plaque accumulation in proximal segment of LAD (black arrow). C) Maximum intensity project show calcified plaque in proximal segment of LAD. D) CTA image clearly shows severe stenosis in coronary artery (black arrow). (E) DSA and (F) MRA images of stenotic proximal iliac artery, shown by black and white arrows. Subfigure A-D adapted from Yorgun et al. [40] Subfigures C and D are adapted from Ruehm et al.[41] 28

Figure 2.4: Schematic of in vivo plaque imaging. Bifurcated fiber optic bundles deliver light to plaque to induce acoustic waves that are detected by an ultrasound transducer. 34

Figure 2.5: *In vivo* IVPA/IVUS imaging in Watanabe heritable hyperlipidemic rabbit abdominal aorta. (A) PA imaging was able to provide lipid characterization, (B) while ultrasound provided structural information. By overlaying these two images plaque accumulation can be resolved within the intimal layer. Figure adapted from Wang et al. [99]. 38

Figure 2.6: In vivo PA image angiogenesis visualized by utilizing $\boldsymbol{\alpha v \beta 3}$ targeted copper nanoparticles. Significant PA signal can be seen between targeted (A-B) and non-targeted (C-D) groups at time 0 and 170 minutes (yellow arrows). A competition group (E-F) was given $\boldsymbol{\alpha v \beta 3}$-oil only nanoparticles 10 minutes prior to imaging and $\boldsymbol{\alpha v \beta 3}$-CuNP directly before imaging. Fumagillin prodrug (Fum-PD) group (G-H) was given both $\boldsymbol{\alpha v \beta 3}$-CuNP and fumagillin prodrug 11 and 15 days after Matrigel implantation and $\boldsymbol{\alpha v \beta 3}$-CuNP before imaging. There is little change in PA single between non-targeted, competition, and fumagillin-prodrug images. PA images were taken using 767nm wavelength. Figure adapted from Zhang et al.[127]. 41

Figure 3.1: Representative healthy (left panels) and aneurysmal (right panels) murine aortae with B-mode (A-B), M-mode (C-D), and PWD (E-F) images. B-mode images were used to assess overall vessel structure and quantify increase in aortic diameter after PPE treatment. M-mode was used to measure circumferential cyclic strain, and PWD was used to quantify mean and peak velocities. 48

Figure 3.2: Summary of structural changes in murine abdominal aortic aneurysm development among standard, left, and right PPE groups. Long-axis B-mode was used to quantify aortic diameter (A), 3D ultrasound for aortic segmentation and volume characterization (B), and M-mode to quantify systolic and diastolic diameters (C) that were used to assess changes in circumferential cyclic strain. Aortic diameter increases steadily up to day 56 (D) with the modified PPE group having rapid increase in volume/length up to day 7 (E). We also observed a

sharp decrease in circumferential cyclic strain between baseline and day 7 post-procedure time points (F). Representative short-axis ultrasound, 3D segmentation, and volume showed slightly larger aneurysm in the modified PPE group compared to the standard PPE group (G). Statistical significance compared with day 0 and defined at $p<0.05$ (*), $p<0.01$ (&), and $p<0.001$ (#). Blue asterisk represents statistical significance between the standard and modified PPE groups. Scale bar denotes 200 μm. 52

Figure 3.3: Comparison of structural and hemodynamic changes between non-ligated (A) and partially ligated (B) iliac arteries at day 56. We observed significant decrease in diameter (C) and circumferential cyclic strain (E) in modified iliac arteries compared to standard PPE arteries and contralateral control iliac arteries. We did not, however, see significant changes in iliac artery velocity between standard and modified PPE groups at day 56 (D). Suture placement is highlighted by white arrow and diameter measurement locations shown by blue lines. Statistical significance is shown as $p<0.001$ (α, β, γ, δ, ε, ζ). Symbols α, β, γ signify statistical significance between their respective group and the standard, modified control, and modified partial ligation groups in the proximal iliac artery. 53

Figure 3.4: Summary of murine centerline deviation analysis methods and results. Aneurysm and projected healthy regions were first segmented using SimVascular (A). We then used short-axis view (B) to quantify magnitude (C) and direction (D) of centerline deviation between the healthy and diseased aorta. Centerline deviation results (E) for day 28 and 56 shows the shift in magnitude and direction of the diseased vessels with respect to the healthy vessel. Red points represent the mean centerline deviation for the standard and modified PPE groups, and the red lines represent the standard deviation in the X and Y axis. Cr: Cranial, Ca: Caudal, L: Left, R: Right, A: Anterior, P: Posterior. 54

Figure 3.5: Histological and immunohistochemistry analysis of PPE infused aortic tissue consisting of EvG stained standard (A,C) and modified (B,D) aortae, as well as Ki67 stained modified (F) infrarenal aorta. Histology showed diffuse elastin breakage throughout the vessels (yellow arrows), thus confirming aneurysm induction. Ki67 staining revealed cell proliferation in the modified PPE animals (white arrows). Further, cell number analysis showed significant increase in cell nuclei (red arrows) between the modified and standard PPE infused aortae (E). A: Anterior, P: Posterior, L: Left, R: Right. Scale bar A, C, F denotes 100 μm, and B and D denotes 50 μm. Statistical significance is defined at $p<0.05$ (*), $p<0.001$ (#), $p<0.0001$ (~)..... 55

Figure 3.6: Relative gene Expression analysis of standard and modified infrarenal aortae at day 56 using qPCR. IL-6 (A) and VEGFA (B) are upregulated, but there are no significant differences between PPE infused and control aortae. TGFβ1 shows significant upregulation between PPE infused and control aortae, and standard and modified groups (C); while KLF4 (D) shows variable differences in expression between standard and modified groups. Fold change values are relative to control aortae. Statistical significance is defined at $p<0.05$ (*), $p<0.001$ (#), and $p<0.0001$ (~)..... 56

Figure 3.7: Summary of human centerline deviation analysis methods and results. 3D segmentation was performed on human AAA (A) and sagittal cross-sectional plane was used to confirm quality of 3D segmentation with red, white, and yellow highlighting AAA wall, AAA lumen, and projected healthy aorta (B). Transverse cross-sectional plane along the center of the AAA (green dotted line) was used to quantify magnitude and direction of centerline deviation (C). Quantitative analysis shows that standard and modified AAA grew away from the spine in

the leftward direction, likely due to the natural leftward origin of the healthy aorta. Red points represent the mean centerline deviation for the standard and modified PPE groups, and the red lines represent the standard deviation in the X and Y axis. Cr: Cranial, Ca: Caudal, L: Left, R: Right, A: Anterior, P: Posterior. 58

Figure 4.1: Schematic depicting PAT setup. Nd:YAG OPO laser delivered light through a fiber optic bundle to an anesthetized mouse. A 40 MHz center frequency transducer was used to acquire the resulting PAT signal. A function generator coordinated pulse excitation and image acquisition between the laser and the Vevo2100 ultrasound system. A pulse generator was used to synchronize the trigger of the laser with the ultrasound system. The ultrasound transducer face is 20x5 mm and fiber optic bundle face is 12x2 mm. 66

Figure 4.2: Ultrasound (left), lipid PAT (middle), and blood PAT (right) images of adult male apoE$^{-/-}$ (top) and WT (bottom) mice. Images are shown such that the animals are orientated in supine position with the head located to the left and tail is located to the right. Greater periaortic fat signal is evident in the apoE$^{-/-}$ mouse compared to the WT mouse. Using these images we can clearly discriminate the infrarenal aorta (red dotted outline), subcutaneous fat (white arrows), periaortic fat (orange arrows), and blood (red arrows). 67

Figure 4.3: Averaged PAT image (1210 nm) reveals subcutaneous and periaortic fat (A). Histogram of PAT pixel intensities shows peaks for background and lipid signal (B). Gray arrow represents threshold point used to create PAT mask, which is overlaid on the original PAT image to confirm thresholding accuracy (C). Plot profile analysis was used to measure periaortic thickness at multiple locations (D). Width of top peak (SV) represents subcutaneous and visceral fat and width of bottom peak (P) represents periaortic fat from one plot profile measurement (E). ORO staining on excised aorta confirms periaortic fat accumulation (F). 68

Figure 4.4: Three representative raw 1210 nm PAT measurement images (A-C) and mean (D) image of an apoE$^{-/-}$ mouse. Measurements were taken in same location in all images. 69

Figure 4.5: Periaortic thickness values in apoE$^{-/-}$ and WT groups. Adult male apoE$^{-/-}$ mice have significantly higher periaortic thickness compared to other groups ($p<0.05$). 69

Figure 5.1: Exploded (A), presentation (B), and constructed (C) images of the PAT holder. Fabricated parts shown in silver, 3D printed parts shown in black, and commercially available parts shown in gold. PAT holder specifically consists of motors for translation of ultrasound transducer (1), and rotation of fiber optic bundles (2). Scale bar represents 1 cm. 76

Figure 5.2: MCML Simulation Results: MCML geometry (A) was created with two 18mm x 2mm fiber bundle terminals that produced 100 random rays at 1064 nm with power of 0.15 W to model light interaction through 3 mm of water bath and 20 mm of PVA (B). Depth-dependent simulation showed exponential decrease in radiant flux with higher fluence at orientations of 0º, 15º, and 30º compared to 45º and 60º (C). Image acquisition plane measurements at five locations showed greatest radiant flux at 30º and the lowest radiant flux at 0º and 60º (D). Statistical significance is shown at $p < 0.05$ (α) and $p < 0.01$ (#, Λ, λ, β, ε, X). Inset A: Top view of the MCML 20% PVA simulation geometry. 81

Figure 5.3: *Ex vivo* Validation Results: Seven freeze-thawed cycled 20% PVA phantom embedded with six PE-50 tubes was imaged using ultrasound and PAT with focal lengths of 2 mm, 3 mm, 5 mm, and 7 mm (A). Three imaging locations were selected from the depth-

profiling phantom to ensure measurement consistency (B). PE-50 tubes are highlighted with purple dotted circles in the ultrasound image. Quantitative results show that we observe better SNR for superficial PE-50 tubes using focal length of 2 mm and 3 mm, and improved contrast for deeper PE-50 tubes using focal length of 5 mm and 7 mm (C). Red dotted line signifies greatest SNR for superficial tubes and blue line signifies greatest SNR for the deeper tubes. Yellow and red arrows signify reflection and motor induced artifacts, respectively. 82

Figure 5.4: *In vivo* Validation Results: Subcutaneous fat and infrarenal periaortic fat were imaged in apoE$^{-/-}$ mice to show increased PAT signal intensity when tuning focal length from 7 mm to 2 mm (A). We observed an increased SNR in the subcutaneous fat (yellow arrow) and periaortic fat (red arrow). The infrarenal aorta is outlined in red dotted line. Quantitative assessment shows statistically significant ($p < 0.05$) increase in subcutaneous SNR of 77% (B), and statistically significant ($p<0.05$) increase in periaortic SNR of 62% (C). Statistical is significance shown at $p < 0.05$ (*). 83

Figure 5.5: Schematic of reflection artifact (A) showing how light reflects off of the optical reflector and induces a photoacoustic effect at the PAT probe face. This PAT signal then travels distance *d* down towards the acoustic reflector and travels another distance *d* up towards the ultrasound transducer. The PAT system, therefore, registers the acoustic wave as traveled 2*d*, creating an artifact that can obscure image quality. The reflection artifact is effectively eliminated when a light-blocking aluminum filter is applied to the transducer face (B) as shown by the ultrasound (top left), PAT without filter (top right), and PAT with 4 μm (bottom left) and 7 μm (bottom right) filter images. Quantitative SNR assessment shows slight decrease in SNR when utilizing aluminum filters (C). The infrarenal aorta is highlighted by the red dotted lines, the periaortic signal by the orange arrows, and the reflection artifact by the red arrow. 84

Figure 6.1: Axial (A) and lateral (B) profile of PAT signal amplitude using 20% PVA with five embedded 50 μm tungsten wires. Depth profiling resolution measurements with 1210 nm light revealed axial resolution of 48±8 μm and lateral resolution of 243±11 μm (C). Insets in A and B show PAT images of tungsten wire and profile measurement location (white dotted line). 98

Figure 6.2: Validation of PAT to quantify lipid burden in a murine model of atherosclerosis. Lipid accumulation in mice that underwent a PCL varied greatly between animals as shown by ORO stained histology (A-C). Comparison of gross (D) and PAT (E) LCA (red dotted line) shows adequate spatial correlation of lipid signal. Suture is highlighted by yellow arrow. Plaque lipid composition did not vary significantly between 2 and 6±1.7 weeks post-PCL procedure regardless of sex (F). Linear regression statistics of plaque lipid composition versus lipid specific PAT SNR showed positive correlation (R^2=0.72, n=27, p<0.001; G). Scale bar A-C, Inset E: 100 μm, E: 1mm. 99

Figure 6.3: Hemodynamic characterization of LCA mean velocities between day 0 (A) and days 1 through 14 post-PCL (B) reveals statistically significant decrease in antegrade blood flow (D) and increase in retrograde blood flow (E). Proximal regions (R4 and R5) had statistically greater antegrade and retrograde velocities compared to distal regions (R1 and R2) until day 7, as well as a steady decrease in overall velocity until day 14. Conversely, the contralateral control RCA revealed healthy pulsed wave Doppler (C) and antegrade flow velocities (F) over 14 days. Statistical significance: p<0.05 (= significance compared to all other days in same region, † = significance compared to the same day in region 1, • = significance compared to the same day in region 2, ∧ = significance compared to day 1 in the same region, # = significance compared to

day 4 in the same region, & = significance compared to day 7 in the same region, and ¥ = significance compared to day 10 in the same region). 100

Figure 6.4: Representative 3D images of maximum first-principal Green-Lagrange strain in the LCA post-PCL (A-C) and the contralateral control RCA (E-G). Regional assessment of strain in the LCA (D) suggest decrease in vessel pulsatility after suture placement at day 1 followed by steady decrease until day 7. Strain measurements in the RCA suggest healthy vessel pulsatility. Strain values were overlaid on segmented volumes for visualization. Statistical significance determined at $p<0.05$ (= significance compared to all other days in same region, $ = significance compared to day 0 in the same region, ∧ = significance compared to day 1 in the same region, and # = significance compared to day 4 in the same region). Scale bar: 1mm. 101

Figure 6.5: Morphological characterization of LCA between days 0 (A) and 14 (B) suggests heterogeneous remodeling response due to PCL until day 7, followed by rapid reduction of both volume/length (E) and diameter (F). Moreover, statistically significant increase in RCA volume/length (G) and increase in diameter (H) from day 0 (C) through day 14 (D) suggests compensatory remodeling due to LCA stenosis. Statistical significance determined at $p<0.05$ (* = significance between groups, $ = significance compared to day 0 in the same region, ∧ = significance compared to day 1 in the same region, # = significance compared to day 4 in the same region, & = significance compared to day 7 in the same region, and ¥ = significance compared to day 10 in the same region). Scale bar: 1mm. 102

Figure 6.6: Representative *in situ* ultrasound (A-C), 1100 nm PAT (D-F), and 1210 nm PAT (G-I) images of LCA at days 7, 10, and 14 post-PCL. Regional assessment of lipid specific PAT SNR (G) and PAT lipid volume (H) suggests statistically significant and rapid lipid accumulation between days 7 and 14, with greater lipid accumulation in the proximal most regions at day 14. Comparison of the lipid volume and lumen volume/length suggests compensatory remodeling of the LCA until day 10, potentially due to Glagov remodeling, followed by rapid decrease in lumen volume and increase in lipid volume. Statistical significance determined at $p<0.05$ (* = significance between groups, † = significance compared to the same day in region 1, # = significance compared to day 4 in the same region, & = significance compared to day 7 in the same region, ⊗ = significance compared to sham group, ⊕ = significance compared to right contralateral control RCA). Scale bar: 1mm. 103

Figure 6.7: Histology and macrophage immunohistochemistry of day 7, 10, 14 post-PCL and sham groups, as well as contralateral control RCA. Staining consisted of H&E (A-E), ORO (F-J), Movat's pentachrome (K-O). Macrophage infiltration was assessed with F4/80 immunohistochemistry (P-T) and revealed rapid inflammation between days 4 and 10 (U). LCA measurements showed a 46.1% greater outer wall diameter in day 14 post-PCL compared to sham mice (V). Statistical significance determined at $p<0.05$. Scale bar: 100 μm. 104

Appendix A Figure 1: Summary of PPE infusion procedure. Aorta and inferior vena cava were first exposed (A) and separated. 6-0 silk sutures were then placed to temporarily ligate branching vessels and infusion inlet and outlet zones, and permanently placed to partially ligate the iliac artery (B). Catheter was placed in the aorta via aortotomy (C) for 10-minute elastase infusion. Aortotomy was then closed using 10-0 suture, temporary sutures are removed, and single iliac artery was partially ligated (D). Cr: Cranial, Ca: Caudal, L: Left, R: Right. Scale bar denotes 2mm……113

Appendix A Figure 2: Overview of ultrasound imaging procedure. Mice were anesthetized and placed on a heated stage where heart rate, respiration, and temperature are closely monitored to ensure animal safety. Ultrasound probe was appropriately placed on the animal to minimize artifacts due to suture and intestinal gas. After ensuring proper anesthesia induction, ultrasound imaging was performed to obtain structural and hemodynamic information……..114

Appendix A Figure 3: Comparison of aortic volume (A), volume/length (B), and normalized diameter (C) changes over 56 days between the standard and modified PPE groups. Both volume and volume/length reveal rapid aneurysm growth over the first seven days post-PPE infusion. Normalized aortic diameter shows steady AAA growth up to day 56. Statistical significance compared with day 0 and defined at $p<0.05$ (*), $p<0.01$ (&), and $p<0.001$ (#). Blue asterisk represents statistical significance between the standard and modified PPE groups at day 7……...118

Appendix A Figure 4: Morphological, kinematic, and hemodynamic changes in infrarenal aorta, and left and right iliac arteries due to PPE infusion and partial iliac ligation. Diameter measurements show gradual increase in AAA size up to day 56, with volume/length showing rapid aneurysm expansion in the first seven days. Circumferential cyclic strain measurements reveal rapid decrease in aortic pulsatility post-PPE infusion for all animals. Overall, infrarenal aorta, and modified left and right PPE velocities decrease after surgical AAA induction and partial iliac ligation, respectively by day 56. Statistical significance defined at $p<0.05$ (*), $p<0.01$ (&), and $p<0.001$ (#)…….……...119

Appendix A Figure 5: Histological and immunohistochemistry analysis of PPE infused aortic tissue. H&E stained standard (A) and modified (B) PPE aortae showed vessel wall thickening compared to control aortae (C). Ki67 staining confirmed cell proliferation (white arrow) in standard (D) and modified (E) aortae compared to control aortae (F). Immunohistochemistry revealed TGFβ1 expression (yellow arrows) in standard (G,J) and modified (H,K) animals compared to control animals (I,L). A: Anterior, P: Posterior, L: Left, R: Right. Scale bar denotes 100 μm…….120

Appendix A Figure 6: Computed tomography imaging of two AAA patients, one with a left common iliac occlusion (A) and one with a right leg amputation (F), reveals asymmetrical aneurysm formation. Closer examination with H&E staining shows signs of increased cellular infiltration on the left side of the AAA in both the modified left (B) and right (G) iliac outflow. EvG staining reveals widespread destruction of elastin laminar units (C,H). High resolution images of elastin destruction are shown in the EvG insets with the location of the inset shown in black dotted boxes. Cellular infiltrate was primarily comprised of inflammatory cells via CD34 (red arrows; D, I) and CD45 (yellow arrows; E, J) immunohistochemistry. Cr: Cranial, Ca: Caudal, L: Left, R: Right, Av: adventitia, Lu: Lumen. Scale bar denotes 200 μm……..…..121

Appendix B Figure 1: Summary of PCL procedure and representative gross images post-PCL. The LCA was first exposed and the internal (red arrow) and external (orange arrow) carotid artery, as well as the occipital (red arrow) and superior thyroid artery (yellow arrow) were identified (A). A 6-0 black braided silk suture was then placed around the internal and occipital carotid arteries, as well as the external carotid artery (B) and tied off to redirect flow into the superior thyroid artery (C). Gross images of the LCA (D-E) revealed robust plaque accumulation as early as day 10 followed by aggressive lipid lesions by day 14. Scale bar: 1mm……..123

Appendix B Figure 2: Hemodynamic changes in the sham and experimental groups post-PCL. The sham group showed a decrease in LCA and RCA velocities as the mice recover from the surgery. Experimental group peak velocities are comparable to mean velocities that are also shown in Figure 3. Statistical significance determined at $p<0.05$ (★ = significance compared to all other days in same region, † = significance compared to the same day in region 1, • = significance compared to the same day in region 2, ∧ = significance compared to day 1 in the same region, # = significance compared to day 4 in the same region, and & = significance compared to day 7 in the same region). 124

Appendix B Figure 3: Mean velocity, strain, diameter, and volume/length changes in both the LCA and RCA in the sham group. These metrics were fairly consistent when comparing baseline and day 14 data. Statistical significance determined at $p<0.05$ († = significance compared to the same day in region 1, $ = significance compared to day 0 in the same region, ∧ = significance compared to day 1 in the same region, # = significance compared to day 4 in the same region, and & = significance compared to day 7 in the same region)..... 124

Appendix B Figure 4: Day 4 strain data in the LCA (A) and RCA (B) post-PCL showed comparable values with and without WD feeding. H&E (C-D), ORO (E-F), Movat's pentachrome (G-H) staining, as well as F4/80 immunohistochemistry revealed no signs of vessel stenosis or inflammation. Statistical significance determined at $p<0.05$ (★ = significance compared to all other days in same region, • = significance compared to the same day in region 2). Scale bar: 100 μm. 125

Appendix B Figure 5: Strain comparison between the DDE and conventional MMode analysis for LCA and RCA. The DDE method shows similar trend in the LCA with large decrease in pulsatility between days 0 and 4. Statistical significance determined at $p<0.05$ (★ = significance compared to all other days in same region, $ = significance compared to day 0 in the same region, ∧ = significance compared to day 1 in the same region, and # = significance compared to day 4 in the same region)..... 126

Appendix B Figure 6: Volume changes in the LCA and RCA post-PCL. We observed a decrease in LCA volume after day 7, and a gradual increase in RCA volume throughout the 14 day study in the PCL group. The sham group did not show changes in carotid artery volumes.126

Appendix B Figure 7: Quantitative 1100nm PAT lipid distribution along carotid artery for day 7 (A), 10 (B), 14 (C), RCA (D), and sham carotid arteries (E). Individual animal data points plotted in gray. 127

Appendix B Figure 8: Quantitative 1210 nm PAT lipid distribution along carotid artery for day 4 (A), 7 (B), 10 (C), 14 (D), RCA (E), and sham carotid arteries (F). Individual animal data points plotted in gray. 127

Appendix B Figure 9: Individual mouse weights for day 4, 7, 10, 14 post-PCL groups, as well as the sham group. On average, we observed a decrease in weight after the surgical procedure followed by gradual increase in weight through the course of the study. Statistical significance determined at $p<0.05$ and compared to baseline..... 128

Appendix B Figure 10: Representative magnified H&E (A-D), ORO (E-H), Movat's pentachrome (I-L) staining, as well as F4/80 immunohistochemistry (M-P). Scale bar: 100 μm 128

ABSTRACT

Atherosclerosis accounts of 50% of the deaths in the western world leading to a plethora of diseases that include myocardial infarction, stroke, and peripheral artery disease. Currently available imaging modalities have inherent limitations, including ionizing radiation, lack of compositional information, and difficulty acquiring volumetric data that constrain their use in studying cardiovascular disease. Photoacoustic Tomography (PAT) has emerged as a promising modality that could address these limitations to improve the characterization and diagnosis of atherosclerosis-related conditions. Non-ionizing pulsed laser light is delivered to tissue leading to thermoelastic expansion followed by propagation of a pressure transient that can be detected with an ultrasound transducer. The magnitude of the ultrasonic PAT signal is proportional to the optical absorption at that location, revealing physiologically relevant compositional information of the tissue. The objective of this work is to therefore develop advanced volumetric imaging techniques to characterize disease progression in a murine model of atherosclerosis. The novelty of this work lies in the methodology and validation presented towards characterization of small animal vascular lipid accumulation with a high-resolution PAT system that utilizes the second near-infrared window (1100-1300nm). Additionally, we utilized *in situ* PAT to cross-sectionally assess lipid deposition and *in vivo* ultrasound to longitudinally assess hemodynamic, kinematic, and morphological changes during atherosclerosis progression. Together, this dissertation lays the foundation towards utilizing dual-modality PAT and ultrasound for various applications including understanding atherosclerosis pathophysiology, evaluation of novel therapeutics, and translation of clinically relevant techniques.

1. INTRODUCTION

Atherosclerosis is a progressive, chronic disease characterized by arterial plaque accumulation and possible rupture that can interrupt blood flow, contributing to an array of conditions including cerebral, carotid, coronary, and peripheral artery disease. While advancements have been made to decrease atherosclerosis prevalence, there still remains room for substantial improvements in the diagnosis and treatment of high-risk patients. For instance, there are limited techniques that can rapidly and cost-effectively diagnose and monitor patients who are at risk of developing rupture-prone plaques. Advanced imaging modalities can also be used to study small animal plaque development to better understand atherosclerosis progression. Mice, in particular, are advantageous for research purposes due to their rapid reproduction and maturation rates, low cost, and utility in mimicking various aspects of human disease pathophysiology through genetic and surgical manipulation. Taken together, this highlights the need to develop advanced imaging techniques to understand atherosclerosis pathophysiology and improve the treatment of cardiometabolic prone patients.

Currently, available clinical techniques provide robust morphological, and in some cases, hemodynamic information that can be useful in assessing lesion phenotype.[1; 2] These techniques, however, generally lack compositional information that can be useful in identifying vulnerable plaques.[1; 2] Optical techniques, on the other hand, provide high-resolution compositional information but lack the depth of penetration and field of view to characterize large areas of the vasculature.[1] Overall, these limitations reduce the potential of imaging strategies to improve human atherosclerosis characterization, novel therapeutic development, and general knowledge of lesion progression, creating a need for rapid, label-free, volumetric compositional imaging.

Photoacoustic Tomography (PAT) has emerged as a promising technique to complement currently available clinical and optical modalities. This technique utilizes pulsed laser light induced pressure transient to reconstruct spatially relevant compositional images of tissue. The advantage of this approach is that the wavelength of light can be tuned to target specific biological components. PAT can also be coupled with ultrasound to obtain morphological, hemodynamic, and compositional information of the tissue, thus making this dual-modality imaging approach a potential method for intravascular assessment of plaque characterization.[3-5] Intravascular PAT has shown great potential, but this technique is not clinically available.

Interestingly, label-free compositional lipid imaging has been primarily explored in humans, and molecular contrast-enhanced methods are typically constrained in mice.

An under investigated area of photoacoustic imaging is the use of advanced compositional imaging for murine plaque assessment [1]. Thus, the work described in this dissertation is novel as it focuses on developing methodology and providing utility towards characterizing murine lipid accumulation. Our rationale is that the development of novel preclinical techniques can motivate new questions that may allow us to learn about disease progression in the human condition. For instance, assessing lipid composition during lesion formation can potentially provide insights into how lipid deposition impacts plaque location, size, material property, and vascular hemodynamics. Preclinical techniques can also improve the validation of novel therapeutics, as well as lead to the translation of innovative clinical techniques.

To demonstrate the utility of PAT for atherosclerosis imaging, we will first provide an overview of preclinical and clinical applications of PAT for atherosclerosis imaging. Analysis of iliac stenosis on abdominal aortic aneurysm formation will highlight the quantitative vascular remodeling capabilities of ultrasound. We then introduce a high-resolution PAT system capable of imaging in the second near-infrared window (1100-1300nm) followed by an in vivo proof-of-concept study to visualize and quantify periaortic fat accumulation. An in-depth experimental analysis will also be provided to assess the impact of illumination geometry on signal-to-noise ratio and penetration depth. This dissertation will conclude with a validation study for atherosclerotic lesion characterization using PAT, as well as a comprehensive study using dual-modality PAT and ultrasound to characterize lesion development.

2. CURRENT APPLICATIONS IN ATHEROSCLEROSIS PHOTOACOUSTICS

As the title of the dissertation suggests, the focus of the work presented here is to outline the methods, advancements, and application of photoacoustic tomography and ultrasound imaging for atherosclerosis imaging. We will first discuss the advantages and limitation of current clinical diagnostic techniques, followed by a comprehensive review of the literature on the applications of photoacoustic imaging for atherosclerosis imaging. This chapter contains published content from the Journal of Optics entitled, "Photoacoustic tomography: application for atherosclerosis imaging." The published version of this chapter is available through the following link: https://doi.org/10.1088/2040-8978/18/8/084005

2.1 Abstract

Atherosclerosis is a debilitating condition that increases a patient's risk for intermittent claudication, limb amputation, myocardial infarction, and stroke, thereby causing approximately 50% of deaths in the western world. Current diagnostic imaging techniques, such as ultrasound, digital subtraction angiography, computed tomography angiography, magnetic resonance angiography, and optical imaging remain suboptimal for detecting development of early stage plaques. This is largely due to the lack of compositional information, penetration depth, and/or clinical efficiency of these traditional imaging techniques. Photoacoustic imaging has emerged as a promising modality that could address some of these limitations to improve the diagnosis and characterization of atherosclerosis-related diseases. Photoacoustic imaging uses near-infrared light to induce acoustic waves, which can be used to recreate compositional images of tissue. Recent developments in photoacoustic techniques show its potential in noninvasively characterizing atherosclerotic plaques deeper than traditional optical imaging approaches. In this review, we discuss the significance and development of atherosclerosis, current and novel clinical diagnostic methods, and recent works that highlight the potential of photoacoustic imaging for both experimental and clinical studies of atherosclerosis.

2.2 Introduction

Atherosclerosis causes approximately 50% of all deaths in the western world despite recent technological advances in clinical diagnosis and treatment.[6] Many people who suffer from atherosclerosis-related complications do not present with symptoms until advanced stages in disease progression, creating a need to improve early diagnosis for atherosclerosis-related diseases. Non-invasive imaging modalities have also become paramount in pre-clinical studies of atherosclerosis; notably in the study of disease progression, novel therapeutic evaluation, and development of animal models that mimic the human condition. While great strides have been made in recent decades in the advancement of pre-clinical and clinical imaging systems, there remains room for improvement in identifying and characterizing atherosclerotic lesions. Photoacoustic (PA) imaging, as described below, has emerged as a promising tool to study atherosclerosis-related diseases and characterize plaques as it has the potential to provide anatomical, compositional, and molecular information of atherosclerotic lesions.

Many patients who suffer from atherosclerotic related disease experience a wide variety of complications that can severely reduce quality of life and even cause death. Plaque rupture in the cerebral, carotid, and coronary arteries can induce potentially life threatening ischemic strokes and myocardial infarctions, while plaque accumulation in the lower extremities can cause debilitating intermittent claudication and critical limb ischemia. Because of the high incidence of these complications, healthcare systems, patients, and society share the exorbitant economic burden of diagnosing and treating atherosclerosis-related diseases.[7] Current atherosclerosis treatment focuses on attenuating the growth and potentially decreasing plaque accumulation in the vasculature through the management of risk factors such as obesity, diabetes, smoking, hyperlipidemia, and hypertension.[8-10] In more severe cases, medical therapy and/or surgery are used to reduce or eliminate arterial stenosis.[8-10] Even in the case of proper treatment, some patients do not respond and debilitating effects of atherosclerosis remain. The late stage diagnosis of atherosclerosis is partly due to inadequate imaging techniques that have difficulty identifying the disease at early time points. Thus, there is a clear need for a rapid, noninvasive, and cost-effective imaging modality to improve the risk assessment, diagnosis, and treatment of atherosclerotic disease.

The objective of this article is to describe atherosclerotic disease progression, current clinical diagnostic methods, and recent advances in PA imaging. Through this review, we hope

to highlight recent work that shows PA imaging has the potential to improve the study and diagnosis of atherosclerosis-related disease. We will do this by describing imaging techniques currently used to assess atherosclerosis such as ultrasound, magnetic resonance angiography, computed tomography angiography, digital subtraction angiography, and optical imaging, with particular focus on their advantages and disadvantages as they relate to atherosclerosis diagnosis. We then provide an introduction to PA imaging with an emphasis on lipid imaging. This review specifically focuses on the advancements of lipid-based PA imaging and its uses in pre-clinical and clinical applications.

2.3 Methods of Literature Review

This review was conducted using references from PubMed and Web of Science databases. All references used in this review are from English peer-reviewed journal articles and textbooks. Textbooks were specifically used for content describing clinical imaging techniques and atherosclerosis pathophysiology. References used for PA imaging, however, were strictly from peer-reviewed journals. The following key words were used in the literature search: “carotid artery disease”, “coronary artery disease”, “peripheral artery disease”, “atherosclerosis”, “ankle brachial index”, “duplex ultrasound”, “magnetic resonance angiography”, “digital subtraction angiography”, “computed tomography angiography”, “nonlinear optical imaging”, “florescence imaging”, “optical coherence tomography”, “photoacoustic”, and “optoacoustics”. Effort was taken to select articles between January 2005 to February 2016 and highly cited, seminal journal articles.

2.4 Discussion of Literature

2.4.1 Atherosclerosis Progression

Atherosclerotic pathophysiology is a multifactorial process that involves the interaction of both environmental and genetic factors. The progression of atherosclerotic plaque development can be separated into six distinct classifications (Types I-VI; **Figure 2.1**).[11] Arterial plaques typically originate from an insult to the arterial endothelial layer, causing Type I lesions that are characterized by diffusion of low-density lipoprotein (LDL) into the subendothelial space.[12] Damage to the endothelial layer can be influenced by a variety of hemodynamic factors,

including low wall shear stress, increased oscillatory shear, and complex blood flow profiles near bifurcations and other tortuous regions of the vasculature.[13; 14] Subendothelial LDL is eventually oxidized by free radicals and stimulates an inflammatory response that causes macrophage migration into the subintimal space. These macrophages begin to phagocytize oxidized LDL and transform into foam cells,[15; 16] which accumulate to form Type II plaques.[11; 17] Type III plaques are characterized by both the migration of smooth muscle cells from the media to the intima[11; 17] and the production of collagen that further promotes formation of a fibrous cap. Accumulation of foam cells and collagen production continue until a fatty necrotic core is formed, characteristic of Type IV plaques. Patients with Type I-IV plaques may be asymptomatic, as stenotic vessels compensate for decreased blood flow by dilating, a phenomenon often referred to as Glagov remodeling.[17-20] Additionally, it is possible that an arterial stenosis is simply not restrictive enough to cause symptoms under normal physiologic conditions, making the detection of early stage plaques difficult.

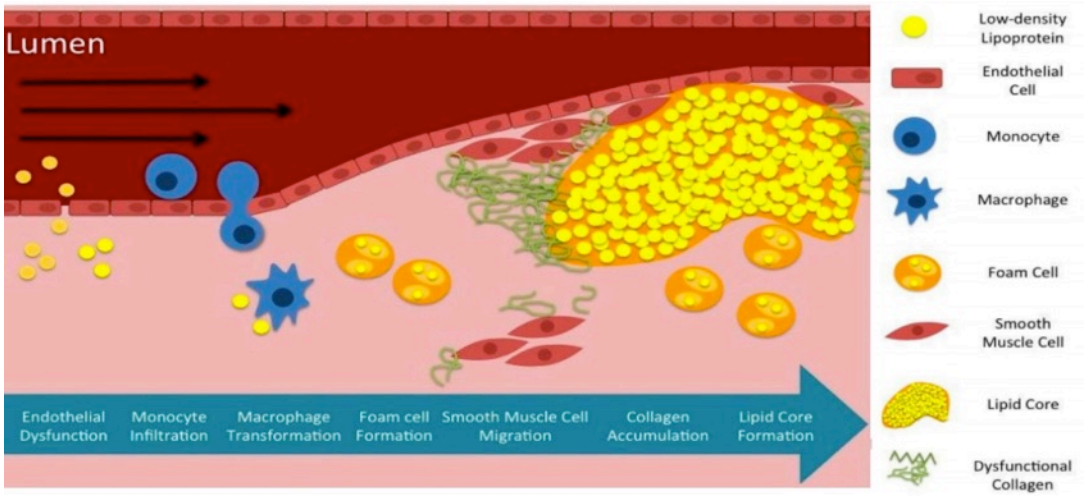

Figure 2.1: Early Type I-IV plaque progression of atherosclerosis beginning with endothelial dysfunction and ending with lipid core formation. Figure adapted and modified from Lin et al.[21]

The progression of atherosclerosis becomes a greater clinical concern when Type V-VI plaque formation begins, since these lesions are more likely to cause severe stenosis and are prone to rupture. Type V plaques form when lipid accumulation causes the destruction of healthy vascular cells and connective tissue, leading to more advanced remodeling of the extracellular matrix.[11] Increased collagen production, lipid accumulation, and cell migration account for increased plaque size, which begins to narrow the arterial lumen. These plaques can become

multilayered (Type V_a), calcified (Type V_b), or fibrotic (Type V_c) depending on their structural properties. Type V_a plaque forms when multiple layers composed of lipid cores and connective tissue accumulate,[11] causing stenosis and decreased blood flow. Type V_b plaques are characteristic of excessive mineral deposits that accumulate as cell death occurs.[11] Although these plaques are less likely to rupture as they often are more calcified, they still cause narrowing of the lumen. Type V_c plaques are rupture-prone, can cause myocardial infarction and strokes, and are commonly seen in patients who suffer from advanced stages of atherosclerosis.[11] In Type V_c plaques, the intima is replaced with a thick fibrous tissue, while lipid is minimal or even absent.[11] Further progression involves complicated lesions (or Type VI plaque) that are identified when hematoma/thrombosis form or when Type V plaques are disrupted. Each stage of atherosclerosis formation is discernible by specific markers; for instance, compromised endothelium (Type I), inflammation (Type II), apoptosis (Type III), intraplaque neovascularization (Type IV), decreased fibrous cap thickness (Type V), and complicated lesion formation (Type VI) all mark milestones in atherosclerosis progression. Monitoring and detecting these features are important in the diagnosis and treatment of atherosclerotic patients, as lumen narrowing does not always precede more serious complications such as plaque rupture.[22] Therefore, modalities that can provide compositional information are often advantageous when imaging atherosclerosis.

2.4.2 Current Diagnostic Techniques

Recent advances and refinements in imaging techniques have improved the diagnosis and treatment of atherosclerosis-related diseases. Current diagnostic methods for atherosclerosis characterize morphological and functional parameters that aid clinicians in determining focal lesion severity. In this section, we specifically focus on the application, advantages, and disadvantages of ultrasound, magnetic resonance angiography (MRA), computed tomography angiography (CTA), and digital subtraction angiography (DSA) for atherosclerosis diagnosis.

2.4.2.1 Ultrasound

Ultrasound is a portable and inexpensive imaging modality that provides clinicians with high-resolution, real-time images for anatomical and hemodynamic characterization of tissue.[23] Atherosclerotic lesions are typically characterized by using either duplex ultrasound (DUS) with

a transcutaneous transducer or intravascular ultrasound (IVUS) with a transducer on the end of a catheter. DUS typically emits 1-10 MHz acoustic waves into the body and records the echoes that are reflected from tissue boundaries due to differences in acoustic impedance to reconstruct real-time images.[23] Current DUS imaging standards for peripheral and carotid arteries include gray-scale B-mode imaging to visualize arterial stenosis (**Figure 2.2A-B**), and color Doppler and spectral Doppler velocity for blood flow velocity.[24; 25] Together, these techniques are used to classify stenosis by varying degrees of occlusion.[24] IVUS, on the other hand, utilizes miniaturized ultrasound probes that are attached to a catheter to characterize atherosclerotic lesions from within a blood vessel.[26] Compared to DUS, IVUS typically utilizes 20-45 MHz frequency ranges,[27] thus providing higher resolution, but reduced depth of penetration. This technique is optimal for imaging deeper and smaller vessels, such as the coronary arteries, that DUS has difficulty visualizing. Using IVUS, the clinicians can obtain short-axis images of the artery with a pullback approach to visualize plaque accumulation and better classify lesions as fibrous, fibrolipidic, calcified, and calcified-necrotic.[28] Overall, the minimally invasive nature of ultrasound makes it a valuable tool for preliminary and advanced screening of arterial lesion development.

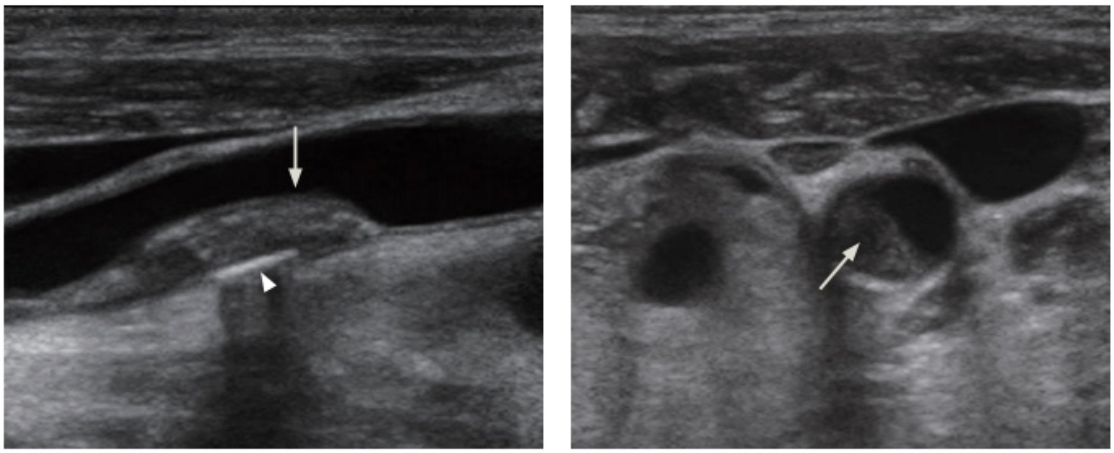

Figure 2.2: A gray-scale long-axis ultrasound image of the distal common carotid artery (left). Calcification (arrowhead) and plaque (arrow) can be clearly visualized within the artery. A short-axis ultrasound image of the distal common carotid artery (right). The more lucent plaque (arrow) is typically associated with higher risk of plaque rupture. Figure adapted from Lee et al. [29]

While vascular ultrasound is an optimal method to obtain anatomical and hemodynamic information, it also has inherent limitations that can hinder its clinical capabilities. Clinical ultrasound is unable to detect lipid compositions and molecular markers, which may be useful in

classifying plaque stability. Moreover, Doppler measurements may be inaccurate for stenosis that is less than 50% of the original diameter due to diverse plaque morphology and composition.[24] This technique is likely to overlook stenosis because of its lower sensitivity compared to magnetic resonance and X-ray imaging modalities (Error! Reference source not found.**.1**;[30]). Ultrasound is also susceptible to various artifacts that can affect image quality and diagnosis.[26; 31] One challenge specific to IVUS is difficulty in imaging some vessels due to motion artifacts caused by unstable catheter positions.[26] Moreover, it can be difficult to spatially orient IVUS images unless specific landmarks such as branching vessels or tissue are present.[26] Ultrasound techniques have also been used to measure both the thickness of the tunica intima and media of an artery; the use of intima-media thickness as an accurate marker for atherosclerosis is, however, debated in the literature.[32; 33]

Table 2.1: Sensitivity and specificity range for clinically relevant diagnostic techniques for atherosclerosis detection.

Imaging Modality	Sensitivity	Specificity
Duplex Ultrasound	74-92% [30]	96-100% [30]
Intravascular Ultrasound	92-100% [34]	56-68% [34]
Digital Subtraction Angiography	54-95% [35; 36]	70-99%[35; 36]
Computed Tomography Angiography	89-100% [30]	99-100% [30]
Contrast Enhanced Magnetic Resonance Angiography	85-100% [30]	97-100% [30]
Time of Light Magnetic Resonance Angiography	77-100% [30]	85-98% [30]

2.4.2.2 X-ray Techniques

X-ray imaging is a transmission-based technique that involves passing X-rays through a patient and measuring emission on the opposite side of the body.[23] The contrast in X-ray imaging comes from the tissue-specific attenuation of X-rays that typically allows for differentiation based on tissue density. X-ray angiography techniques are a subset of X-ray methods that have been optimized for vascular imaging and are, therefore, useful for atherosclerosis detection. DSA and CTA are the two major X-ray angiography techniques that use iodine-based contrast agents to acquire vascular angiograms, a valuable capability that allows clinicians to pinpoint narrowed vessels.

DSA is the current gold standard for atherosclerosis imaging, but is becoming less common for atherosclerosis diagnosis due to advances in CTA and MRA imaging.[37] Dense tissue

and bone artifacts affect conventional X-ray imaging quality, making it difficult to visualize overlapping vasculature. During a DSA scan, an image is captured before and after the injection of an iodine contrast agent, and an image subtraction is performed to remove detracting tissue artifacts, providing clearer visualization of peripheral vessels.[38] DSA provides high spatial resolution, offering exceptional image quality to visualize stenotic vessels. Unfortunately, DSA involves the use of an ionizing radiation[30; 38] and can potentially cause nephrotoxicity.[30] The procedure also involves arterial puncturing of the femoral artery to deliver the contrast agent, increasing the risk of bleeding, infection, and stroke.[38; 39] The use of DSA for imaging vessels below the knee is problematic due to lesion morphology and location (**Figure 2.3E**;[38]). DSA has been widely utilized to diagnose atherosclerosis, but its limitations have decreased its use in the clinic in favor of other three-dimensional techniques.

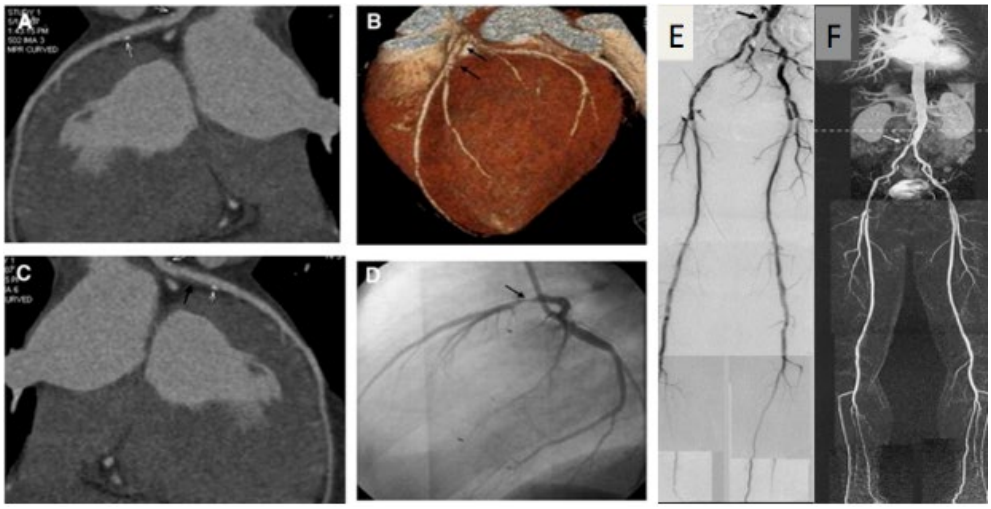

Figure 2.3: A) Coronary CTA maximum intensity projection images reveal plaque in proximal segment of left anterior descending artery (LAD) with calcification (white arrow). B) Volume rendering show plaque accumulation in proximal segment of LAD (black arrow). C) Maximum intensity project show calcified plaque in proximal segment of LAD. D) CTA image clearly shows severe stenosis in coronary artery (black arrow). (E) DSA and (F) MRA images of stenotic proximal iliac artery, shown by black and white arrows. Subfigure A-D adapted from Yorgun et al. [40] Subfigures C and D are adapted from Ruehm et al.[41]

CTA is an evolving X-ray based technique that is becoming clinically accepted for the diagnoses of atherosclerosis. CTA does not require image subtraction and delivers contrast through intravenous injections; as a result, CTA is a less aggressive technique that offers shorter imaging times and is capable of imaging the entire vascular tree (**Figure 2.3A-D**;[42]). CTA has great sensitivity and specificity (Error! Reference source not found.) compared to other techniques, allowing for accurate diagnosis of atherosclerosis.[43; 44] The temporal resolution of

CTA, however, is 20 times worse than that of conventional X-ray techniques.[22] Therefore, to produce optimal images, a large dosage of radiation is required,[22; 45-47] which can have health implications considering that patients with atherosclerosis will typically undergo multiple scans in their lifetime.[22] As with other techniques discussed thus far, X-ray angiography does not provide molecular or compositional information to differentiate between vulnerable and stable plaques.[48]

2.4.2.3 Magnetic Resonance Angiography

Magnetic Resonance Imaging (MRI) is a nonionizing imaging technique that provides three-dimensional images with high spatial resolution. MRI uses magnetic fields to align hydrogen atoms that precess coherently in the presence of a weak radiofrequency field.[23] MRA is a group of techniques, based off of MRI, which is optimized to visualize blood vessels with high sensitivity and specificity (**Table 2.1**;[49-52]), making it one of the most accurate atherosclerosis diagnostic methods.[30]

Atherosclerotic lesions are typically diagnosed with either flow dependent time-of-flight (TOF) MRA or flow independent contrast-enhanced (CE) MRA. Moving blood produces a much higher signal compared to static tissue with TOF-MRA. This technique, however, is susceptible to image acquisition artifacts[53] and inaccurate imaging results in the presence of complex blood flow.[54] This technique is also susceptible to stenosis size overestimation,[55] which motivates the use of flow independent CE-MRA for the diagnosis of atherosclerosis-related diseases. With CE-MRA, an image is acquired before and after the injection of a gadolinium contrast agent, and the two images are subtracted to obtain an image of the vasculature. Since CE-MRA relies on contrast agents, it is not as easily susceptible to time-of-flight artifacts, thus provides higher quality images for a more accurate diagnosis of atherosclerosis (**Figure 2.3F**). In some cases, the gadolinium-based contrast has been associated with nephrogenic systemic fibrosis, excluding patients with advanced kidney disease from this approach.[56-58] MRI has several other limitations including high scanning cost, prolonged scan times,[38] millimeter scale resolution,[23] and the difficulty of imaging patients who are claustrophobic[38] or have implanted medical devices.[37] MRI has been used, however, to characterize plaque components,[59] such as lipid-rich necrotic core,[60; 61] fibrous cap,[60-62] and calcification.[61] While MRI has the potential to characterize plaque composition, this feature is not widely used in the clinic.

We have described both advantages and limitations in current clinically adopted diagnostic imaging techniques in characterizing atherosclerotic plaques. Because of the complexity of this disease, arterial disease diagnosis commonly relies on a multimodal imaging approach. For instance, DUS can be used as a first pass imaging method for high-risk populations, such as diabetics and smokers, followed by MRA, DTA, and CTA for more in depth imaging of arterial lesions.[38] DUS and MRA avoid the use of invasive ionizing radiation and are, therefore, among the least invasive imaging techniques. Ideally, CTA and DSA should not be used if there are any concerns regarding the use of ionizing radiation or contrast agents. While these traditional techniques certainly are helpful, additional compositional and molecular information about atherosclerotic lesions could help guide clinical care. Thus, clinicians would likely benefit from additional imaging techniques that can provide full anatomical, compositional, and molecular imaging of the vasculature.

Table 2.2: Summary of advantages and disadvantages of clinically adopted, optical, and PA techniques in the diagnosis of atherosclerosis-related disease. Table adopted and modified from Lin et al. [21].

Diagnostic Method	Advantages	Disadvantages
Ultrasound	• Fast acquisition time • Portable • High spatiotemporal resolution • No harmful radiation	• Acoustic artifacts • Often difficult to interpret
Magnetic Resonance Angiography	• Non-ionizing • Superior tissue differentiation • Provides anatomical, functional, and molecular information • Whole body imaging capability	• Lower temporal resolution compared to ultrasound • High cost
X-ray	• Fast acquisition time • High spatiotemporal resolution • Provides information about spatial geometry, luminal patency, and vascular networks • Whole body imaging capability	• Ionizing radiation • Lacks soft tissue differentiation • Requires contrast agent
Optical Imaging	• High sensitivity • No ionizing radiation • Availability	• Limited penetration depth (<1–2 mm) • Susceptibility to photobleaching
Photoacoustic Imaging	• Increased penetration depth compared to conventional optical imaging • High molecular and compositional sensitivity	• Susceptible to acoustic artifacts • Lack of anatomical information

2.4.2.4 Optical Imaging Techniques

Optical imaging techniques are also being developed to improve the diagnosis of atherosclerosis-related diseases. Optical methods are non- or minimally-invasive, chemically selective, and provide high-resolution images that allow for imaging small structures below the cellular length scale.[63; 64] In this section we will briefly discuss optical techniques that are being developed for atherosclerosis imaging applications.

2.4.2.5 Fluorescence Imaging

Fluorescence imaging is a branch of optical imaging that commonly utilizes fluorescent dyes to visualize molecular processes, such as protein expression. Due to their poor imaging depth, fluorescence techniques are typically coupled with IVUS techniques to image plaque severity. Sun et al. developed a simultaneous time- and wavelength-resolved fluorescence spectroscopy method to image atherosclerotic lesions *ex vivo* and *in vivo.*[65] This technique uses a single excitation input and a detector to image the fluorescence emissions spectra for characterizing diseased tissues. Fluorescence imaging is capable of correlating the degree of atherosclerotic progression with the normalized intensity ratio.[65] Near infrared fluorescence (NIRF) intravascular molecular imaging is another modality developed for vascular imaging. Intravascular NIRF uses protease-activatable fluorescent agents to detect areas prone to atherosclerotic lesions. Calfon et al. used a cysteine protease-activatable NIRF probe to detect plaque inflammation *in vivo,* induced by balloon injury in the iliac arteries of atherosclerotic rabbits.[66] They showed that atherosclerotic lesions produced a strong NIRF signals 24 hours post agent delivery. Fluorescent techniques have also been employed to take advantage of intrinsic autofluorescence of atherosclerotic molecules, but these methods are limited, as they are performed *ex vivo.*[67; 68] Taken together, these fluorescence imaging approaches show the potential of fluorescent imaging for early plaque detection and characterization.

2.4.2.6 Optical Coherence Tomography

Optical Coherence Tomography (OCT) is an emerging technique that uses scattering from biological tissue to create volumetric data sets with μm-resolution.[69] OCT works by probing local tissue with near infrared light to produce high-resolution images of vascular tissues. This technique utilizes a method called interferometry to reject light that scatters multiple times

before detection, reducing scattered light noise that can corrupt images. Recently, there has been an emphasis to develop OCT for atherosclerosis diagnosis using intravascular catheters. An *ex vivo* study by Yabushita et al. showed that OCT can be used to differentiate between fibrous, fibrocalcific, and lipid rich plaques with high sensitivity and specificity.[70] OCT is largely limited in efficacy due to its short depth of penetration of 1-2mm.[70] Intravascular OCT uses a probe placed within an atherosclerotic artery, aiding in the quantification of plaques composition.[70-72] OCT is a promising technique that can be coupled with other modalities to produce high-resolution images of atherosclerotic lesions, but still lacks the penetration depth often needed for robust characterization.

2.4.2.7 Nonlinear Optical Imaging

Nonlinear optical imaging is a subfield in optics that focuses on the interaction of light and matter in a nonlinear fashion. This modality encompasses coherent anti-Stokes Raman scattering (CARS), second harmonic generation (SHG), and two photon excited fluorescence (TPEF), each of which have advantages in tissue imaging. Together, these techniques allow for the study of biological components that are involved in inflammation and plaque formation. Specifically, these modalities have been used to image collagen fibers,[73; 74] elastin fibers,[73; 74] and lipid accumulation,[75; 76] respectively. In fact, a study by Wang et al. showed that these three imaging modalities could also be extended to image endothelial and smooth muscle cells.[74] Nonlinear optical microscopy modalities are limited by a small scan area and limited depth of penetration, which is typically less than 1mm. While the translational potential to the clinic is limited, nonlinear optics can play a vital role in the study of atherosclerosis pathophysiology.

Early molecular and compositional detection of plaques can be beneficial in the diagnosis and treatment of atherosclerosis-related diseases.[77; 78] While optical techniques are being developed to improve molecular imaging, these efforts have their limitations due to suboptimal penetration depths. Intravascular techniques such as fluorescence and OCT are promising, but are minimally invasive and limited by a relatively high cost. In fact, these techniques come with the added risk of catheter-related infections that are often be harmful to patients.[79] Therefore, these procedures are only used on patients diagnosed with severe atherosclerosis that are in of plaque characterization. PA imaging can complement currently used technologies as it has

shown the potential to provide *in vivo* anatomical, compositional, and molecular information of atherosclerotic lesions in a rapid, cost effective, and minimally invasive manner.

2.4.3 Photoacoustic Imaging

Over the past decade, substantial effort has been made to develop PA imaging for visualization of biological components that are relevant to the diagnosis of atherosclerosis (i.e. blood, collagen, and lipids). This inherent property of PA imaging to provide compositional information allows for advanced plaque characterization that many current clinical techniques cannot provide. As a consequence, PA imaging has the potential to be used as a platform for spectroscopic and tomographic imaging of atherosclerosis-related disease. In this section, we will briefly discuss the theory behind PA imaging and elaborate on its uses as a platform for imaging atherosclerosis.

2.4.3.1 Introduction to Photoacoustic Imaging

The PA effect involves the delivery of pulsed laser light to tissue, which induces acoustic wave propagations through thermoelastic expansion. To elaborate, thermoelastic expansion occurs when tissue expands due to an increase in temperature, which stimulates acoustic wave propagation that can be acquired to reconstruct an image (**Figure 2.4**). The temperature rise is caused by light absorption of specific functional groups, such as CH_2-rich lipids and CH_3-rich collagen, which release the energy as heat.[80] In order to generate thermoelastically-induced PA signals efficiently, the thermal and stress confinement conditions must be met.[81]

$$\tau_p = \frac{2\delta_T^2}{D_T} \qquad \textbf{Equation 2.1}$$

$$\tau_{th} \sim \frac{L_p^2}{4D_T} \qquad \textbf{Equation 2.2}$$

In the thermal confinement condition, the pulse width (τ_p) must be shorter than the time it takes for heat dissipation of absorbed light (τ_{th}). These parameters are dependent on thermal diffusion length (δ_T), thermal diffusivity of soft tissue (D_T), and the geometry of the tissue volume being heated (L_p), as shown in **Equations 2.1** and **2.2**.[81] The thermal confinement condition allows for the efficient propagation and acquisition of laser-induced photoacoustic

signals. The stress confinement condition is met when the pulse width is shorter than the time it takes for stress to pass through the light-induced heated region (τ_s). This region is dependent on L_p and the speed of sound through tissue.[81] The stress confinement condition allows the thermoelastically-induced pressure to rapidly build up in the tissue. When both thermal and stress confinement conditions are met, the PA pressure rise can be described by **Equation 1.3**, which shows that the acoustic pressure rise is governed by temperature-dependent Grueneisen parameter (Γ), absorption coefficient (μ_a), and local optical fluence (F).[82; 83]

$$P_o = \Gamma \mu_a F \qquad \textbf{Equation 1.3}$$

This fundamental equation shows that the PA signal amplitude at the absorber is dependent on the amount of light delivered to the tissue, absorbed by the tissue, and the temperature rise of the tissue. Every one millikelvin rise in temperature typically results in a 800 Pascal pressure rise, which is detectable by a high frequency ultrasound transducer.[82] The resulting PA image is therefore reconstructed depending on the location of the PA signal and amount of pressure generated when the tissue is irradiated by light.

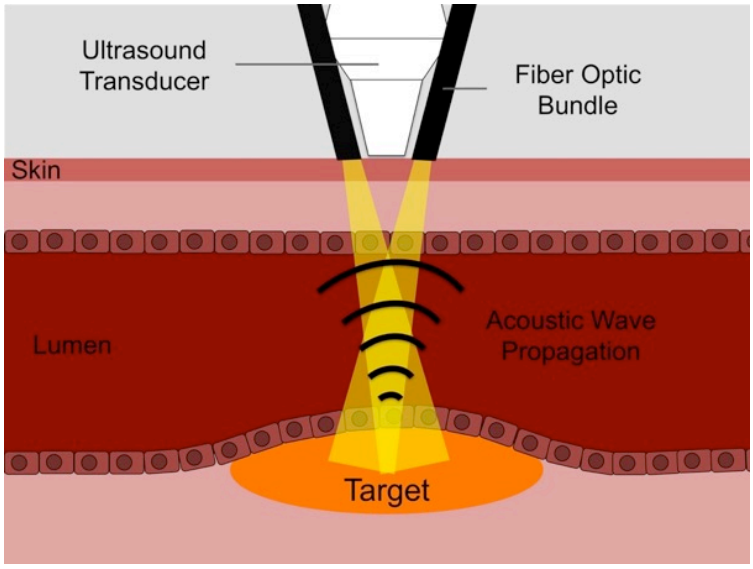

Figure 2.4: Schematic of in vivo plaque imaging. Bifurcated fiber optic bundles deliver light to plaque to induce acoustic waves that are detected by an ultrasound transducer.

The optical properties of biological tissues, specifically scattering and absorption, are dependent on the electronic and vibrational structures of the molecules that construct them.[81]

Conventional optical imaging is often hindered by light scattering, which causes loss of directionality and limits imaging depth into tissue. Current optical techniques utilize either focused ballistic photons that allow imaging up to 1mm into tissue, or diffuse techniques that have reduced spatial resolution.[84] Since acoustic scattering is two to three times weaker than biological optical scattering, PA imaging can typically provide better spatial resolution at depths beyond 1mm.[81] These properties allow PA imaging to obtain compositional information in tissue with superior penetration depth compared to conventional optical techniques.

While acoustic attenuation in soft tissue is not negligible, optical attenuation is the main limitation in lipid-based PA imaging. This becomes apparent for *in vivo* lipid imaging considering that much of the light is attenuated by both blood and subcutaneous fat. Several studies have shown that the potential penetration depth for PA imaging ranges from 4cm for non-contrast imaging[85] to 5-6cm for contrast enhanced imaging.[86; 87] The penetration depth for lipid imaging, however, has not been optimized as it is reported to be approximately 3cm through chicken tissue[88] and 3mm through fat[89] when using 1197nm light. Lipid-based PA imaging must, therefore, be improved to allow better depth of penetration that would permit characterization of lipid content in deeper atherosclerotic vessels, an area that has not been fully explored.

To induce the PA effect, light in the visible or near-infrared range is tuned to excite specific tissue components.[81] The two major regions of the electromagnetic spectrum that contain peak light absorption for lipids are 410-680nm[90] and 920-1730nm,[80; 91] with 1210nm and 1730nm generating the greatest signals as these are the first and second overtone excitations of CH_2.[80; 92] The majority of light between 410-680nm and 910-1040nm is prone to hemoglobin absorption or does not generate enough PA signal for *in vivo* imaging.[91] The greatest PA lipid signal is generated around 1730nm, but tomographic imaging of deeper tissue at this wavelength is limited due to excessive water absorbance.[80; 91] The use of 1210nm light, however, produces enough lipid PA signal to be used for noninvasive *in vivo* imaging. Light at 1730nm leads to strong PA signal, but has five-fold greater water absorption than 1210nm.[80] In summary, the wavelength of light used is highly dependent on the application (i.e. intravascular versus noninvasive imaging).

2.4.3.2 Multimodality Photoacoustic Imaging

On its own, PA imaging can only provide compositional information, which can be difficult to interpret without structural information. One key to optimizing PA imaging is to couple the modality with other imaging techniques. For instance, gadolinium(III)-gold nanorods have been used for atherosclerosis imaging by coupling MRI and PA techniques.[93] The benefit of using these two modalities is that MRI can be used to identify the location of lesions while PA imaging is able to quantify signal from gold nanorods to evaluate plaque severity by estimating the infiltration of macrophages in the vessel.[93] While promising, the use of MRI is not practical for initial atherosclerosis screening because of its high cost and longer imaging time. Another possibility is to couple PA with other emerging modalities such as OCT and fluorescence based techniques.[94-97] These techniques can complement each other to definitively characterize arterial plaques. For instance, PA, OCT, and fluorescence imaging have the capability to effectively evaluate lipid rich cores, fibrous cap thickness and calcification, and inflammation, respectively.[94] The major limitation, however, is integrating these technologies in a small and cost effect probe that can be used in the clinic. Currently, the more accessible multimodality approach is to couple PA with ultrasound imaging. The benefit of using PA imaging is that it provides optical-dependent contrast to tissue that ultrasound cannot produce on its own. Ultrasound, on the other hand, does provide structural and hemodynamic information that is useful in the diagnosis of vascular disease. It is also important to note that, from an engineering perspective, coupling ultrasound and PA imaging is relatively straightforward compared to combining PA imaging with other modalities. The sections below discuss how ultrasound and PA imaging can be used simultaneously as a platform for tomographic, intravascular, and molecular-based imaging as the clinical applications for this approach have not yet been fully explored. More specifically, coupling ultrasound and PA imaging can provide structural, compositional, and hemodynamic information about tissue that has the potential to improve atherosclerosis diagnosis and plaque characterization.

2.4.3.3 Intravascular Photoacoustic Imaging

The ability of PA imaging, coupled with ultrasound, to identify compositional and structural information has inspired the development of translational PA techniques. One of the most promising uses of PA imaging is the development of intravascular PA (IVPA) methods

coupled with IVUS. With IVPA/IVUS, a catheter is introduced through a large artery to image vessels prone to plaque development. Several studies have shown the potential of IVPA/IVUS to image atherosclerotic plaque in both *ex vivo* and *in vivo* experiments.[91; 98-101] Sethuraman et al. were the first to demonstrate that IVPA/IVUS can be used to differentiate between different lesion components such as plaques with thickened fibrous deposits, thin fibrillar structure, and lipid rich deposits using 650-900nm light.[102] In a separate study, the same group showed the ability of IVPA/IVUS to differentiate foam cells and fibrous caps.[103] Other groups have used atherosclerotic Ossabaw pig arteries to locate lipid core, scattered lipid deposition, and mild fatty streaks *ex vivo* [104]. Additionally, Wu et al. showed that IVPA/IVUS could be used to differentiate plaque and peri-adventitial fat using 1718nm and 1734nm light, which is particularly significant in vessels with a small wall thickness.[105] While the aforementioned *ex vivo* studies are promising, they cannot be used to predict the limitations of in vivo IVPA/IVUS. Wang et al. were the first to show the feasibility of using IVPA/IVUS for in vivo imaging of Watanabe heritable hyperlipidemic rabbit abdominal aorta via 1720nm light (**Figure 2.5**;[99]). Their study showed that 1720nm light could be used to image plaque accumulation within the artery without the need of a saline flush or balloon occlusion. The limitation of this study, however, is that it did not explore the possibility of utilizing the high lipid peak absorbance at 1210nm to detect plaques through blood. This is essential considering that 1730nm PA lipid signal is only greater than 1210nm signal when imaging through a blood layer less than 1 mm.[80] A study by Allen et al. used wavelengths between 740-1800nm and also found that 1200nm wavelength produced the highest lipid signal intensity when imaged through 4mm of blood.[91] This is important, as larger vessels may have limited PA-induced lipid signal due to a sizeable blood barrier between the PA probe and vessel wall. Taken together, these efforts have shown that IVPA has great potential for characterizing advanced lipid lesions, however, more comprehensive studies should be performed to show the feasibility of *in vivo* IVPA/IVUS to characterize plaques in various sized vessels using multiple wavelengths of light.

Though the reported studies are encouraging, IVPA/IVUS also is minimally invasive and carries procedural risks that make it viable for only a subset of patients. Indeed, IVPA/IVUS permits the majority of light to be focused on the vessel and prevents light attenuation by subcutaneous fat. This technique also provides structural and compositional information of tissue, making the detection and characterization of plaques feasible. Unfortunately, IVPA/IVUS is still

a minimally invasive technique and is best suited for imaging vessels reachable by a catheter. Moreover, it is impractical, and in some cases unnecessary, to utilize an intravascular procedure to diagnose all potential patients with atherosclerosis due to the cost, time, and invasiveness of the procedure. The foregoing studies were also performed using multiple wavelengths. While PA imaging is still in its infancy, the use of multiple wavelengths could be a translational limitation as tunable lasers are large, costly, and often require separate water chillers. These difficulties suggest that studies should be performed to test the capabilities of PA imaging to characterize plaques at limited wavelengths. IVPA/IVUS has potential to complement current imaging techniques, but more noninvasive PA techniques will be useful to improve the overall diagnosis of atherosclerosis-related disease.

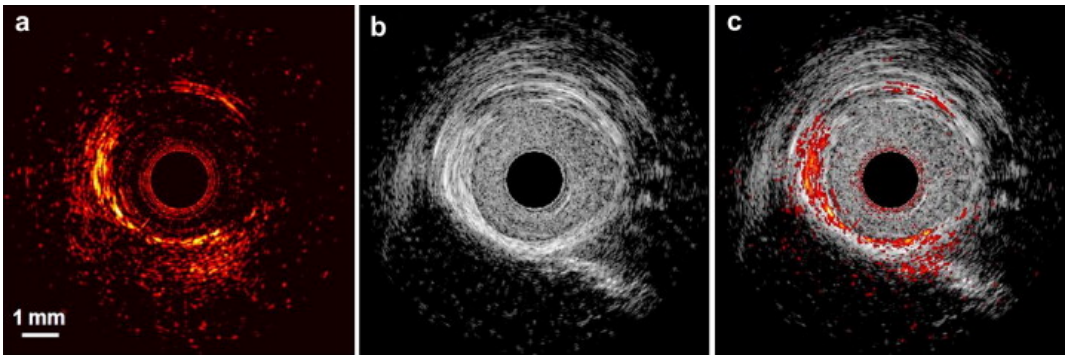

Figure 2.5: *In vivo* IVPA/IVUS imaging in Watanabe heritable hyperlipidemic rabbit abdominal aorta. (A) PA imaging was able to provide lipid characterization, (B) while ultrasound provided structural information. By overlaying these two images plaque accumulation can be resolved within the intimal layer. Figure adapted from Wang et al. [99].

2.4.3.4 Molecular-Based Photoacoustic Imaging

PA imaging is an attractive method to study the progression of atherosclerosis, but its ability to image molecular markers is nonexistent without the use of contrast agents. The use of contrast agents allows for imaging of various stages of atherosclerosis disease progression. Therefore, numerous types of nanoparticle have been developed to overcome this limitation. Gold nanoparticles are attractive contrast agents due to their surface plasmon resonance property of light absorption. Several studies have used gold nanoparticles to target E-selectin, ICAM-1, and VCAM-1,[106-108] which are known to help leukocytes adhere to endothelial cells.[109] Gold nanoparticles may also be used to detect macrophage infiltration of the endothelial cell layer, as macrophages have a natural tendency to phagocytize gold nanoparticles.[110-112] In fact, Yeager et al. used IVPA/IVUS with gold nanorods contrast agent to image plaque formation and quantify

lesion severity.[110] The use of gold nanoparticles for clinical use is debated, as they are not easily excreted from the body and their long-term consequence are unknown.[113] Gold nanoparticles are also commonly used with lower wavelengths of light, which may make noninvasive *in vivo* imaging difficult. However, these particles are still useful for studying atherosclerosis pathophysiology since they can be utilized for pre-clinical *in vivo* intravascular animal imaging.[110] Although gold nanoparticles may be useful in tracking macrophages in lesion formations, more work must be done to use these nanoparticles to target other areas of atherosclerosis progression including smooth muscle cell migration, LDL infiltration, and collagen formation to name a few.

Quantum dots have also been designed for PA applications by optimizing the property of light-induced acoustic production.[114] For instance, quantum dot-labeled monocytes, macrophages and T-lymphocytes have been delivered into an atherosclerotic mouse model to detect plaques as early as two days post-injection.[115] Like gold nanoparticles, quantum dots have also been functionalized with various markers to detect inflammation,[116; 117] but they have not been used for PA imaging. Quantum dots, however, have been utilized with other modalities, such as microPET and optical techniques[118] for pre-clinical applications. While studies have shown that certain quantum dots can be cleared by the renal system,[119] optimization studies are still needed to determine and prevent cytotoxicity.[120] Thus, nanoparticle-based contrast is not limited to gold nanoparticles and that safe PA contrast agents can be potentially designed for pre-clinical imaging.

PA imaging for the detection of extracellular matrix degrading proteases is also an important area of development as these are involved in vulnerable plaque production.[121] Levi et al. developed an enzyme-activatable probe that generated PA signals at 675 and 750nm. In the presence of proteases, however, this probe is cleaved to form a cell penetrating peptides that produces a signal at only 675nm.[122] Moreover, PA signal produced from a matrix metalloproteinases-sensitive activatable fluorescent probe (MMPSense) has been used to detect MMP activity in *ex vivo* carotid plaque samples.[123] MMPSense is an optically silent agent when introduced into the body and produces a fluorescent signal once cleaved by metalloproteinases. These probes are promising for PA imaging, as they have not been reported to produce cytotoxic effects. Additional *in vivo* studies are needed, however, to determine the concentration of probe required to detect vascular inflammation, where these probes bind in atherosclerotic plaques, and

how they are excreted.[83] If effective, these probes could be used to develop targets for early stage diagnosis of atherosclerosis-related disease.

Table 2.3: Summary of currently available nanoparticles for PA imaging, their targets, and implications for atherosclerosis imaging.

Nanoparticles	Target	Implication
Gold nanoparticles [106-108; 110-112]	E-selectin, ICAM-1, VCAM-1, macrophage	Inflammation
Quantum dots [115]	Monocytes, macrophages, T-lymphocytes	Inflammation
Enzyme-activatable probe [122]	Protease	Extracellular matrix degradation
MMPSense [123]	Metalloproteinases	Extracellular matrix degradation
Copper nanoparticles [124]	$\alpha_v\beta_3$	Angiogenesis
Indocyanine Green-dye enhanced single walled carbon nanotubes [125]	$\alpha_v\beta_3$	Angiogenesis

PA contrast agents have also been developed to image angiogenesis, a phenomenon where new capillaries form from preexisting vessels to compensate for decreased blood flow in stenotic vessels. The benefit of these approaches is that $\alpha_v\beta_3$ expression is present in angiogenesis and is also a marker for vulnerable plaque.[124] Recently, Zhang et al. used $\alpha_v\beta_3$ targeted copper nanoparticles to image angiogenesis in matrigels and showed drastic improvement in capillary imaging using these targeted particles (**Figure 2.6**;[124]). The additional benefit of using copper nanoparticles is that they are cheaper, biocompatible, and produce PA imaging signals that are comparable to that produced by gold nanoparticles.[126] Zerda et al. performed similar works, but used $\alpha_v\beta_3$ targeted indocyanine Green-dye enhanced single walled carbon nanotubes to obtain enhanced signal in tumor angiogenesis.[125] The development of collateral artery formation is particularly important in the study of peripheral artery disease where there is limited blood flow to the lower extremities. The limitation, again, of using nanoparticle based contrast agents is that their long-term effects are unknown. Therefore, the use of these nanoparticles would be specifically beneficial in animal studies of prospective therapeutics for collateral artery formation.

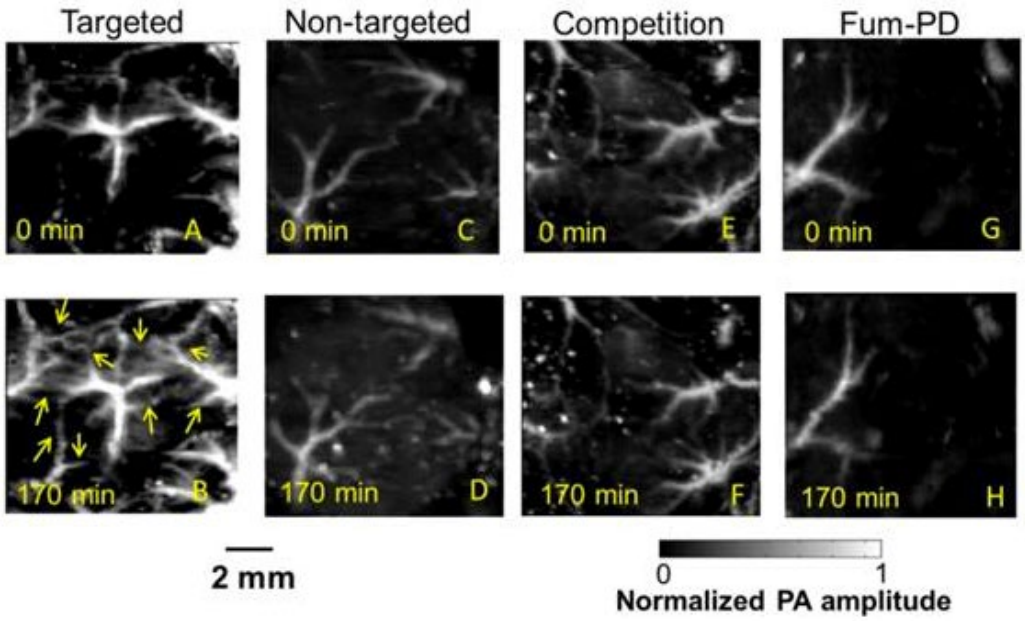

Figure 2.6: In vivo PA image angiogenesis visualized by utilizing $\boldsymbol{\alpha_v\beta_3}$ targeted copper nanoparticles. Significant PA signal can be seen between targeted (A-B) and non-targeted (C-D) groups at time 0 and 170 minutes (yellow arrows). A competition group (E-F) was given $\boldsymbol{\alpha_v\beta_3}$-oil only nanoparticles 10 minutes prior to imaging and $\boldsymbol{\alpha_v\beta_3}$-CuNP directly before imaging. Fumagillin prodrug (Fum-PD) group (G-H) was given both $\boldsymbol{\alpha_v\beta_3}$-CuNP and fumagillin prodrug 11 and 15 days after Matrigel implantation and $\boldsymbol{\alpha_v\beta_3}$-CuNP before imaging. There is little change in PA single between non-targeted, competition, and fumagillin-prodrug images. PA images were taken using 767nm wavelength. Figure adapted from Zhang et al.[127].

PA imaging has the potential to enhance molecular imaging of atherosclerosis with the help of various contrast agents (**Table 2.3**). Using contrast agents can allow for imaging of specific markers of atherosclerosis progression such as macrophage infiltration, extracellular changes, and collateral artery formation. While gold nanoparticle are useful to study atherosclerosis, their application to the clinic is limited. Gold nanoparticles have been tested on human cells,[113] but no longitudinal studies have been conducted in human subjects. This is mainly due to the unknown long-term effects of these particles.[113; 128] A benefit of using organic dyes over nanoparticles is that they are biocompatible, are easily excreted from the body, and have been used for clinical applications. The concern with dyes, however, is that their rapid clearance means that they are less likely to be delivered to plaque-detecting targets. To solve this problem, encapsulating techniques have been used to increase the circulation and delivery time of dyes.[129; 130] While the current status of PA contrast agents does not currently allow for their clinical translation, their use is likely to be important in the study atherosclerosis progression in animal models.

2.5 Preclinical and Clinical Directions

PA imaging is a rapidly evolving modality that has the potential to improve plaque detection and our knowledge of atherosclerosis disease progression. While the development of PA techniques has come a long way in recent years, there is still more work that is needed to improve its use in clinics and laboratories. We have seen that there has been great emphasis on developing IVPA/IVUS techniques for both pre-clinical and clinical use. Although the commercialization of IVPA would be a useful tool for plaque detection, a more noninvasive PA method could also improve lesion characterization in a wide variety of patients who are at risk for vascular disease. The use of IVPA/IVUS on all patients is unrealistic, especially patients who are asymptomatic or do not fall into the category of a "high-risk" patient. The development of noninvasive transcutaneous PA imaging would allow clinicians to rapidly scan a wide variety of patients that would not be imaged otherwise. The development of a noninvasive tomographic PA technique will also allow scientists to better utilize the technology for small animal studies of atherosclerosis progression.

The limitation of lipid-based PA imaging is that current penetration depth under 1 cm, which is why many atherosclerosis studies are currently limited to small animal models. The advancement of a clinical noninvasive PA technique may be achieved by optimizing current PA protocols to deliver more light to tissue by improving laser power, method of light delivery, etc. In fact, many articles have been published describing various probe configurations and image reconstruction techniques for PA imaging.[94; 131-136] These configurations can be used to optimize light delivery to tissue to improve compositional contrast. With proper optimization of the technique penetration depth can be improved up to several centimeters,[137] making PA imaging more applicable for clinical use.

It is also important to focus on PA laser safety as it relates to medical professionals, patients, and researchers. While PA imaging does not require ionizing radiation or harmful contrast agents, high power lasers are often used. Therefore, special precautions must be taken to prevent laser-induced injuries, specifically to the eyes and skin. Eye injuries can be prevented by mandating laser safety goggles, with the appropriate optical density, to be worn during PA imaging. Moreover, laser induced burns can be prevented by following the American National Standard Institute (ANSI) safety standards[81; 138; 139] for laser use in health care. By following

these guidelines, injury to patients, physicians, and researchers can be minimized or even eliminated.

There have also been efforts focused on contrast enhanced PA imaging. While contrast enhanced imaging is useful to study disease progression, the translation from bench to bedside currently seem limited due to the potential cytotoxic effects of various contrast agents. Their use, however, can play an important role in experimental studies of atherosclerosis. Therefore, another area of PA imaging that could be explored is the development of safe PA contrast agents that target various areas of atherosclerosis pathophysiology such as LDL infiltration, smooth muscle cell migration, and collagen deposition. The development of contrast agents and noninvasive PA techniques will allow clinicians and researchers to perform in vivo compositional and molecular targeting studies of early plaque (Type I-IV) development. Overall, PA imaging has potential to play a complementary role in atherosclerosis imaging alongside other currently used modalities.

2.6 Conclusion

In recent years we have observed great strides in the development and applications of PA imaging towards the study of atherosclerosis. While there is still more work to be done, PA imaging has shown promise as a rapid, cost effective, minimally invasive modality for atherosclerosis imaging. Previous imaging techniques can effectively detect stenosis in middle-later stages of arterial plaque development, but novel techniques are needed to characterize plaque composition and diagnose high risk lesions at an earlier time points. The use of PA imaging is promising as it can be easily coupled with ultrasound to provide anatomical, molecular, and compositional information of tissue without the need of ionizing radiation. The optimization of PA imaging may indeed allow for the study of plaque formation in greater detail, thereby enabling clinicians and scientists to better characterize lesion formation, evaluate therapeutics in small animal models, and perform *in vivo* human studies aimed at better quantifying atherosclerosis progression.

2.7 Acknowledgement

The authors would like to thank Andrea Chambers, Matthew Giarra, Brett Meyers, Evan H. Phillips, Arvin H. Soepriatna, and James R. Wodicka for their editing assistance. Funding was provided by the American Heart Association to Dr. Craig J. Goergen through the Scientist Development Grant (14SDG18220010). There are no conflicts of interest to be disclosed.

3. ULTRASOUND CAPABILITIES FOR MURINE VASCULAR IMAGING

The previous chapter highlights the potential of coupling photoacoustic and ultrasound imaging for clinical characterization of atherosclerosis. Here, we delve deeper into the ultrasound quantification methods that can be employed to characterize changes during cardiovascular disease progression. We will do this by utilizing a surgically induced small animal aneurysm model to quantify the hemodynamic and morphological changes with presence of bilateral iliac artery stenosis. These results will then be compared to clinically relevant case studies. This chapter contains published content from the Journal of Vascular Research entitled, "Effects of Iliac Stenosis on Abdominal Aortic Aneurysm Formation in Mice and Humans." The published version of this chapter is available through the following link: https://doi.org/10.1159/000501312

3.1 Abstract

Reduced lower limb blood flow has been shown to lead to asymmetrical abdominal aortic aneurysms (AAAs) but the mechanism of action is not fully understood. Therefore, small animal ultrasound (Vevo2100, FUJIFILM VisualSonics) was used to longitudinally study mice that underwent standard porcine pancreatic elastase (PPE) infusion (n=5), and PPE infusion with modified 20% iliac artery stenosis in the left (n=4) and right (n=5) iliac arteries. Human AAA computed tomography images were obtained from patients with normal (n=9) or stenosed left (n=2), right (n=1), and bilateral (n=1) iliac arteries. We observed rapid early growth and rightward expansion (8/9 mice) in the modified PPE groups (p<0.05), leading to slightly larger and asymmetric AAAs compared to the standard PPE group. Further examination showed a significant increase in TGFβ1 (p<0.05) and cellular infiltration (p<0.05) in the modified PPE group versus standard PPE mice. Congruent, yet variable, observations were made in human AAA patients with reduced iliac outflow compared to those with normal iliac outflow. Our results suggest that arterial stenosis at the time of aneurysm induction leads to faster AAA growth with aneurysm asymmetry and increased vascular inflammation after 8 weeks, indicating that moderate iliac stenosis may have upstream effects on AAA progression.

3.2 Introduction

Abdominal aortic aneurysms (AAAs) are a complex and often asymptomatic disease affecting 5-10% of men between the ages of 65 to 79.[140-142] AAA pathophysiology is associated with destruction of elastin and increased collagen turnover in the medial and adventitial layers, resulting in dilation of the vessel. This dilation and change in material properties weakens the arterial wall, increasing the likelihood of life-threatening aortic rupture. The initiation and progression of this disease, however, is multifactorial and influenced by a combination of environmental and genetic factors. AAA growth is coupled with proteolytic degradation of aortic connective tissue, inflammation and immune responses, and increased biomechanical wall stress.[143] The multifactorial nature of aneurysm progression leads to an increased risk of aortic rupture in some patients more than in others.

One under-investigated area of AAA research is how changes in lower extremity flow alter infrarenal aortic hemodynamics and aneurysm expansion. Altered iliac artery flow can be caused by a myriad of factors including atherosclerotic plaque formation, above knee amputations, or muscular inactivity. Vollmar et al. first observed the phenomenon that above-knee amputees developed AAAs that expanded asymmetrically in a study of 1,031 veterans. Not only were AAA more prevalent in the amputee group (5.8% vs. 1.1%), but these patients also developed asymmetric AAAs that expand towards the amputated side of the body.[144] The authors hypothesized that higher incidence of asymmetric AAAs may be due to complex flow patterns in amputees near the aortic bifurcation that cause abnormal mechanical shear stress on the vessel. A later study by Lorenz et al. found that among 545 surgical AAA patients, the incidence of AAA in groups with above and below the knee lower limb amputation compared to controls were statistically indistinguishable after controlling for atherosclerosis risk factors.[145] This study, however, did not investigate the longitudinal effects of altered iliac artery hemodynamics on AAA geometry. Nevertheless, exploring the factors contributing to AAA asymmetry can improve our understanding of how hemodynamics affects AAA formation. Indeed, previous AAA biomechanics studies have shown that aortic curvature and diameter asymmetry are important markers in rupture-risk assessment,[146-149] most likely due to the geometric influences on wall stress.[146; 150] In fact, Crawford et al. showed that altered aortic outflow is associated with AAA rupture at smaller diameters.[151] This suggests that identifying additional metrics may help to develop patient-specific aneurysm growth and risk stratifications.

Additional small animal work has been performed to investigate the effects of altered lower limb outflow on AAA progression. Hoshina et al. showed that rats that had undergone porcine pancreatic elastase (PPE) infusion with left femoral arteriovenous fistula experienced increased aortic wall shear stress of 300% compared to reduced shear stress of 60% in animals that underwent left iliac artery ligation.[152] Comparison of AAA diameters showed that mice that have undergone iliac artery ligation had aortic diameters that were almost twice the size of the femoral arteriovenous fistula groups. Moreover, studies using similar models have shown that reduced wall shear stress induced by iliac ligation may also affect endothelium stability and permeability[153] and medial-adventitial angiogenesis,[154] leading to transmural aortic inflammation. Together, these human and animal studies suggest that altered iliac artery hemodynamics and mechanics have upstream effects on the aorta thereby potentially exacerbating AAA progression, influencing unilateral growth and eventual rupture rates. The presented study utilized longitudinal small animal ultrasound imaging to assess structural and hemodynamic changes in the infrarenal aorta of mice after PPE infusion in combination with modified unilateral iliac stenosis. Additionally, we assessed gene expression and histological changes between mice that had undergone the standard and modified PPE procedures. Our murine results were then compared to human AAA data with and without iliac artery stenosis. We hypothesized that moderate iliac artery stenosis would create regions of disturbed aortic flows, thus causing gene expression and hemodynamic changes within the infrarenal aorta that lead to asymmetric AAA formation with expansion direction correlating to the side of stenosis.

3.3 Materials and Methods

3.3.1 Elastase Infusion Surgery

Ten-week-old male C57BL/6J wild-type mice from The Jackson Laboratory (Bar Harbor, ME) underwent porcine pancreatic elastase (PPE) infusion surgeries. The Purdue Animal Care and Use Committee approved all procedures. Mice were separated into standard PPE (n=5), left partial ligation PPE (n=4), and right partial ligation PPE (n=5) groups. All animals were anesthetized and aseptic technique was used during the procedure. The infrarenal aorta was exposed and infused with 2 U/mL of PPE for 10 minutes (**Appendix A Figure 1)**. Left or right iliac artery was partially ligated by tying a 6-0 silk-braided suture around both the iliac artery and

a 30 gauge needle. The needle was then removed, resulting in vessel stenosis as described previously (**Appendix A Figure 1**;[155]).

3.3.2 Ultrasound Imaging

Mice were imaged using a high-resolution small animal ultrasound system (Vevo2100, FUJIFILM VisualSonics) with a 22–55 MHz transducer (MS550D; 40 MHz center frequency; **Appendix A Figure 2)**. We acquired full ultrasound imaging datasets for all mice prior to surgery (day 0) and on days 3, 7, 14, 21, 28, and 56 after surgery. Long-axis B-mode (**Figure 3.1A-B**) was used to assess vessel diameter, and M-mode (**Figure 3.1C-D**) was used to quantify circumferential cyclic Green-Lagrange strain. Mean and peak blood flow velocities were quantified from pulsed-wave Doppler (PWD) images (**Figure 3.1E-F**) in the middle of the infrarenal aorta, and proximal and distal regions of the iliac arteries. Finally, 3D gated acquisitions of the infrarenal aorta and iliac arteries was performed using a stepper motor that translated across the abdomen on the animal with step size of 193 μm. Further details are described in **Appendix A2-3**.

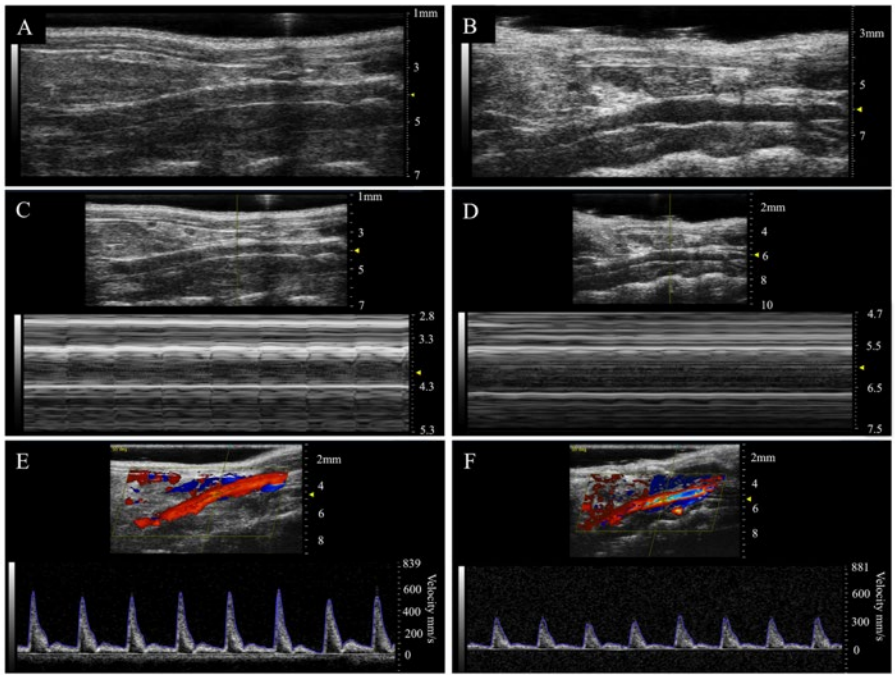

Figure 3.1: Representative healthy (left panels) and aneurysmal (right panels) murine aortae with B-mode (A-B), M-mode (C-D), and PWD (E-F) images. B-mode images were used to assess overall vessel structure and quantify increase in aortic diameter after PPE treatment. M-mode was used to measure circumferential cyclic strain, and PWD was used to quantify mean and peak velocities.

3.3.3 3D Segmentation and Centerline Deviation Quantification

We performed 3D segmentation and centerline deviation analysis using the SimVascular platform[156] on day 0, 28, and 56 murine datasets. Day 0 segmentation was used to assess the morphology of the healthy aorta, which was then used to determine the projected healthy aorta at later time points for comparison (**Appendix A4**). We then calculated the AAA and healthy aortic centerline paths, by identifying the centroid of both segmentations in a short-axis view, to quantify the magnitude and direction of aneurysm expansion. The same centerline deviation protocol was applied to acquired computed tomography images from nine "standard" AAA patients without iliac stenosis and four "modified" patients with either left iliac (n=2), right iliac (n=1), or both left and right iliac artery (n=1) high-grade stenosis. The study was performed according to the Guidelines of the World Medical Association Declaration of Helsinki. The Ethics Committee of Klinikum rechts der Isar, Technische Universitaet Muenchen approved the study, and written informed consent was given by all patients. Computed tomography scan images obtained in the arterial phase were acquired by injecting 120mL of contrast agent (Imeron®) in AAA patients in a supine position with image acquisition time of approximately four minutes. The aortic location of maximum diameter or curvature in cases of tortuous aneurysms was used as representative centerline deviation for comparison between animals/patients.

3.3.4 Histology, Gene Expression, and Immunohistochemistry Experiments

The infrarenal aorta was resected *en bloc* with the adjacent vena cava and kidneys. The bottom half of this tissue segment was dissected to separate the aorta from adjacent tissues, stored in RNA later (Qiagen), and snap-frozen in liquid nitrogen for storage at –80°C. The upper half and adjacent tissues were fixed in 4% paraformaldehyde (Thermo Fisher Scientific) overnight for hematoxylin and eosin (H&E) and Elastica van Gieson (EvG) histology, as well as Ki67 and TGFβ1 immunohistochemistry. ImageJ was used to determine the cellular content in H&E sections by quantifying cell nuclei in three separate randomly chosen 50x50μm^2 regions for each histological section that included the aortic intima and media at 100x magnification[157; 158]. Quantitative RT-PCR was used to assess IL-6, VEGFA, KLF4, and TGFß1 expression in all PPE-infused mice after euthanasia on day 56. All fold changes were expressed compared to

control aortae obtained from 12-14 week old healthy male C57BL/6J wild-type mice (n=6). Finally, Ki67 and TGFβ1 immunohistochemistry was performed overnight with primary antibody (Ki67 1: 200, Abcam; TGF-b-1 1:100, Abcam) incubation at 4°C followed by 30 minute incubation in secondary antibody (goatantirabbit,1:200inPBS-T 5% goat serum). Further details are provided in **Appendix A5-7**.

3.3.5 Human AAA Tissue Acquisition

Human aneurysm tissues were acquired from two AAA patients, one with complete occlusion of the left common iliac artery and one with a right above the knee amputation (**Appendix A8-9**). These patients had undergone open AAA repair with patients' informed and written consent and with approval of the local ethics committee. Samples were taken from opposite sides of the aneurysm sac and stained with H&E and EvG, as well as labeled with anti-CD34 and CD45 antibodies (Abcam) for immunohistochemistry as described previously.[159] The study was performed according to the Guidelines of the World Medical Association Declaration of Helsinki. The Ethics Committee of Klinikum rechts der Isar, Technische Universitaet Muenchen approved the study, and written informed consent was given by all patients.

3.3.6 Statistical Analysis

We used analysis of variance (ANOVA) with Tukey's HSD post-hoc analysis to determine statistical significance for diameter, volume/length, strain, velocity, ΔCt gene expression, cell counting, and centerline deviation magnitude data. Inverse transformation was applied to normally distribute aortic strain data prior to parametric statistical testing. MATLAB CircStat Toolbox was used for centerline deviation direction statistics.[160] All values are reported and plotted as average ± standard deviation, and statistical significance was determined at the $p<0.05$ threshold. More details are provided in **Appendix A10**.

3.4 Results

3.4.1 Morphological Changes in Murine PPE-infused Aortae

We observed a rapid increase in aortic diameter (**Figure 3.2A,D**) at day 14 for both the standard PPE (0.71±0.06 mm to 1.1±0.03 mm; $p<0.001$) and modified PPE (0.71±0.05 mm to

1.1±0.12 mm; $p<0.001$) groups compared to day 0. Interestingly, modified PPE diameter reached statistically significant expansion by day 3 ($p<0.001$) compared to day 7 for the standard PPE group ($p<0.01$). The aortic diameter then steadily increased to 1.2±0.04 mm for the standard PPE group and 1.3±0.15 mm for the modified PPE group by day 56 ($p=0.89$). Aortic volume/length (**Figure 3.2B,E,G**) followed a similar trend with the modified PPE group experiencing rapid expansion in the first seven days (0.48±0.07 mm^3/mm to 0.67±0.06 mm^3/mm; $p<0.001$) and comparatively slower growth in the standard PPE group until day 14 (0.40±0.09 mm^3/mm to 0.61±0.04 mm^3/mm; $p<0.05$). The modified PPE volume/length was also statistically greater at day 7 when compared to the standard PPE group ($p<0.05$). After this rapid expansion period the volume/length steadily increased to 0.69±0.14 mm^3/mm for the standard PPE group and 0.76±0.14 mm^3/mm for the modified PPE group ($p=0.95$; **Appendix A Figure 3**. Conversely, our results showed an overall decrease in infrarenal aorta mean velocity and a significant decrease in average peak velocity between days 0 and 56 for all PPE treated animals. Moreover, we observed an abrupt decrease in Green-Lagrange circumferential cyclic strain measurements (**Figure 3.2C,F**) in the first 7 days post-procedure, with an overall decrease from 11.7±2.6% to 3.1±0.61% ($p<0.01$) for the standard PPE group and 12.2±3.6% to 3.63±0.91% ($p<0.01$) for the modified PPE group. Circumferential cyclic strain remained stable for both the proximal and distal regions of the PPE infused aorta. Velocity and circumferential cyclic strain were higher in the modified PPE group compared to standard PPE, but this difference was not statistically significant. Individual animal ultrasound measurements can be found in **Appendix A Figure 4**.

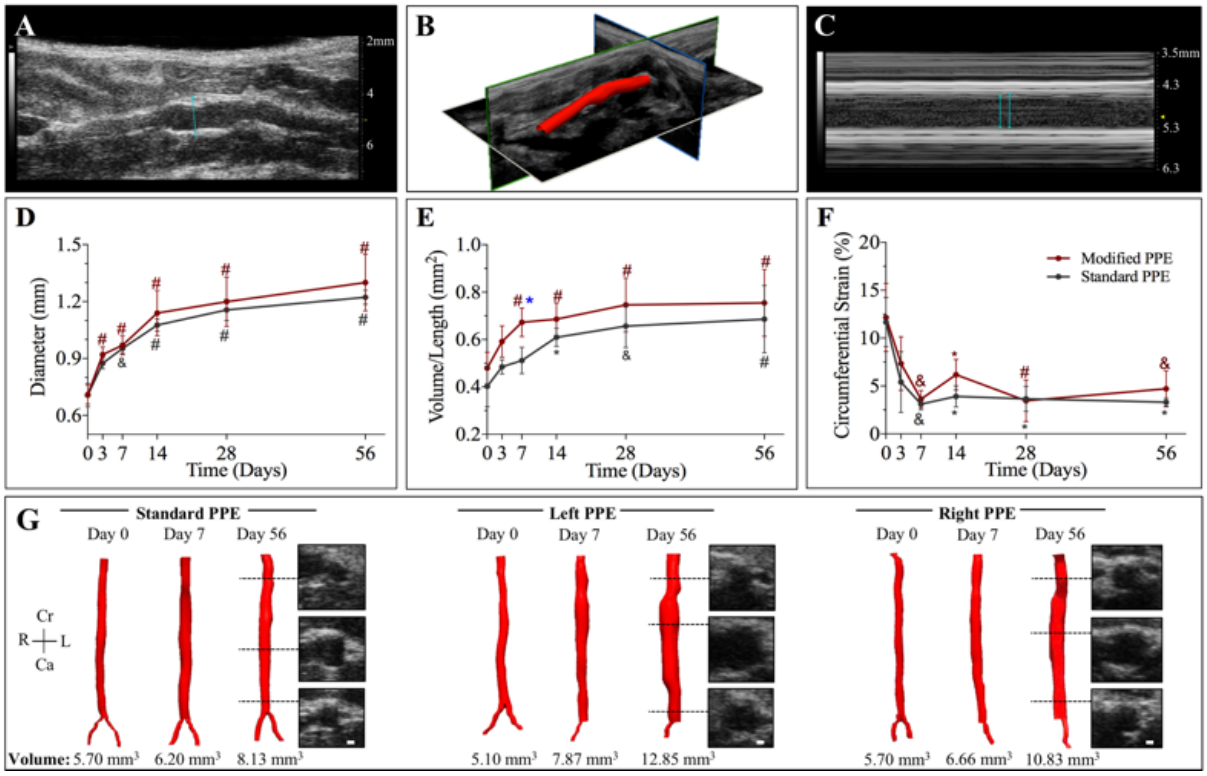

Figure 3.2: Summary of structural changes in murine abdominal aortic aneurysm development among standard, left, and right PPE groups. Long-axis B-mode was used to quantify aortic diameter (A), 3D ultrasound for aortic segmentation and volume characterization (B), and M-mode to quantify systolic and diastolic diameters (C) that were used to assess changes in circumferential cyclic strain. Aortic diameter increases steadily up to day 56 (D) with the modified PPE group having rapid increase in volume/length up to day 7 (E). We also observed a sharp decrease in circumferential cyclic strain between baseline and day 7 post-procedure time points (F). Representative short-axis ultrasound, 3D segmentation, and volume showed slightly larger aneurysm in the modified PPE group compared to the standard PPE group (G). Statistical significance compared with day 0 and defined at $p<0.05$ (*), $p<0.01$ (&), and $p<0.001$ (#). Blue asterisk represents statistical significance between the standard and modified PPE groups. Scale bar denotes 200 µm.

In the iliac arteries, we also quantitatively assessed the effect of vessel stenosis on changes in arterial structure and hemodynamics. (**Figure 3.3A-B**). Day 56 diameter measurements distal to suture placement showed that the partially ligated iliac artery diameter (0.50±0.07 mm) was significantly smaller compared to both standard (0.62±0.063 mm; $p<0.001$) and modified contralateral control (0.60±0.10 mm; $p<0.001$) iliac artery diameters. Further analysis showed iliac artery stenosis of 21% in the right iliac artery PPE group and 19% in the left iliac artery PPE group. Conversely, we did not see significant changes in vessel diameter proximal to sutures with values of 0.67±0.07 mm in the standard PPE group, 0.67±0.09 mm in modified contralateral control arteries, and 0.69±0.06 mm in partially ligated arteries (**Figure 3.3C**). Interestingly, substantial changes were not observed in iliac artery mean velocity among

standard, contralateral control, and partially ligated arteries at day 56. In fact, the standard PPE group showed larger and highly variable mean velocity measurements compared to the modified and contralateral control iliac arteries (**Figure 3.3D, Appendix A Table 1**). Mean and peak velocity data can be found in **Appendix A Figure 4**. Finally, assessment of day 56 vessel pulsatility distal to suture placement (**Figure 3.3E**) showed that the modified iliac arteries had significantly decreased circumferential cyclic strain (2.31±1.13%) compared to the contralateral control vessels (14.2±4.09%; $p<0.001$) and unmodified iliac arteries in the standard PPE group (11.9±2.48%; $p<0.001$). Together, these results indicate that the modified iliac arteries have decreased luminal diameter and patency distal to suture placement.

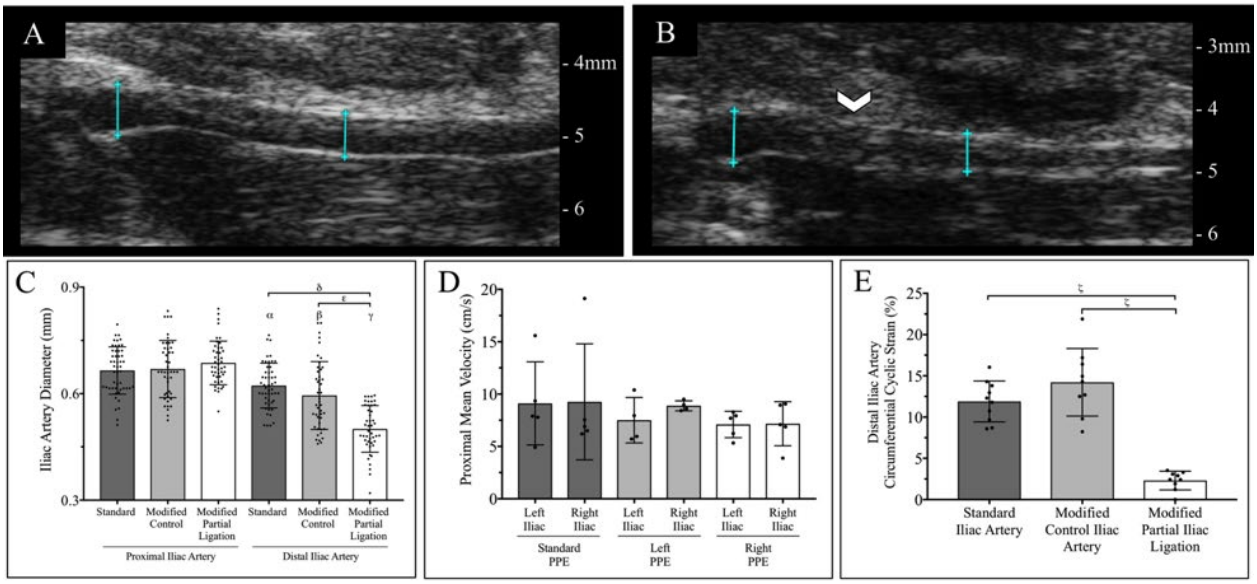

Figure 3.3: Comparison of structural and hemodynamic changes between non-ligated (A) and partially ligated (B) iliac arteries at day 56. We observed significant decrease in diameter (C) and circumferential cyclic strain (E) in modified iliac arteries compared to standard PPE arteries and contralateral control iliac arteries. We did not, however, see significant changes in iliac artery velocity between standard and modified PPE groups at day 56 (D). Suture placement is highlighted by white arrow and diameter measurement locations shown by blue lines. Statistical significance is shown as $p<0.001$ (α, β, γ, δ, ε, ζ). Symbols α, β, γ signify statistical significance between their respective group and the standard, modified control, and modified partial ligation groups in the proximal iliac artery.

Aortic segmentation and centerline deviation analysis (**Figure 3.4A**) was performed on short-axis B-mode images (**Figure 3.4B**) to assess the magnitude (**Figure 3.4C**) and direction (**Figure 3.4D**) of aneurysmal shift in left and right partial iliac ligation groups compared to the standard PPE groups. Day 28 and 56 data analysis showed that standard PPE aortae expansion was heterogeneous, with the mean centerline deviation close to the origin of the Cartesian plane. Interestingly, the left and right partial iliac ligation PPE groups deviated further from the center,

suggestive of more asymmetric expansion (**Figure 3.4E**). Specifically, day 28 results suggest that the left partial iliac ligation PPE group had a centerline shift towards the rightward direction, while the right partial iliac ligation PPE group had a centerline shift towards the leftward direction (**Appendix A Table 2**). This trend shifts by day 56 where we observed rightward expansion in 8 out of 9 modified PPE animals (**Appendix A Table 2**).

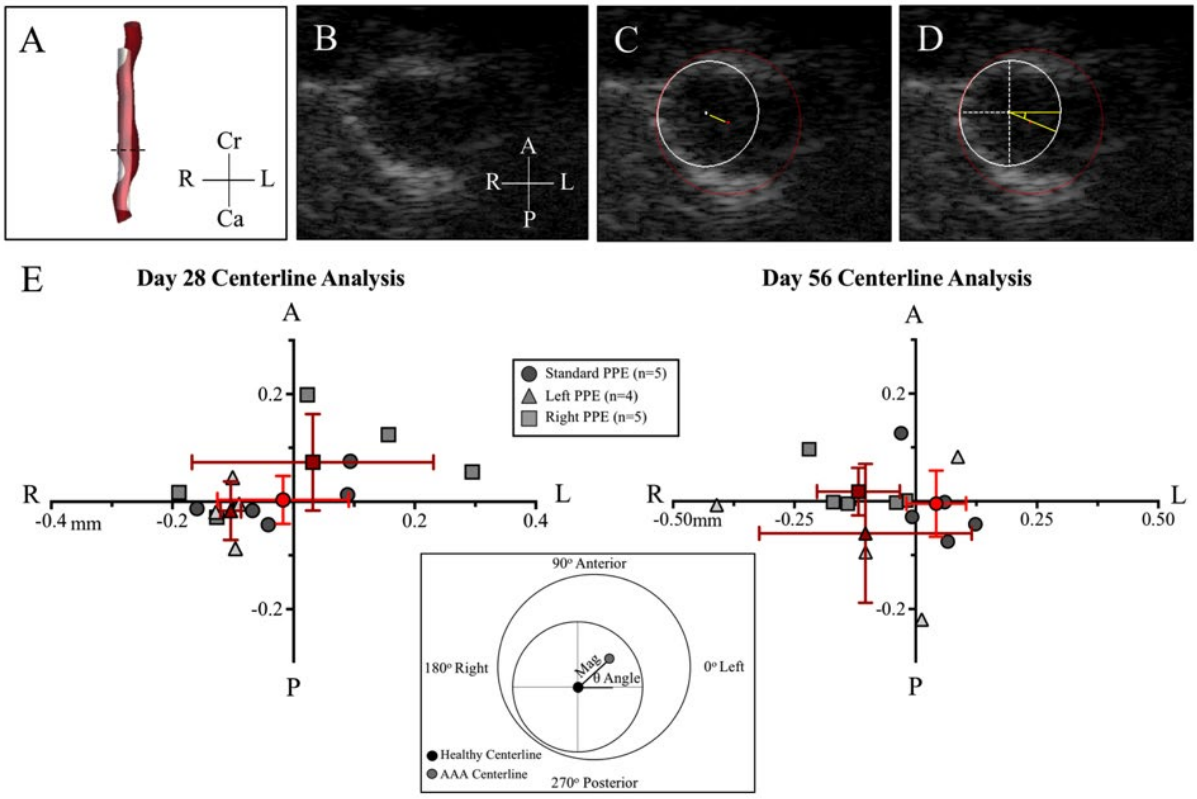

Figure 3.4: Summary of murine centerline deviation analysis methods and results. Aneurysm and projected healthy regions were first segmented using SimVascular (A). We then used short-axis view (B) to quantify magnitude (C) and direction (D) of centerline deviation between the healthy and diseased aorta. Centerline deviation results (E) for day 28 and 56 shows the shift in magnitude and direction of the diseased vessels with respect to the healthy vessel. Red points represent the mean centerline deviation for the standard and modified PPE groups, and the red lines represent the standard deviation in the X and Y axis. Cr: Cranial, Ca: Caudal, L: Left, R: Right, A: Anterior, P: Posterior.

3.4.2 Murine Histology, Gene Expression, and Immunohistochemistry

Based on the H&E stained sections, we observed that standard and modified PPE mice experienced aortic wall thickening (**Appendix A Figure 5** with elastin degradation, collagen turnover, and inflammation not observed in control aortae. Magnified EvG images further confirm varying elastin degradation throughout the aorta in both the standard (**Figure 3.5A-B**) and modified (**Figure 3.5C-D**) groups. Moreover, we observed relatively consistent aortic wall

thickness on both the left and right sides of the modified aortae suggesting homogeneous collagen deposition in the diseased vessels. Qualitative Ki67 immunohistochemistry analysis revealed increased cell proliferation in PPE infused animals (**Figure 3.5F**) with greater signaling in the modified (**Appendix A Figure 5E**) compared to the standard PPE (**Appendix A Figure 5D**) aortae. An in-depth examination of nuclei showed a statistically significant increase in cell number for the standard (p<0.01) and modified (p<0.001) PPE groups compared to untreated controls, as well as between standard and modified PPE groups (p<0.05; **Figure 3.5E**).

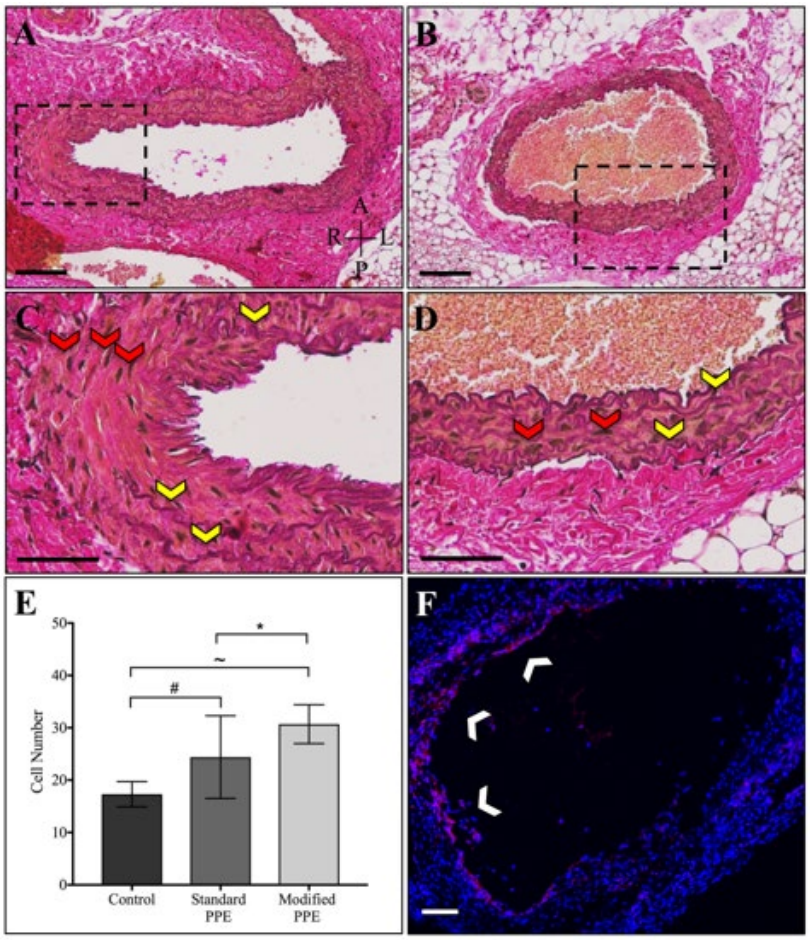

Figure 3.5: Histological and immunohistochemistry analysis of PPE infused aortic tissue consisting of EvG stained standard (A,C) and modified (B,D) aortae, as well as Ki67 stained modified (F) infrarenal aorta. Histology showed diffuse elastin breakage throughout the vessels (yellow arrows), thus confirming aneurysm induction. Ki67 staining revealed cell proliferation in the modified PPE animals (white arrows). Further, cell number analysis showed significant increase in cell nuclei (red arrows) between the modified and standard PPE infused aortae (E). A: Anterior, P: Posterior, L: Left, R: Right. Scale bar A, C, F denotes 100 μm, and B and D denotes 50 μm. Statistical significance is defined at p<0.05 (*), p<0.001 (#), p<0.0001 (~).

For further validation, we measured exemplary upregulation of growth factor and inflammatory genes. In the standard group, the inflammatory cytokine IL-6 (5.1±3.8 fold

increase; **Figure 3.6A**) and AAA-associated growth factors VEGFA (1.7±0.20 fold increase; **Figure 3.6B**) and TGFβ1 (3.0±1.8 fold increase; $p<0.05$; **Figure 3.6C**) were all upregulated compared to control aortae. The flow-dependent transcription factor KLF4 was downregulated (0.66±0.24 fold change; **Figure 3.6D**). These results are also consistent with our modified group where we observed upregulation of IL-6 (3.6±1.4 fold increase), VEGFA (3.0±1.9 fold increase), and TGFβ1 (6.6±1.9 fold increase; $p<0.0001$). On the protein level, immunohistochemistry confirmed higher expression of TGFβ1 in standard (**Appendix A Figure 5G,J)** and modified PPE (**Appendix A Figure 5H,K)** when compared to control aortae (**Appendix A Figure 5I,L).** Interestingly, we observed statistically significant increases in TGFβ1 between the standard and modified groups ($p<0.05$). Modified KLF4 expression showed large variation from the mean with downregulation in the left PPE group (0.69±0.24 fold decrease) and upregulation in the right PPE group (1.6±1.2 fold increase).

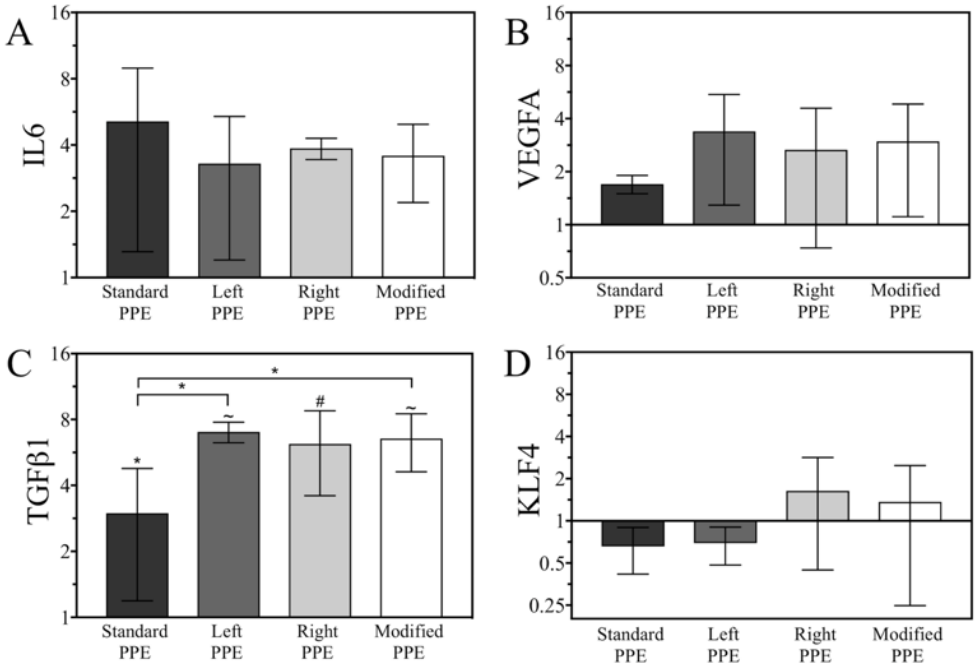

Figure 3.6: Relative gene Expression analysis of standard and modified infrarenal aortae at day 56 using qPCR. IL-6 (A) and VEGFA (B) are upregulated, but there are no significant differences between PPE infused and control aortae. TGFβ1 shows significant upregulation between PPE infused and control aortae, and standard and modified groups (C); while KLF4 (D) shows variable differences in expression between standard and modified groups. Fold change values are relative to control aortae. Statistical significance is defined at $p<0.05$ (*), $p<0.001$ (#), and $p<0.0001$ (~).

3.4.3 Human AAA Centerline, Histology, and Immunohistochemistry

Aortic segmentation and centerline deviation analysis (**Figure 3.7A-B**) was performed on human AAA data to assess the magnitude and direction of aneurysm growth (**Figure 3.7C**). Overall, we observed that the healthy iliac (standard) AAA group had an average centerline deviation of 13.8±13.35 mm and the iliac stenosis/occlusion (modified) group had an average centerline deviation of 12.9±4.43 mm (p=0.33). Interestingly, we saw anterior and leftward expansion of the AAA away from the spine and inferior vena cava for both the standard (75.5±25.6^{o}) and modified (46.0±13.8^{o}) groups (**Figure 3.7D**). A closer look at the human datasets show that the center of the standard healthy aorta was shifted leftward laterally with respect to the center of the spine with a distance of 5.72±3.08 mm. Patients with left or right iliac occlusion had an increased leftward lateral shift of 10.6±1.93 mm, while the patient with both iliac occlusions had a leftward lateral shift of 2.05 mm. Finally, histological analysis was performed on the left and right lateral sides of the aneurysm sac, at the level of maximum diameter, for two patients with either left iliac artery occlusion or right knee amputation. Different lateral aneurysm wall morphology and cellular content was seen with H&E and EvG staining, as well as CD34 and CD45 immunohistochemistry (**Appendix A Figure 6**). Examination of H&E staining of left side of the AAA sac showed increased cellular infiltration, while EvG staining revealed extensive breakdown of elastin laminar units throughout the AAA. CD34 and CD45 staining revealed increased inflammatory infiltration on the left side of the aneurysm for both AAA patients. Overall, we observed distinct difference in morphology when comparing the left and right side of these aneurysms, as well as inflammatory activity (CD45) and angiogenesis (CD34).

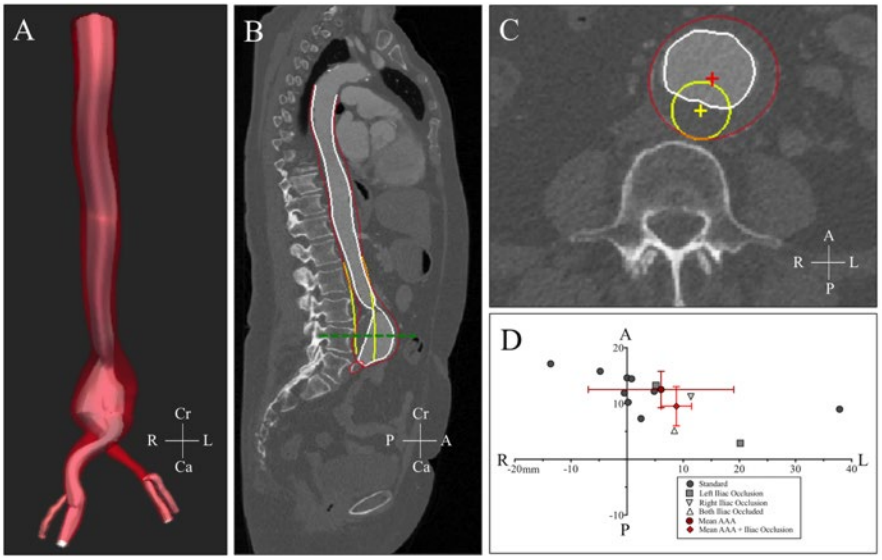

Figure 3.7: Summary of human centerline deviation analysis methods and results. 3D segmentation was performed on human AAA (A) and sagittal cross-sectional plane was used to confirm quality of 3D segmentation with red, white, and yellow highlighting AAA wall, AAA lumen, and projected healthy aorta (B). Transverse cross-sectional plane along the center of the AAA (green dotted line) was used to quantify magnitude and direction of centerline deviation (C). Quantitative analysis shows that standard and modified AAA grew away from the spine in the leftward direction, likely due to the natural leftward origin of the healthy aorta. Red points represent the mean centerline deviation for the standard and modified PPE groups, and the red lines represent the standard deviation in the X and Y axis. Cr: Cranial, Ca: Caudal, L: Left, R: Right, A: Anterior, P: Posterior.

3.5 Discussion

In this study, we investigated the effects iliac stenosis has on asymmetric AAA formation. This work was motivated by the observation that patients with above the knee amputations formed asymmetrical AAAs, potentially due to disturbed flows that produce high shear zones and increased mechanical stress on the aortic wall.[144] Therefore, we attempted to replicate this phenomenon in a small animal model of AAAs to study how vessel hemodynamics longitudinally affects AAA formation and growth. Understanding asymmetrical AAA formation is important, as disturbed iliac flow may lead to increased endothelium permeability and medial-adventitial angiogenesis, both of which have been shown to increase aortic inflammation that can potentially exacerbate AAA development and rupture.[153; 154; 161]

The PPE infusion murine model combined with an iliac artery stenosis was utilized to evaluate the effects restricted lower limb blood flow has on aneurysm formation in the infrarenal aorta as previously presented by Vollmar et al. Low dose PPE (2 U/mL) was used to create aneurysms that mimic early AAA progression and male mice were used in this initial study as AAA disproportionally affects men and to minimize sex-specific effects. Our gene expression

results confirmed that low dose PPE induces an inflammatory response as shown by the upregulation of IL-6[162; 163] and VEGFA[164] in both the standard and modified PPE groups, suggesting upregulation of extracellular matrix proteinases.[162] Histological analysis of standard and modified PPE groups showed diffuse elastin breakdown with the modified PPE group having greater cell infiltration compared to standard PPE group ($p<0.05$). Additionally, ultrasound imaging showed a reduction in arterial velocity and 61% increase in volume/length from days 0 to 56, as well as a rapid reduction in circumferential cyclic strain, providing quantitative evidence of decreased pulsatility due to changes in arterial material properties. These results are consistent with previous works that show that a low concentration of PPE results in elastin degradation and collagen turnover, both of which result in hemodynamic and morphological changes in the vessel.[155; 165] Lastly, a decrease in iliac circumferential cyclic strain distal to the suture placement provided evidence that the partial iliac artery ligation increased peripheral vessel stiffness.

AAA asymmetry was quantified by performing 3D segmentation of the projected healthy, standard PPE, and modified PPE infrarenal aortae, followed by the quantification of the magnitude and direction of centerline deviation. Previous work has shown PPE induced dynamic changes in centerline deviation up to day 28 after PPE infusion in mice;[166] therefore, we increased the length of our study to 56 days to quantify the effects of iliac stenosis on centerline deviation over a longer timeframe. Interestingly, day 56 results showed that both the left and right PPE groups had a rightward centerline shift (8 of 9 mice), possibly due to supportive surrounding tissues and a new equilibrium of proteolytic and stabilizing aortic wall activity. Assessment of the iliac artery PWD showed only antegrade blood flow, suggesting that iliac stenosis alone may not be enough to induce disturbed retrograde flows in the infrarenal aorta. In fact, mice do not experience reversal of flow in the infrarenal aorta as commonly observed in healthy humans, thus highlighting species-specific hemodynamic differences that may account for the lack of exacerbated aortic disturbed flow.[167]

Pulsed wave velocity, however, provides bulk flow information along the beam axis and lacks the capability to detect small changes in velocities along the vessel wall that may induce abnormal shear stress.[168] Therefore, we assessed changes in endothelial flow-dependent KLF4 gene expression[169] which showed a limited trend between the standard and modified PPE groups. Specifically, we saw KLF4 down regulation in the left iliac stenosis PPE group and upregulation

in the right iliac stenosis group, thus creating large variability the combined modified group. We did, however, observe a significant decrease in the modified left iliac artery mean and peak velocities at days 28 ($p<0.001$) and 56 ($p<0.05$). Additional quantification of iliac artery structure and hemodynamics showed similar proximal diameter and velocity values between the modified iliac artery and contralateral control. Characterization of distal iliac artery showed variable changes in blood flow velocity but did show significant decrease in circumferential cyclic strain and approximately 20% stenosis compared to the day 0 baseline measurements. These results suggest modest changes in iliac artery mechanics that may have had upstream effects on the aorta, which accelerated early murine aneurysm growth. One possible explanation for the lack of significant flow changes in the iliac arteries is the moderate stenosis of the iliac artery combined with the possible formation of collateral vessels over the eight week period in response to decreased blood flow to the lower limb.[170] Another consideration is that murine aortae trifurcate into the left and right iliac artery, as well as a tail artery. Significant flow changes in the iliac arteries may also be mitigated due to compensations caused by tail artery remodeling. Interestingly, we observed a significant upregulation of TGFβ1 in the modified PPE groups relative to the standard group ($p<0.05$). While the role of TGFβ1 on AAAs progression is still somewhat uncertain,[171; 172] silencing has been shown to prevent AAA formation in PPE infusion and angiotensin II murine models.[171; 173] This suggests that the upregulation of TGFβ1 reported here may be promoting AAA formation in animals with partial iliac ligation. Closer examination of the data also revealed that mice with modified iliac outflow experience rapid early aneurysm growth in the first seven days after AAA induction compared to mice without iliac stenosis ($p<0.05$). This is interesting as the time between aneurysm induction and growth plateau is considered the most active arterial remodeling period in the murine PPE infusion model.[174] Future work could utilize other mouse models, such as the topical periadventitial PPE applications,[175; 176] where significant arterial remodeling can be observed beyond three weeks of AAA induction due to pronounced inflammatory activity.[177] Additionally, sample size should also be increased by additional studies to improve the power of the results and to more clearly resolve gene expression differences between groups. Taken together, while retrograde flow was not detected with our methods, there could be fine changes in the iliac artery mechanics and hemodynamics that have upstream implications in AAA induction and growth.

Finally, centerline deviation was also quantified in human AAAs to better elucidate the effects of iliac atherosclerotic disease and AAA development. Quantifying CT data from 13 AAA patients (9 controls and 4 with high-grade iliac stenosis) revealed that on average, aneurysms shifted both in the anterior and leftward directions. While the number of patients is small, this expansion could be partially attributed to posterior aortic support provided by the spine and right lateral support provided by the inferior vena cava. The findings may also suggest that the left lateral side of the aneurysm may be weaker and prone to enlargement.[178] Further work will be needed to determine if rupture on the left side of AAAs is pattern that could potentially be used to improve risk stratification. Furthermore, our results suggest that above the knee amputations and iliac artery occlusion likely have different effects on infrarenal aorta hemodynamics, potentially due to the grade of stenosis and rate of collateral artery formation in the lower limbs. Collateral remodeling may compensate in some ways for iliac stenosis on aortic flow over extended periods. Conversely, and more consistent with our sudden onset model, above the knee amputation results in a rapid increase in vascular resistance,[179; 180] which may exacerbate the disturbed triphasic flow pattern commonly observed in the infrarenal aorta,[167; 180] possibly increasing the chances of asymmetric AAA formation. Validation in a larger human image dataset supported by further animal studies are needed for a true quantitative discrimination of the effects that iliac occlusion has on infrarenal aorta hemodynamics.

3.6 Conclusion

We show here that modified iliac outflow in mice leads to faster AAA growth and slightly larger aneurysms after 8 weeks, with variable time-dependent centerline shift and altered aneurysm morphology. Additionally, characteristic molecular patterns of AAA formation, such as TGFβ1 expression, were altered in animals with iliac stenosis. Human AAA patients showed leftward expansion of the aneurysm with highly variable centerline shift, regardless of iliac stenosis. Taking both mouse and human data into account, these results suggest that moderate iliac stenosis may have flow-dependent upstream effects on early AAA formation and progression due to a differential cellular activity in the aneurysm wall.

3.7 Acknowledgments

The authors would like to acknowledge Andrea Chambers for her ultrasound imaging assistance. Funding was provided to Dr. C.J.G through the AHA Scientist Development Grant (14SDG18220010), G.S.S. and A.G.B through the NSF Graduate Research Fellowship (DGE-1333468), and G.S.S. through the NIH T32 Bioengineering Interdisciplinary Training for Diabetes Research (T32DK101001-05).

4. PHOTOACOUSTIC METHODOLOGY FOR IN VIVO LIPID IMAGING

Lipid-based photoacoustic advancements have been primarily limited to clinical applications for atherosclerosis characterization. Moreover, numerous studies have been published exploring the use of photoacoustic imaging using the visible light spectrum. Here, we explore the use of the second near-infrared window to noninvasively image lipid and blood in mice. These preclinical applications show the potential to use photoacoustic imaging to study cardiovascular disease progression. This chapter contains published content from the Biomedical Optics Express entitled, "In Vivo Photoacoustic Lipid Imaging in Mice Using the Second Near-Infrared Window." The published version of this chapter is available through the following link: https://doi.org/10.1364/BOE.8.000736

4.1 Abstract

Photoacoustic imaging has emerged as a promising technique to improve preclinical and clinical imaging by providing users with label-free optical contrast of tissue. Here, we present a proof-of-concept study for noninvasive *in vivo* murine lipid imaging using 1210 nm light to investigate differences in periaortic fat among mice of different gender, genotypes, and maturation. Acquired lipid signals suggest that adult male apoE$^{-/-}$ mice have greater periaortic fat accumulation compared to adolescent males, apoE$^{-/-}$ females, and wild-type mice. These results demonstrate the potential of photoacoustic tomography for studying vascular pathophysiology and improving the diagnosis of lipid-based diseases.

4.2 Introduction

Lipid-based diseases account for a significant portion of Western world mortality.[6; 181; 182] Clinical manifestations of lipid-based conditions appear in a multitude of debilitating disease states that include diabetes, obesity, fatty liver disease, demyelination, and vascular diseases such as coronary artery disease and peripheral artery disease. As a result, many imaging techniques including ultrasonography, magnetic resonance imaging, positron emission tomography, x-ray angiography, and optical imaging have been developed to better characterize these conditions. While these imaging modalities can be effective in studying a wide variety of disease states, each has its own inherent limitations such as high cost, limited penetration depth, and/or long imaging times.[183] Therefore, there is still a need to develop techniques that can better characterize compositional information in a rapid, label-free, noninvasive manner that complements currently used imaging methods.

Photoacoustic tomography (PAT) is an emerging modality that can improve *in vivo* disease characterization in humans and animals.[183; 184] Compared to traditional photoacoustic techniques, PAT, using the second near-infrared window, provides optical-dependent contrast that allows users to differentiate biological components such as blood and fat.[185; 186] This contrast is produced by using pulsed laser light to induce a transient temperature rise in tissue that causes acoustic wave propagation. These acoustic waves are acquired to reconstruct an image that displays the relative density and location of biological components. PAT also allows the user to tune the wavelength of light to monitor the excitation of distinct molecular overtones. For instance, the second overtone vibrations of the CH_2 bonds can be detected by using 1210 nm light to identify lipid deposition.[183] When overlaid with ultrasound images, we obtain anatomical and compositional information that other modalities cannot easily provide. In fact, previous *ex vivo* and intravascular studies have shown that PAT can identify mild fatty streaks and discriminate between fibrous and lipid-rich plaques.[184] Despite the exciting potential of PAT, its use in noninvasive *in vivo* imaging of lipid-based murine disease models to better understand disease initiation and progression has not been explored.

Here we present our findings on how PAT can be utilized to study lipid accumulation in hyperlipidemic mice. We focused on the periaortic fat in mice, as it is ample, metabolically active, and accumulates throughout the vasculature. Studying excessive periaortic fat may also have clinical implication as it is involved in cardiovascular and metabolic dysfunction.[187] We

hypothesized that PAT can be utilized to image and detect significant differences in lipid accumulation between apolipoprotein E-deficient ($apoE^{-/-}$) and wild-type (WT) mice. The methods and results in this paper are significant as this is the first report to our knowledge that utilizes long wavelength PAT for noninvasive *in vivo* lipid detection in mice.

4.3 Materials and Methods

$ApoE^{-/-}$ (n=17) and WT (n=10) mice were obtained from Jackson Laboratory (Bar Harbor, ME) and fed a standard chow diet. These mice were separated into six distinct groups based on gender and maturation as shown in **Table 4.1**.[188] A small animal anesthesia system (SomnoSuite, Kent Scientific;[189]) was used to keep the mouse under anesthesia using 1.5-3% isoflurane and 225 mL/min room air. Prior to imaging, eye lubricant was applied to each animal to prevent corneal desiccation. We kept rectal temperature at roughly 34-36°C with a heated stage and monitored this using a rectal probe. Furthermore, heart rate was maintained between 450-600 beats per minute while respiration rate was kept between 40-80 breaths per minute and monitored using electrodes built into the heated stage.

Table 4.1: Summary of the Characteristics for Experimental Mouse Groups

Genotype	**apoE-/-**				**WT**	
Gender	Male		Female		Male	
Maturation	Adolescent	Adult	Adolescent	Adult	Adolescent	Adult
n	5	4	4	4	5	5
Age (months)	2.96±0	11.7±2.7	2.69±0.2	9.40±0	2.79±0	5.99±0.20
Weight (g)	30.3±1.0	32.2±2.1	23.8±2.5	32.8±3.9	26.3±2.9	32.8±4.7

We used a high-frequency small animal ultrasound system (Vevo2100, FUJIFILM Visual Sonics) equipped with a 40 MHz center frequency transducer (MS550D) to obtain *in vivo* long-axis B-mode and PAT images of the infrarenal aorta. A Nd:YAG pulsed optical parametric oscillator (OPO) laser (NT352C, Ekspla) capable of producing 670 to 2300 nm light was used to generate 5 ns pulses at 10 Hz. Our system design has been previously summarized[186] and has been recapitulated in **Figure 4.1**. A function generator (4013B, B&K Precision) was used to synchronize pulse excitation and image acquisition between the laser and the ultrasound, and a pulse generator (9200, Quantum Composers) was used to coordinate the trigger of the laser with the ultrasound system. The function generator specifically produced a 10 Hz, 5 V square

waveform. This setup provided us an ultrasound axial spatial resolution of 40 µm with pixel size of 13.2x55.0 µm (axial x lateral), and PAT axial spatial resolution of 124 µm with pixel size of 28.4x26.6 µm.[186]

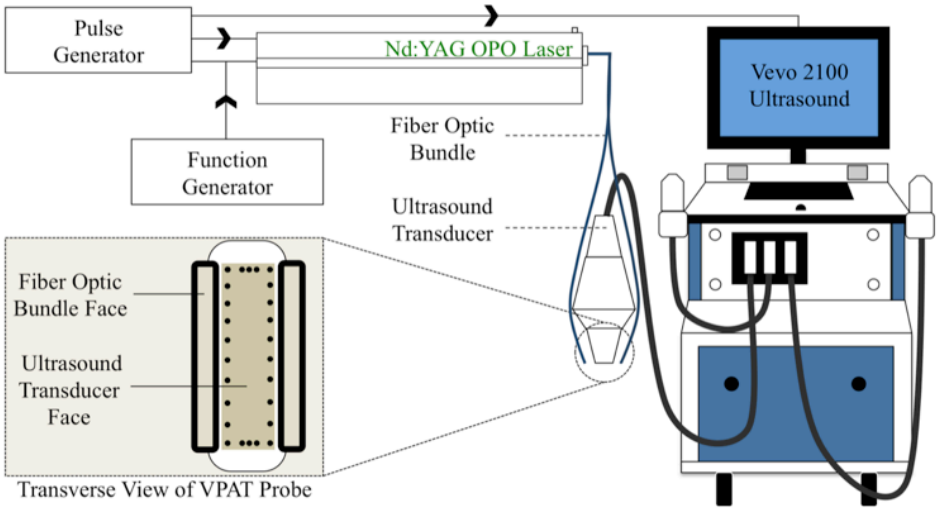

Figure 4.1: Schematic depicting PAT setup. Nd:YAG OPO laser delivered light through a fiber optic bundle to an anesthetized mouse. A 40 MHz center frequency transducer was used to acquire the resulting PAT signal. A function generator coordinated pulse excitation and image acquisition between the laser and the Vevo2100 ultrasound system. A pulse generator was used to synchronize the trigger of the laser with the ultrasound system. The ultrasound transducer face is 20x5 mm and fiber optic bundle face is 12x2 mm.

In this study, 1210 nm light was used to detect periaortic fat signal along the anterior wall of the infrarenal aorta (**Figure 4.2**;[185]) of apoE$^{-/-}$ and WT mice (**Table 4.1**). We used 1100 nm light to detect blood signal [186] within the lumen of the aorta and 1250 nm light as a negative off-resonance control [185]. Photoacoustic images were acquired with a priority of 80%, gain of 30 dB, power of 100%, brightness of 50, and contrast of 50 in the Vevo2100 system. Priority was decreased to 80% to shift the image intensity histogram leftward by 20%. This eliminated many of the background pixels and provided us with better lipid contrast. We chose to remove 20% as it ensured that no part of the histogram was truncated. To minimize minor PAT signal fluctuations and background noise we acquired ten PAT images for each wavelength and computed the pixel-wise arithmetic mean (**Figure 4.3A**). We then performed a thresholding technique to discriminate lipid and background signal. A new histogram of each image was obtained, which produced two peaks that represented the background and lipid signal (**Figure 4.3B**). A threshold point, in the trough of these two peaks, was chosen to assign pixels a value of 255 if their value was greater than or equal to that of the threshold and assigned 0 otherwise.

This PAT mask was overlaid on a grayscale PAT image to confirm the accuracy of our thresholding technique (**Figure 4.3C**). If the mask did not properly align on the grayscale PAT image, the threshold was either increased or decreased by a value of 10 until the mask aligned with the grayscale image. We then plotted the profile of pixel intensities along multiple lines of interest extending anterior to posterior (**Figure 4.3D**). The width of the periaortic fat peak was measured to quantify lipid accumulation on the aorta (**Figure 4.3E**). This thresholding method was repeated 10 times for each mouse (270 total measurements) to take into account measurement variability. Oil Red O (ORO) lipophilic staining was performed to confirm presence of periaortic fat on an excised mouse aorta. Finally, an ANOVA with a Tukey post-hoc statistical test was used to determine significance between groups ($p<0.05$).

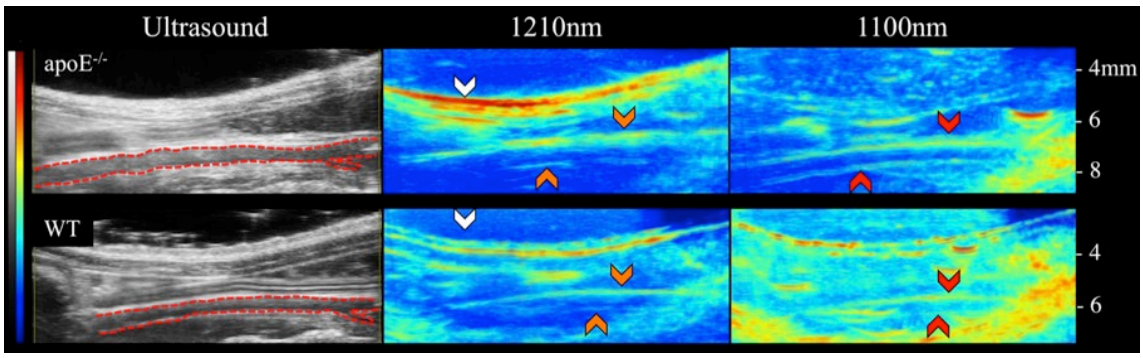

Figure 4.2: Ultrasound (left), lipid PAT (middle), and blood PAT (right) images of adult male apoE$^{-/-}$ (top) and WT (bottom) mice. Images are shown such that the animals are orientated in supine position with the head located to the left and tail is located to the right. Greater periaortic fat signal is evident in the apoE$^{-/-}$ mouse compared to the WT mouse. Using these images we can clearly discriminate the infrarenal aorta (red dotted outline), subcutaneous fat (white arrows), periaortic fat (orange arrows), and blood (red arrows).

4.4 Results

Using our PAT setup we were able to resolve subcutaneous and periaortic fat buildup in both apoE$^{-/-}$ and WT mice. We clearly observed lipid specific PAT signal that followed both the geometry of the skin due to the subcutaneous fat and infrarenal aorta due to periaortic fat accumulation. The adult male apoE$^{-/-}$ mice also showed more subcutaneous and periaortic fat accumulation compared to the adult male WT mice (**Figure 4.2**). To confirm that our lipid signal is coming from periaortic fat, we performed ORO staining on excised aortae of apoE$^{-/-}$ mice. We observed that the entire vessel stained red, confirming the presence of periaortic fat (**Figure 4.3F**). This suggests that our lipid signal is indeed coming from fat buildup on top of the vessel.

All vessels that underwent this ORO process stained red, making it challenging to detect differences in periaortic fat between mice, thus highlighting the benefits of PAT.

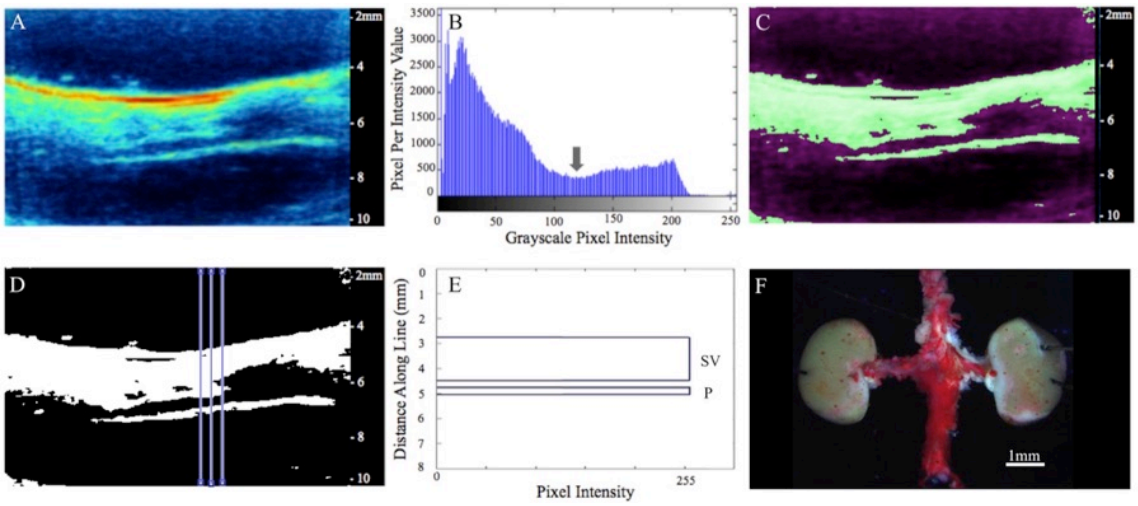

Figure 4.3: Averaged PAT image (1210 nm) reveals subcutaneous and periaortic fat (A). Histogram of PAT pixel intensities shows peaks for background and lipid signal (B). Gray arrow represents threshold point used to create PAT mask, which is overlaid on the original PAT image to confirm thresholding accuracy (C). Plot profile analysis was used to measure periaortic thickness at multiple locations (D). Width of top peak (SV) represents subcutaneous and visceral fat and width of bottom peak (P) represents periaortic fat from one plot profile measurement (E). ORO staining on excised aorta confirms periaortic fat accumulation (F).

Prior to quantifying periaortic fat accumulation, we validated our analysis technique to ensure accurate quantification of lipid signal. First, we confirmed that our thresholding technique provides reliable measurements by measuring the inner diameter of polyethylene 50 (PE50) tubing. This was accomplished by acquiring 1100 nm PAT images of a murine blood filled PE50 tube. The thickness of the blood signal was measured at three locations along the tube and compared to the known inner diameter (0.58 mm). Using our threshold algorithm we obtained an experimental inner diameter of 0.553±0.012 mm, resulting in a percent error of 4.7%. This variation is possibly due to differences in acoustic speeds through water and PE50 tubing. We also showed that there is no measurement variation due to respiratory or cardiac motion by quantifying lipid thickness in both the raw PAT and the pixel-wise arithmetic mean images. To prevent measurement bias we quantified thickness at the same location throughout the aorta (**Figure 4.4**). Our analysis showed respiratory and cardiac motion does not affect our results, as there are no statistically significant differences in fat thickness between the raw and mean images ($p>0.05$). Furthermore, we observed greater lipid signal towards the surface of the mouse due to

progressively fewer photons reaching deeper structures. To overcome this limitation we used lipid thickness as our quantification marker rather than signal intensity.

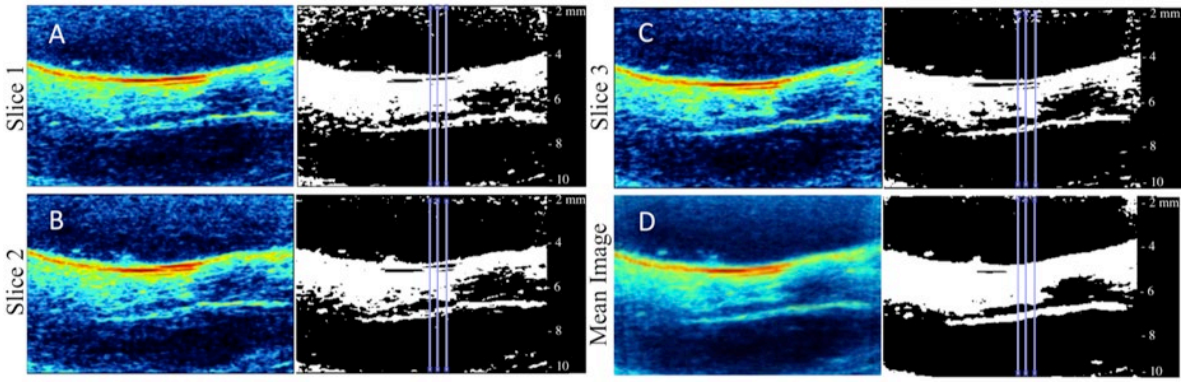

Figure 4.4: Three representative raw 1210 nm PAT measurement images (A-C) and mean (D) image of an apoE$^{-/-}$ mouse. Measurements were taken in same location in all images.

We then used our thresholding technique to quantify lipid thickness in adolescent male (0.24±0.06 mm), adult male (0.46±0.12 mm), adolescent female (0.24±0.08 mm), and adult female apoE$^{-/-}$ (0.21±0.03 mm) mice, as well as in adolescent (0.19±0.04 mm) and adult (0.25±0.06 mm) male WT mice (**Figure 4.5**). Adult male apoE$^{-/-}$ mice have significantly greater periaortic fat compared to other apoE$^{-/-}$ and WT groups ($p<0.01$).

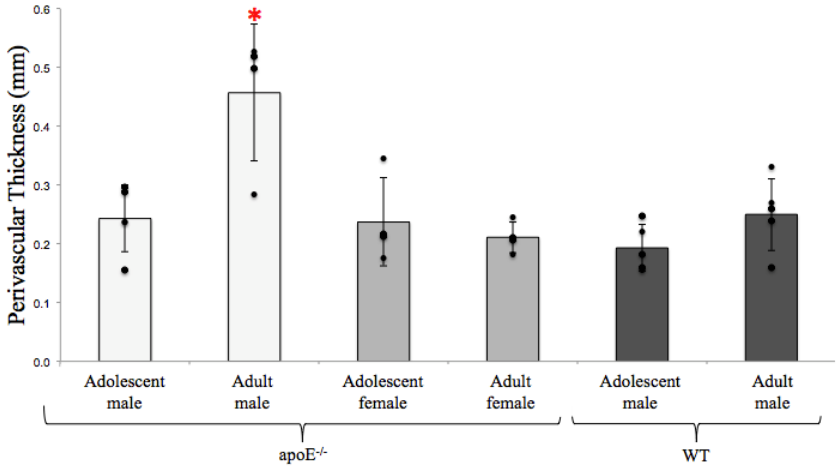

Figure 4.5: Periaortic thickness values in apoE$^{-/-}$ and WT groups. Adult male apoE$^{-/-}$ mice have significantly higher periaortic thickness compared to other groups ($p<0.05$).

4.5 Discussion

In this study we evaluated the hypothesis that PAT can be used to image and quantify periaortic fat accumulation *in vivo*. By coupling a high frequency ultrasound system and a pulsed

laser, we were able to acquire images of subcutaneous and periaortic fat. We are certain that our PAT images provide lipid-specific signal for multiple reasons. We specifically utilized 1210 nm light to excite the second overtone vibrations of CH_2 bonds, which are abundantly found in lipids [184]. The *in vivo* subcutaneous fat signal also follows the geometry of the skin, while the periaortic fat signal follows the geometry of the aorta. Finally, we confirmed that our images are indeed detecting periaortic fat by performing ORO lipophilic staining on excised murine aortae (**Figure 4.3F**). Our results support the application of PAT as a noninvasive *in vivo* method for preclinical studies of lipid-based conditions.

We then demonstrated the utility of this technique by detecting differences in periaortic lipid accumulation among groups of mice with different genetic background, age, and gender. Our results showed that adult male apoE$^{-/-}$ mice had significantly greater periaortic fat accumulation compared to adolescent males, female apoE$^{-/-}$, and WT mice ($p<0.01$). These results are consistent with the literature, which shows that male apoE$^{-/-}$ mice are more prone to develop cardiovascular disease compared to female apoE$^{-/-}$ mice, as they are used for aneurysm, deep vein thrombosis, and atherosclerosis studies.[166; 190-193] In fact, male apoE$^{-/-}$ mice are more prone to developing atherosclerotic lesions especially when fed a high fat diet.[190] We also investigated if female apoE$^{-/-}$ mice fed a high fat diet would accumulate more periaortic fat compared to female mice fed a normal chow diet. In a study with separate animals, we found that there were no differences in periaortic fat thickness between mice that were placed on a high fat diet for 3 months versus normal chow (data not shown), suggesting that diet may affect luminal and periaortic fat buildup differently. While further studies are needed to explore the various mechanisms affecting luminal and periaortic fat deposition, PAT can be a powerful tool for providing noninvasive information about lipid accumulation.

While PAT has the potential to improve preclinical and clinical imaging, there still remains room to optimize this technique to improve depth of penetration and minimize photoacoustic artifacts. One limitation of our current PAT technique is that much of the 1210 nm light is absorbed by subcutaneous fat and reflected off of the skin, therefore decreasing the depth of penetration. Light attenuation by skin, muscle, and blood also limit penetration of photons to the posterior periaortic fat. As a result, we were unable to quantify lipid accumulation on the posterior aortic wall. Moreover, our current PAT setup is susceptible to artifacts that match the geometry of the skin layer and sometimes appear within a region of interest. This artifact

typically appears at two times the vertical distance from the probe-skin boundary and we hypothesize that it appears due to light reflecting off of the skin surface and causing a photoacoustic effect at the probe interface. This is clearly seen in the WT images as a thick skin geometry-matching PAT signal at depths of 5 to 8 mm (**Figure 4.2**). Imaging atherosclerotic plaques in rodents with our current PAT system is also challenging and requires further optimization for *in vivo* characterization of murine atherosclerosis. Therefore, future work will be focused on improving our system by increasing the light fluence through the skin and to employing mechanisms to minimize light reflection towards the PAT probe.

4.6 Conclusion

The work described here illustrates the unexplored application of PAT for preclinical *in vivo* lipid detection. While further optimization is possible, PAT has a clear advantage for rapid, noninvasive, and label-free imaging. Moreover, PAT is easily coupled with ultrasound imaging, providing both anatomical and compositional information of tissue with better depth of penetration compared to conventional optical techniques. Development of this technology has the strong potential to lead to a myriad of applications, such as studying lipid-based disease pathology, evaluating therapeutics, and aiding in the diagnosis of human disease.

4.7 Acknowledgements

The authors would like to thank Dr. Ji-Xin Cheng for use of the Nd:YAG OPO laser and Hannah M. Ginsberg for her assistance during animal imaging. Both Gurneet S. Sangha and Evan H. Phillips made equal contribution in the preparation of this manuscript. Funding was provided by the American Heart Association through the Scientist Development Grant (14SDG18220010) and a Jim and Diann Robbers Research Grant from the Purdue Center of Cancer Research to CJG.

5. OPTIMIZATION OF PHOTOACOUSTIC IMAGE QUALITY

A current limitation in small animal high-resolution photoacoustic imaging is absorption of light by subcutaneous absorbers. Here, we characterize fiber bundle orientations and illumination geometries to optimize light delivery into tissue to improve signal to noise ratio and penetration depth. This chapter contains published content from the Photoacoustic journal entitled, "Adjustable Photoacoustic Tomography Probe Improves Light Delivery and Image Quality." The published version of this chapter is available through the following link: https://doi.org/10.1016/j.pacs.2018.08.002

5.1 Abstract

One cause for suboptimal photoacoustic tomography (PAT) penetration depth is attenuation of incident light by soft tissue. To better understand this problem, we investigated the effects of illumination fiber optic bundle geometry on PAT penetration depth and signal-to-noise ratio. An adjustable, motorized PAT probe was used to reduce probe-skin reflection artifacts and improve light distribution in the image acquisition plane by tuning fiber orientation. We validated our motorized PAT probe through Monte Carlo simulations and *ex vivo* imaging of a tissue mimicking phantom, and *in vivo* imaging of murine periaortic fat. Overall, our *ex vivo* results showed a several millimeter improvement in penetration depth and *in vivo* results showed a >62% increase in lipid signal-to-noise ratio. Our PAT probe also utilized a 7-μm aluminum filter to block *in vivo* probe-skin reflection artifacts. Together, these findings showed the importance of optimizing illumination geometry to enhance PAT image quality.

5.2 Introduction

Photoacoustic Tomography (PAT) has been shown to provide real-time compositional information of tissue without the need for exogenous contrast agents and with superior penetration depth compared to conventional optical techniques.[137; 194; 195] These optical barriers are overcome since PAT does not rely on conventional ballistic photons, but rather detects acoustic waves that are thermoelastically produced by photon-tissue interactions.[137; 194; 195] Therefore, PAT can provided useful compositional information that complements current clinical

imaging modalities, thus emphasizing the capability of this imaging approach to improve medical care. These characteristics highlight the potential of the technology to be used for a variety of biomedical applications including atherosclerosis,[100-102; 196-198] cancer,[199-201] and nerve imaging.[186]

While PAT has shown great potential, there are still certain biological barriers that have limited its use. For example, applications for high-resolution noninvasive lipid-based imaging are limited to roughly 3 mm due to subcutaneous fat absorbers, as well as the intrinsic light attenuation due to optical properties of tissue.[1; 196] Therefore, there is still a need for further PAT optimization to fully utilize its capabilities. Previous works have utilized image processing and instrumentation engineering to improve image quality and eliminate PAT-specific artifacts. Light catching mechanisms have been particularly useful for redirecting reflected light back into tissue to increase photon density, thus improving signal intensity.[202-204] While effective, the combination of this approach and manually tuning the angle of the fiber optic bundles to improve photon density at various depths may be a superior technique for improving image quality. This is further supported by previous works that have shown that tissue light distribution is effected by illumination geometry.[205; 206] Therefore, we hypothesized that by manipulating fiber-ultrasound orientation we can optimize light penetration into tissue, thus improving penetration depth and signal-to-noise ratio (SNR). Light tuning is dependent on fundamental photoacoustic principles where an initial photoacoustic pressure rise (p_o) results from light-induced thermoelastic expansion as characterized by **Equation 5.1**.

$$p_o = \Gamma \mu_a F \qquad \textbf{Equation 5.1}$$

Here the pressure rise p_o is dependent upon the Grüneisen parameter (Γ), absorption coefficient (μ_a), and optical fluence (F) if we assume that all of the absorbed light is converted to heat energy.[81; 137] The Grüneisen parameter is further defined by **Equation 5.2**, where α is the isobaric volume thermal expansion coefficient, κ is the isothermal compressibility, ρ is the density of the sample, and C_p is the specific-heat capacity. These parameters, including μ_a, are dependent on the innate tissue properties; therefore we can assume that increasing photon density in the tissue can increase the PAT signal amplitude. Taken together, we aim to design tunable fiber optic PAT probes that can enhance image quality for a wide variety of applications.

$$\Gamma = \alpha / (\kappa \rho C_p)$$ **Equation 5.2**

Digital image processing techniques have played a tremendous role in minimizing in-plane artifacts and out-of-plane clutter,[207; 208] however, in some cases artifact prevention strategies may be a more appropriate solution to improve image quality. PAT reflection artifacts is one such example where light reflects off of the skin surface that causes a photoacoustic (PA) effect at the probe face rather than within the sample.[209] This PA ultrasound wave then travels and reflects off of the skin surface, registering in the ultrasound system as originating at a distance two times the probe to skin spacing (**Figure 5.5A**). Singh et al. has previously developed a simple yet effective PAFUSion technique to remove PAT reflection artifacts without the need of additional transducers or algorithms.[210; 211] This approach uses the ultrasound transducer to acquire two images where one image is focused on the optical absorber and the other is focused on the acoustic reflector induced artifact. A weighted addition is then performed and used to recreate a corrected image without the reflection artifact. While this approach is effective, we explore an alternative solution by which an aluminum filter is used to decouple the optical absorbance by the ultrasound transducer to eliminate the reflection artifact. We quantitatively evaluate the use of a light reflecting material over our PA probe to prevent optical absorption by the transducer and adequately remove this probe-skin interaction artifact.

Here, we propose to use a method whereby the fiber optic bundles are tuned to increase photon density in the image acquisition plane. This method can be coupled with other light manipulation techniques, such as the light catching mechanism, to further improve penetration depth and SNR. We introduce our methods to design and build a PAT holder that allows tuning of the fiber optic bundle orientation. We also investigate the effect of fiber optic bundle orientation on tissue light distribution using Monte Carlo multilayer (MCML) modeling. We then compared these results to *ex vivo* and *in vivo* studies were we used focal length to quantify changes in image quality, as we believe this is a more intuitive experimental metric compared to fiber optic bundle angle. We defined focal length as the distance between the bifurcated fiber optic bundles and where the two incident light beams converge. This should not be confused with the transducer focus, which is defined as the depth with the narrowest acoustic beam width. We also present a straightforward and effective method to remove reflection artifacts that can be used on virtually all PAT imaging systems. Overall, the work described here suggests that PAT

illumination geometry should be optimized for different biological tissues due to varying optical tissue heterogeneity and to minimize in-plane artifacts and out-of-plane clutter.

5.3 Methods

5.3.1 Photoacoustic Tomography System Design

The PAT system utilized in this study consists of a high-frequency small animal ultrasound system (Vevo2100, FUJIFILM Visual Sonics) and an Nd:YAG pulsed optical parametric oscillator (OPO) laser (Surelite EX, Continuum). Ultrasound system was equipped with a 40 MHz center frequency transducer (MS550D) that allowed the user to acquire images with an axial resolution of 40 μm. The Nd:YAG laser was capable of producing 5 ns pulses at 10 Hz ranging from 670-2500 nm. Pulsed light was delivered from the laser to the sample through a 2 meter fiber optic bundle with a opening diameter of 1.0 cm and rectangular terminals of 18 mm x 2 mm. This allowed us to produce an optical fluence of 40 mJ/cm^2, which is below the American National Standards Institute (ANSI) safety standards.[138] A pulse generator (9200, Quantum Composers) synchronized laser excitation with ultrasound and PAT image acquisition by sending 1) appropriately timed 10 Hz, 5 V inverted signals to the laser q-switch and flash lamp and 2) a normal 10 Hz, 5 V pulse signal to the ultrasound system. Finally, to prevent acoustic focus induced changes in SNR the transducer focus was set to 7 mm for *ex vivo* validation imaging and 5 mm for *in vivo* validation imaging.

5.3.2 Photoacoustic Tomography Fiber-Adjusting Apparatus Design

The PAT fiber-tuning apparatus was first designed using Autodesk Inventor Professional Student Edition (**Figure 5.1A-B**) and built using both 3D printed and fabricated 6061-T6 aluminum parts, as well as commercially available hardware (**Figure 5.1C**). The 3D printed parts were printed from Acrylonitrile Butadiene Styrene plastic using a Stratasys Fortus 400mc 3D Production System. The arms that hold fiber cables were made of 16-gauge-carbon steel, while the remaining plates that mount the stepper motors are made from 0.25 inch 6061-T6 aluminum. A 12 V Nema 17 external linear stepper motor (17LS13-0404E-100H, StepperOnline), a 5.4 V Nema 17 bipolar stepper motor (17HM15-0904S, StepperOnline), and a Stepoko 3-axis controller (ROB-13899, SparkFun) were used to adjust the translation of the ultrasound

transducer and rotation of the fiber optic bundles. The external linear stepper motor specifically controlled the ultrasound transducer height by allowing a step angle of 1.8°, thus producing a movement length of 0.02 mm per step. The bipolar stepper motors, equipped with a 16 tooth 32 pitch motor pinion gear, was able to produce a fiber optic bundle step angle of 0.11° to control each fiber optic cable. These specifications were chosen to give us the appropriate strength, accuracy, and precise control of the fiber optic bundles and ultrasound transducer. These stepper motors were controlled by the Stepoko 3-axis controller using GRBL software to allow us to finely tune the ultrasound and fiber optic bundle position. This apparatus was designed to have a 3 cm offset between the transducer face and motors to make sure that the hardware did not interfere with the sample being imaged. Moreover, the translation of the ultrasound transducer allowed us to adjust the pivot point around which the fiber optic bundles rotated, thus allowing us to tune the focal length of our PAT probe.

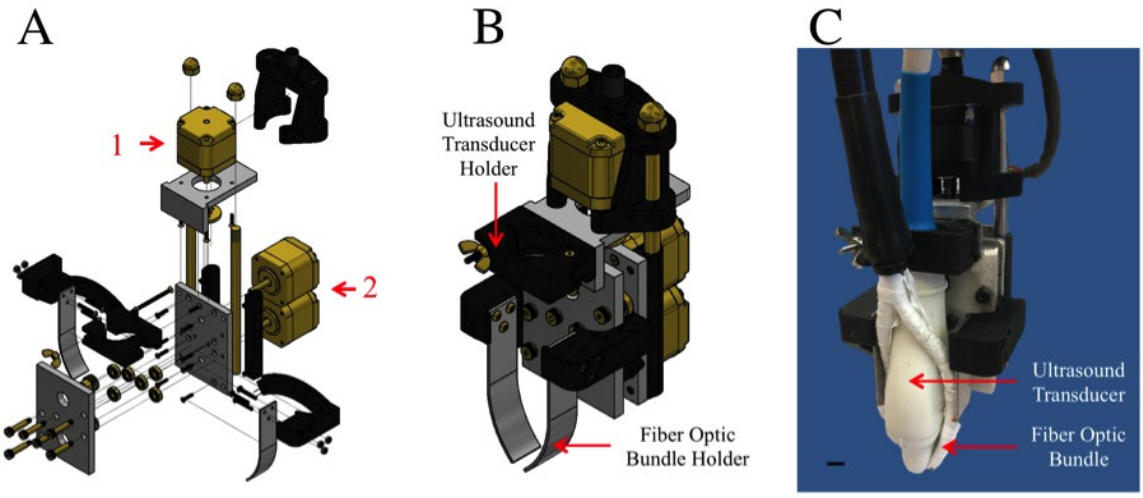

Figure 5.1: Exploded (A), presentation (B), and constructed (C) images of the PAT holder. Fabricated parts shown in silver, 3D printed parts shown in black, and commercially available parts shown in gold. PAT holder specifically consists of motors for translation of ultrasound transducer (1), and rotation of fiber optic bundles (2). Scale bar represents 1 cm.

5.3.3 Monte Carlo Multilayer Simulation Study

MCML simulations were performed to assess near-infrared light interaction with 20% polyvinyl alcohol (PVA) at various fiber optic bundle orientations. PVA was specifically chosen due to its well-characterized tissue mimicking optical properties (**Table 5.1**). Ray tracing software (TracePro, Lambda Research Corporation) was used to design the tissue-mimicking

phantom geometry that was later used for *ex vivo* validation studies. Tissue-light interaction was simulated through two 18 mm x 2 mm fiber optic bundles that delivered 100 randomly arranged rays with a radiant flux of 0.15 W at 1064 nm. These fiber optic bundles were placed 5 mm away from each other to account for the ultrasound transducer width at orientations of 0°, 15°, 30°, 45°, and 60° with respect to the ultrasound transducer. To further improve the accuracy of our simulation the fiber optic bundles were submerged in a water to account for light attenuation due to acoustic-coupling agents with a distance of 3 mm from the PVA. This MCML simulation model and example output is shown in **Figure 5.2A** and **5.2B**, respectively. The relevant optical properties and geometries for the water and PVA are summarized in **Table 5.1**. Briefly, water scattering anisotropy and refractive index were obtained from previous works,[212; 213] while absorption coefficient at 1064 nm was interpolated from literature values.[214] We were unable to find scattering coefficient at 1064 nm; therefore, scattering coefficient for 800 nm light was used,[215] as light attenuation due to scattering is negligible in the infrared region.[216] PVA absorption, scattering, and refractive index values were obtained from the literature.[217; 218] Scattering anisotropy (g) was calculated using reduced scattering (μ_s' [219]) and scattering coefficients (μ_s[218]) as shown in **Equation 5.3**.

$$\mu_s' = \mu_s(1 - g) \qquad \textbf{Equation 5.3}$$

Two MCML simulations were performed to understand the effect of fiber optic bundle orientation on light penetration. The first simulation profiled the depth dependent changes in radiant flux to quantify the light distribution throughout the PVA. The second simulation assessed the radiant flux in the long-axis cross-sectional plane to quantify the energy delivered in the image acquisition plane. Five measurements were taken at 0.04825 mm step sizes below the center of the PAT probe to account for the 0.193 mm elevational resolution of our transducer. Together, these experiments allow us to profile how fiber optic bundle orientation impacts the radiant flux throughout the PVA.

Table 5.1: Summary of optical properties and geometry of the simulated water and PVA. τ denotes calculated value.

	Absorption Coefficient (mm^{-1})	Scattering Coefficient (mm^{-1})	Scattering Anisotropy	Refractive Index	Length x Width x Height (mm)
Water	0.0154 [214]	$3x10^{-7}$ [215]	0.890 [213]	1.32 [212]	78x58x10
Polyvinyl Alcohol	0.035 [218]	6.90 [218]	0.930[τ]	1.47 [217]	78x58x20

5.3.4 *Ex Vivo* Validation Study

A depth-profiling phantom was designed to evaluate the performance of our PAT holder. This phantom consisted of 20% PVA by weight with six polyethylene-50 (PE-50) tubes running through it at depths of 1 mm (**Figure 5.3B**). Phantom mold was designed and optimized in Inventor and then 3D printed (Statasys Fortus 400mc). We used 20% PVA due to its tissue-mimicking acoustic and optical properties,[220] and PE-50 tubes as they produce PA signal when exposed to 1210 nm light. PVA was prepared using a modified method as described by Kharine et al.[220] Briefly, 20% PVA (Sigma Aldrich, St. Louis, MO) was prepared by slowly dissolving PVA crystals in a secondary heat bath for 6 hours. Temperature of solution was cycled between 60° C and 90° C to promote dissolving of PVA crystals. Once dissolved, the 20% PVA solution was centrifuged to remove air bubbles. PVA was then poured into a mold with PE-50 tubes (Braintree Scientific Inc., Braintree, MA) and undergone seven freeze thaw cycles.[220] We defined one freeze thaw cycle as placing the mold in a -20° C refrigerator for 12 hours, followed by thawing the mold at room temperature for 12 hours. Once prepared, we imaged our phantom using combined ultrasound and PAT imaging at three different locations. Short-axis B-Mode imaging was first used to identify all six PE-50 tubes, followed by PAT images using 1210 nm light to obtain PE-50 specific contrast. PAT holder was used to acquire ultrasound and PAT images with focal length of 2, 3, 5, and 7 mm. SNR was then calculated using FIJI, where the 16-pixel region of interest was chosen to measure the average PAT signal (A_{Signal}) and background noise (A_{Noise}) for all PE-50 tubes (**Equation 5.4**). We chose to use 16-pixel region of interest as this allowed us to maximize the measurement area without the incorporation of background noise.

$$\text{SNR} = A_{signal} \,/\, A_{noise} \qquad \textbf{Equation 5.4}$$

5.3.5 *In Vivo* Validation Study

We performed ultrasound and PAT imaging on the infrarenal aorta of apolipoprotein E-deficient (apoE$^{-/-}$) mice (n=3) to assess the performance of our PAT holder *in vivo*. Six week old apoE$^{-/-}$ male mice were obtained from Jackson Laboratory (Bar Harbor, ME), fed a standard chow diet, and weighed 24.7 ± 4.9 grams at the time of imaging. A small animal anesthesia system (SomnoSuite, Kent Scientific) was used to anesthetize the animals using 2-3% isoflurane and 225 mL/min room air.[189] Eye lubricate was applied to the eyes of the mouse to prevent corneal desiccation. Animal vital signs were closely monitored to ensure a consistent anesthetic plane. Mice were placed on a heated stage to maintain body temperature at approximately 34-36^{o} C, which was monitored via rectal probe. Heart rate and respiration were monitored using electrodes built into heated stage and maintained at 500-600 beats/min and 40-80 breaths/min, respectively. Infrarenal aortas was found via long-axis B-mode ultrasound imaging and imaging location was kept consistent between animals by identifying the left renal vein and tail artery bifurcation. The aorta was then imaged using 1210 nm light to target lipids and 1400 nm as an off-resonance control. Similar to our *ex vivo* studies, we then tuned the focal length of our PAT probe to 2, 3, 5, and 7 mm to assess the effect of illumination geometry on image quality. Images were analyzed in FIJI to calculate SNRs using a region of interest of 16 pixels due to small-scale thickness of the periaortic fat.

5.3.6 Photoaccoustic Reflection Artifact Removal

The engineering design specification for materials that have the potential to reduce the PAT reflection artifact include 1) complete reflection of light, 2) minimal attenuation of ultrasound and PAT signal, and 3) an inability to generate a PAT signal. These design criteria were chosen to prevent optical absorption by the ultrasound probe to eliminate reflection artifacts, while allowing easy registration of ultrasound and PAT signals. We chose to experiment with aluminum filter with thickness of 4, 7, and 16 μm as aluminum is cost effective and its material properties allow reflection of light with no generation of PAT signal. We first tested the aluminum filter's ability to prevent light transmission by delivering pulsed laser light to the aluminum filter, with a power meter on the opposite side of a laser to measure light transmission. This was done to validate that the thin aluminum sheets did not have any major defects that

would prevent complete blockage of light. We then tested the aluminum filter's ability to remove PAT reflection artifact *in vivo* by obtaining PAT images of periaortic fat on the infrarenal aorta of apoE$^{-/-}$ mice. The same animal care and imaging protocol was used as the *in vivo* PAT holder validation studies above. Both sides of the aluminum foil sheet were coated with ultrasound gel to act as an acoustic coupling agent between both 1) the transducer and the foil and 2) the foil and the mouse. The aluminum foil was mounted on the transducer face prior to fixing the ultrasound probe to the PAT fiber-tuning apparatus, thus allowing both artifact elimination and light delivery through the fiber optic bundles. The transducer was placed on the abdomen of the animal to obtain long-axis ultrasound and PAT images of the infrarenal aorta between the left renal vein and tail artery bifurcation. We then imaged the mouse with and without the aluminum filter to assess the ability to remove reflection artifact. Images were exported to FIJI and SNR was calculated using region of interest of 16 pixels along the periaortic fat to quantify filter induced signal attenuation.

5.3.7 Statistical Analysis

All MCML radiant flux and *ex vivo* and *in vivo* SNR ratio measurements are reported as mean ± standard deviation. Additionally, an ANOVA with a Tukey post-hoc statistical test was used to determine significance between experimental groups ($p<0.05$).

5.4 Results

5.4.1 Monte Carlo Simulation Results

MCML simulations were performed to assess depth-dependent and long-axis cross-sectional changes in radiant flux with varying fiber optic bundle orientations. Our depth-dependent simulation showed an exponential decrease in radiant flux from 0.45 ± 0.01 W at the surface of the PVA to 0.05 ± 0.01 W at 10 mm into the PVA (**Figure 5.2C**). We also observed that fiber optic bundles orientation of 0º, 15º, and 30º have greater radiant flux compared to angles of 45º and 60º up to depths of 6 mm. In fact, the average power amongst 0º, 15º, and 30º orientation at 5 mm produced a 21% increase in radiant flux compared to the average between 45º and 60º. While our simulations showed that fiber optic bundle angles play a role in increasing optical fluence in our sample, we also wanted to assess the impact of fiber optic

bundle orientation on light delivery in our image acquisition plane (**Figure 5.2D**). To do this we designed a simulation to measure radiant flux in five locations along the image acquisition plane. We observed a Gaussian distribution with the greatest radiant flux at 30° (0.28 ± 0.06 W), and the lowest flux at 0° (0.12 ± 0.02 W) and 60° (0.08 ± 0.01 W).

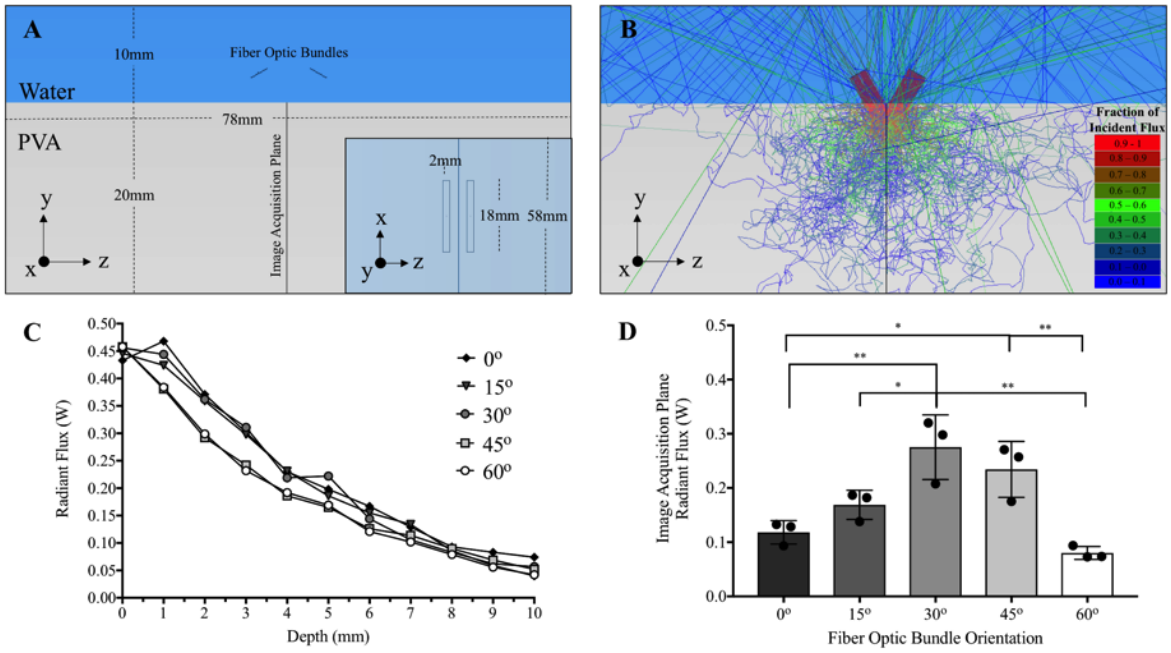

Figure 5.2: MCML Simulation Results: MCML geometry (A) was created with two 18mm x 2mm fiber bundle terminals that produced 100 random rays at 1064 nm with power of 0.15 W to model light interaction through 3 mm of water bath and 20 mm of PVA (B). Depth-dependent simulation showed exponential decrease in radiant flux with higher fluence at orientations of 0°, 15°, and 30° compared to 45° and 60° (C). Image acquisition plane measurements at five locations showed greatest radiant flux at 30° and the lowest radiant flux at 0° and 60° (D). Statistical significance is shown at $p < 0.05$ (α) and $p < 0.01$ (#, Λ, λ, β, ε, X). Inset A: Top view of the MCML 20% PVA simulation geometry.

5.4.2 *Ex vivo* Validation Results

Figure 5.3 summarizes the results for the *ex vivo* validation experiments. Using short-axis B-mode ultrasound imaging we were able to resolve all six PE-50 tubes in our PVA phantom. Our PAT results, however, showed the SNR and penetration depths were dependent on the focal length of our probe. Qualitative assessment shows that as we increase the focal length of our PAT probe from 2 mm to 7 mm we can resolve deeper PE-50 tubes that result in a penetration depth improvement of 2 mm (**Figure 5.3A**). This improvement in image quality is supported by our quantitative SNR results (**Figure 5.3C**), which show a focal length of 2 mm resolves the PE-50 tubes up to 3.00 mm depth with SNR above 4.7, but resolves the PE-50 tubes

at depths of 3.75 mm and 4.50 mm with a sharp drop-off in SNR of 3.2 ± 0.26 and 2.0 ± 0.53, and no contrast for the PE-50 tube at depth 6.00 mm. As we increase the focal length to 7 mm we see that we can resolve contrast for the PE-50 tubes with depths of 3.75 mm, 4.50 mm, and 6.00 mm with SNR of 3.71 ± 0.30, 2.71 ± 0.42, and 2.12 ± 0.32, respectively. This increase in penetration depth, however, comes at a cost as shown by the decrease in SNR ratio at depths of 1.5 mm (4.37 ± 0.16 to 3.73 ± 0.25), 2.5 mm (4.74 ± 0.31 to 4.34 ± 0.40), and 3.00 mm (4.74 ± 0.28 to 4.26 ± 0.23).

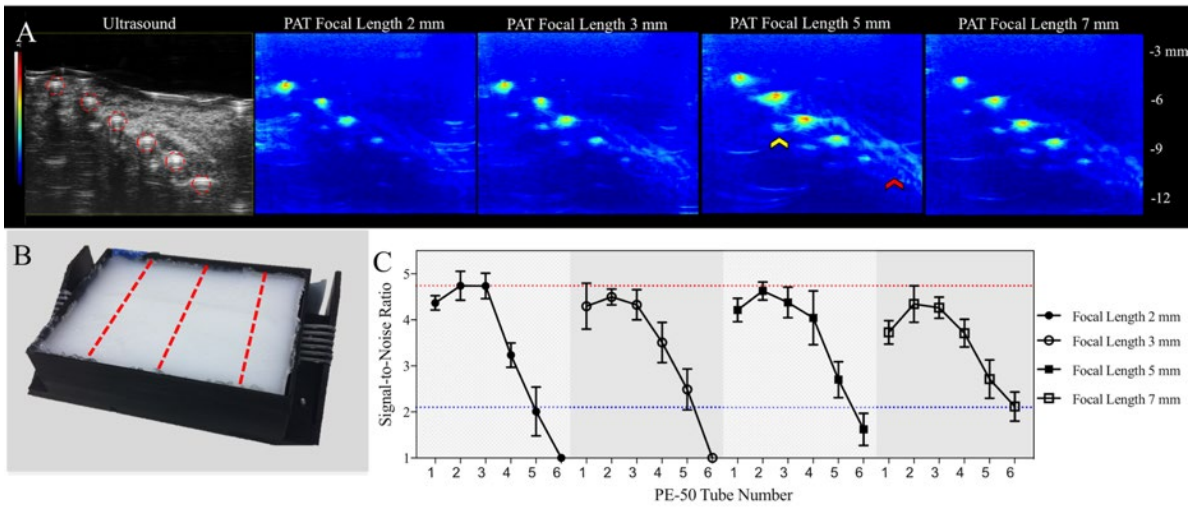

Figure 5.3: *Ex vivo* Validation Results: Seven freeze-thawed cycled 20% PVA phantom embedded with six PE-50 tubes was imaged using ultrasound and PAT with focal lengths of 2 mm, 3 mm, 5 mm, and 7 mm (A). Three imaging locations were selected from the depth-profiling phantom to ensure measurement consistency (B). PE-50 tubes are highlighted with purple dotted circles in the ultrasound image. Quantitative results show that we observe better SNR for superficial PE-50 tubes using focal length of 2 mm and 3 mm, and improved contrast for deeper PE-50 tubes using focal length of 5 mm and 7 mm (C). Red dotted line signifies greatest SNR for superficial tubes and blue line signifies greatest SNR for the deeper tubes. Yellow and red arrows signify reflection and motor induced artifacts, respectively.

5.4.3 *In vivo* Validation Results

Figure 5.4 summarizes the qualitative and quantitative in vivo assessment of our PAT holder using focal lengths of 2, 3, 5, and 7 mm. Qualitative assessment shows focal length dependent increased signal intensity from subcutaneous and periaortic fat when imaging apoE-/- mice using 1210 nm light (**Figure 5.4A**). This was supported by our quantitative assessment, which shows steady increase of subcutaneous and perivascular fat SNR when focal length is tuned from 7 mm to 2 mm. Specifically, we found subcutaneous fat SNR of 4.7 ± 1.1 at 2 mm focal length, 4.0 ± 0.41 at 3 mm focal length, 3.6 ± 0.29 at 5 mm focal length, and 2.9 ± 0.36 at 7

mm focal length (**Figure 5.4B**). Additionally, we observed a periaortic fat SNR of 2.3 ± 0.37 at 2 mm focal length, 2.1 ± 0.25 at 3 mm focal length, 1.9 ± 0.59 at 5 mm focal length, and 1.3 ± 0.13 at 7 mm focal length (**Figure 5.4C**). Our results also showed a statistically significant increase ($p<0.05$) in both subcutaneous and periaortic SNR between focal lengths of 2 and 7 mm. Overall, we observed a 77% increase in subcutaneous SNR and 62% increase in periaortic SNR.

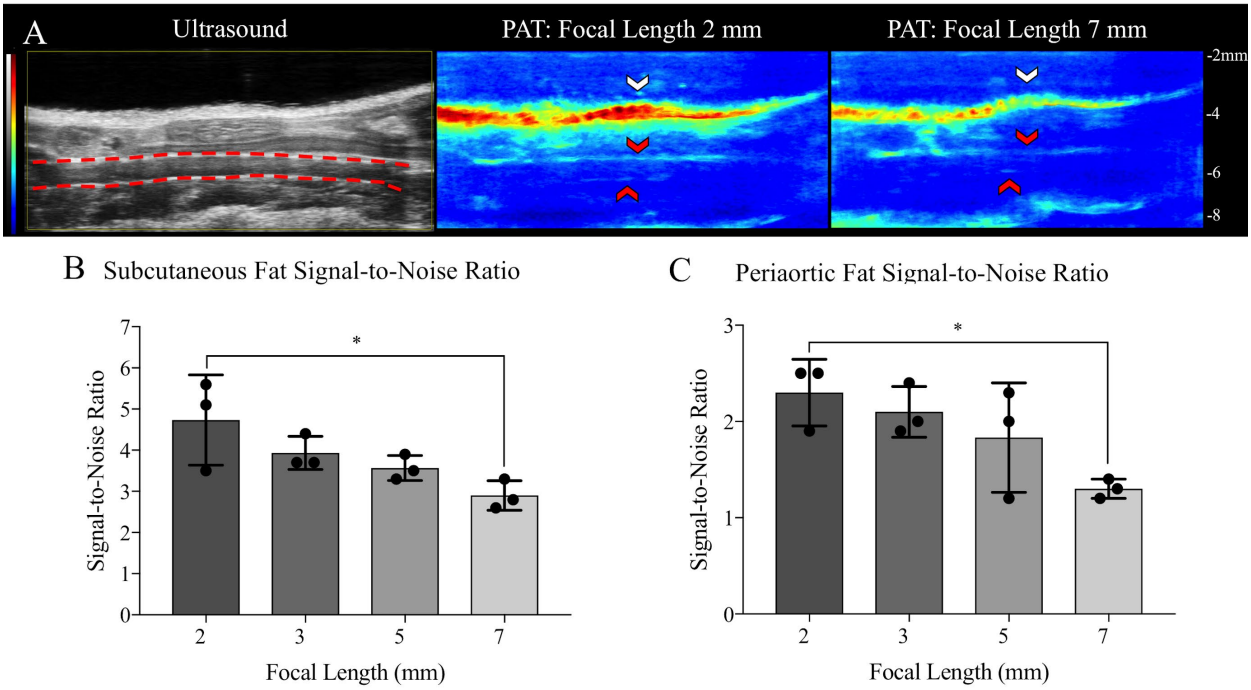

Figure 5.4: *In vivo* Validation Results: Subcutaneous fat and infrarenal periaortic fat were imaged in apoE$^{-/-}$ mice to show increased PAT signal intensity when tuning focal length from 7 mm to 2 mm (A). We observed an increased SNR in the subcutaneous fat (yellow arrow) and periaortic fat (red arrow). The infrarenal aorta is outlined in red dotted line. Quantitative assessment shows statistically significant ($p < 0.05$) increase in subcutaneous SNR of 77% (B), and statistically significant ($p<0.05$) increase in periaortic SNR of 62% (C). Statistical is significance shown at $p < 0.05$ (*).

5.4.4 Photoacoustic Reflection Artifact Removal Results

We quantitatively assessed both the ability of aluminum filters to completely reflect incoming light and also prevent PAT reflection artifacts. Through our light transmission experiment we found that 4, 7, and 16 µm aluminum filters were all able to completely block light transmission, thus showing potential to prevent PAT-related reflection artifacts through decoupling of light-probe interactions. Moreover, when we applied our aluminum filter to our PAT probe and performed *in vivo* imaging of periaortic fat on the infrarenal aorta we found that the 4 and 7 µm aluminum filters prevented the PAT reflection artifact (**Figure 5.5B**). The 16 µm

aluminum filter, however, did not allow acquisition of both ultrasound and PAT images, potentially because the aluminum was too thick to allow penetration of acoustic waves. Quantitative analysis showed that baseline average periaortic SNR to be 2.37 ± 0.16, while the average periaortic SNR slightly decreased to 2.03 ± 0.34 with the 4 μm aluminum filter and 2.03 ± 0.38 with the 7 μm aluminum filter (**Figure 5C**).

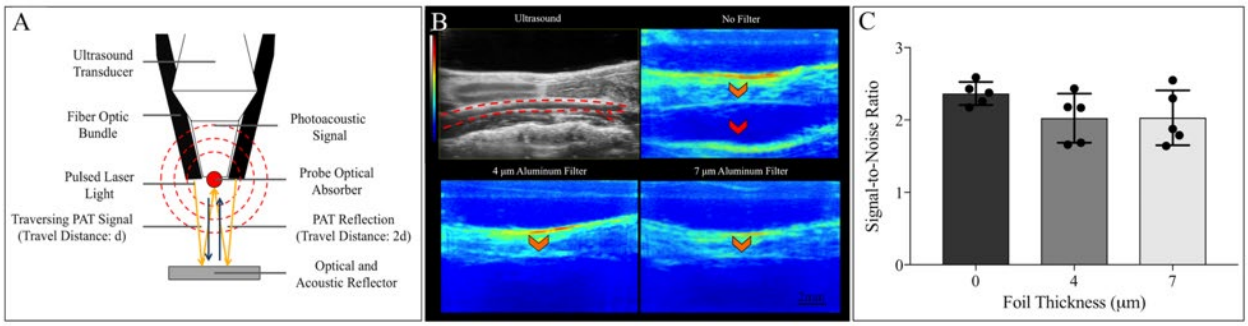

Figure 5.5: Schematic of reflection artifact (A) showing how light reflects off of the optical reflector and induces a photoacoustic effect at the PAT probe face. This PAT signal then travels distance *d* down towards the acoustic reflector and travels another distance *d* up towards the ultrasound transducer. The PAT system, therefore, registers the acoustic wave as traveled 2*d*, creating an artifact that can obscure image quality. The reflection artifact is effectively eliminated when a light-blocking aluminum filter is applied to the transducer face (B) as shown by the ultrasound (top left), PAT without filter (top right), and PAT with 4 μm (bottom left) and 7 μm (bottom right) filter images. Quantitative SNR assessment shows slight decrease in SNR when utilizing aluminum filters (C). The infrarenal aorta is highlighted by the red dotted lines, the periaortic signal by the orange arrows, and the reflection artifact by the red arrow.

5.5 Discussion

We have developed an adjustable, motorized PAT holder that improves optical fluence at various layers of tissue to increase penetration depth and SNR. This holder consisted of an external linear stepper motor that allows vertical translation of the ultrasound transducer to adjust the pivot point around which the fiber optic bundles rotate, and two bipolar stepper motors that allow the user to tune the fiber optic bundle angle with respect to the ultrasound transducer. These stepper motors were controlled by a Stepoko 3-axis controller that used GRBL software, allowing for 0.02 mm translation of the ultrasound transducer and 0.11° rotation of the fiber optic bundles. Our rationale for pursuing this light manipulation mechanism is that illumination geometry can impact photon density within the tissue, which will then affect PAT signal generation. By tuning our fiber optic bundle orientation, we can optimize light fluence in our image acquisition plane and improve our PAT penetration depth and SNR.

The MCML simulations revealed that the largest spot size at 30° allowed maximum light penetration and flux in the image acquisition plane, while orientations at 0° and 60° resulted in suboptimal tissue light fluence due to the momentum of the incident light being directed laterally and parallel to the image acquisition plane. These results, however, will vary depending on the ultrasound transducer and fiber optic bundle geometry, as well as distance between PAT probe and tissue surface. For example, in our simulation 30° produced the largest spot size due to the PAT probe offset of 3 mm from the surface of the PVA. If this offset is increase or decreased the fiber optic bundle angle of 30° would not create the largest spot size, producing suboptimal radiant flux. Collectively, these results show that there is an optimal fiber optic bundle configuration that allows maximum fluence throughout the sample of interest, as well as in the image acquisition plane. These configurations, however, will vary depending on the overall PAT imaging geometry.

The *ex vivo* PAT imaging of PVA embedded with six PE-50 tubes matched well with the MCML simulations. Further the *ex vivo* images confirmed that tuning fiber angle can alter the SNR at various depths and can lead to improvement in penetration depths. A focal length of 5 mm produced the smallest theoretical spot size and allowed us to resolve the first five PE-50 tubes. When we increased our focal length to 7 mm we also increased our spot size that led to a 2 mm improvement in penetration depth, but with a cost to decreased SNR for more superficial PE-50 tubes. Focal lengths of 2 and 3 mm, however, produced incident light momentum that caused light to move laterally from the image acquisition plane, thus decreasing penetration depth. It is important to note that the improvements in penetration depth and SNR can vary depending on the optical properties of the tissue and the transducer frequency. In this case, our phantom broadly mimicked the acoustic and optical properties of breast tissue.[220; 221] Imaging depth is also dependent on application, where breast tumor margin imaging is focused on 2 mm suggesting a 2 mm improvement can be suitable for shallow imaging.[199] Taken together, our *ex vivo* validation shows that the focal length of the PAT probe can be tuned to improve the radiant flux in the image acquisition plane to improve penetration depth and SNR.

The *in vivo* murine images revealed the importance of utilizing a focal length tuning apparatus to obtain improved image quality of subcutaneous and periaortic fat accumulation in apoE$^{-/-}$ mice. We observed a 77% increase in subcutaneous fat SNR and a 62% increase in periaortic fat SNR by decreasing the focal length from 7 mm to 2 mm. Additionally, by tuning

the focal length we resolved periaortic fat accumulation on both and anterior and posterior wall of the aorta, a critical improvement that opens up the possibility of characterizing plaques in small animal models.[196] We did observe, however, that while the ultrasound probe is placed 3 mm from the skin surface, the probe with focal length of 2 mm produced the greatest SNR. We attribute this to the heterogeneity in the absorption and scattering of the tissues that are being imaged (e.g. skin, muscle, intestines) that may cause complex scattering regimes that are not simulated in our homogenous MCML simulation. Another consideration is that the focal length was measured in air and not in water, thus the focal length in water may vary due to slight scattering effects. Nevertheless, the results of our MCML and *ex vivo* studies suggest that there is little deviation in focal length when light travels through water. These *in vivo* results, therefore, emphasize the need for PAT holder that can allow the user to optimize their tissue illumination to improve image quality. This highlights the preclinical and clinical utility of an adjustable PAT probe, as the illumination geometry should be carefully considered depending on the tissues being imaged.

Finally, we present an alternative and effective method to remove PAT reflection artifacts that arise due to light interaction with the ultrasound probe face through the use of 4 μm and 7 μm thick aluminum foil. This reflection artifact arises due to light reflecting off of the tissue surface and interacting with the PAT probe face to induce a PA signal. This signal is then reflected off of the skin surface and registered by the ultrasound system, thus producing an artifact that matches the geometry of the tissue surface but at twice the skin depth. One caveat for utilizing the 4 μm aluminum foil, however, is that it is very fragile and easily torn when applied with shear forces. Still, these experimental results show that 4 and 7 μm filters are thick enough to completely reflect light, yet thin enough to allow penetration of acoustic waves. This allowed us to reflect light away from the probe face while also acquiring both PAT and ultrasound signal, thus making aluminum an effective filter to prevent probe-specific reflection artifacts. It is important to differentiate when to use artifact prevention strategies (i.e. foil filter) and post-image processing techniques to remove in-plane artifacts and out-of-plane clutter. In-plane artifacts typically result from high PAT signals that reflect off of acoustically dense structures capable of obscuring regions of interest. On the other hand, photoacoustic transients that originate outside of the image acquisition plane can cause out-of-plane clutter that leads to misinterpretation of PAT images. Examples of reflection and motor-induced interference can be

seen in **Figure 5.3B**, with artifact signal increasing up to a focal length of 5 mm, suggesting that illumination geometry may independently affect both PAT signal and artifact intensity. Therefore, it is important to emphasize that an aluminum filter may be effective in removing artifacts due to optical absorption at the probe face, but other sophisticated methods should be used for more troublesome in- and out-of-plane artifacts. Moreover, artifacts due to optical absorption by the ultrasound transducer may be avoided by utilizing a probe with a white surface rather than gray acoustic lenses, as found in many commercially available systems.

There are several specific design criteria that can significantly alter the effectiveness of this PAT probe. First, it is critical to minimize the material between the fiber optic bundle and ultrasound transducer face, such as the metal casing that typically house the terminal end of the fiber bundle. This is because if there is too much material between the ultrasound transducer and fiber optic bundle face, the users ability to control where the light is focused within the tissue is reduced. Second, the current dimensions of our motorized PAT probe are 6.5 x 6 x 19 cm, meaning that design optimization is required to miniaturize this fiber tuning mechanism for clinical use. Our probe is specifically limited due to large size of the motors that control translation of the ultrasound transducer and rotation the fiber optic bundles. As the size of transducers vary, the pivot point in which the fibers must rotate can also vary between transducers. One potential solution is to create an optimal ultrasound transducer that requires only one pivot point to achieve a range of desired focal lengths. Finally, special consideration should be made when determining the length of the fiber optic bundle bifurcation. A bifurcation that is too short will limit the attainable focal lengths, as there is not enough cord length to allow for the proper rotation of the fiber bundles. Alternatively, a bifurcation that is too long could make the probe hard to manage, especially for *in vivo* clinical applications. Sub-optimal bifurcation length can increase the chances of damage to the fiber optic bundle due to increased stress applied when the fiber is pushed passed its bending radius. These design criteria specifically apply to PAT probes that utilize bifurcated fiber optic bundles, as well as laser diodes, and light-emitted diodes. While this adjustable holder is certainly versatile, other photoacoustic microscopy techniques and configurations (e.g. diffuser light source, scanning lens, and catheter probes) will require different design criteria based on application and need.[222]

5.6 Conclusion

In conclusion, we have shown through MCML, *ex vivo,* and *in vivo* studies that penetration depth and SNR can be improved by adjusting the fiber optic bundle orientation with respect to the ultrasound transducer. This mechanism improves image quality by increasing photon density in the image acquisition plane. Our results also suggest that illumination geometry should be optimized depending on the optical heterogeneity of the tissue, as well as to maximize SNR and minimize artifacts. With the combination of other light manipulation techniques, such as a light catching mechanism, an advanced PAT probe can be created for high-resolution deep tissue compositional imaging. Further optimization of a tunable handheld PAT probe has the potential to improve image quality for various pre-clinical and clinical applications.

5.7 Acknowledgment

Funding was provided to Dr. Craig J. Goergen through the American Heart Association Scientist Development Grant (14SDG18220010) and a Jim and Diann Robbers Research Grant. Research support was provided to Gurneet S. Sangha through the National Institute of Health T32 Bioengineering Interdisciplinary Training for Diabetes Research (T32DK101001-05) and the National Science Foundation Graduate Research Fellowship Program (DGE-1333468).

6. PHOTOACOUSTIC TOMOGRAPHY FOR MURINE ATHEROSCLEROSIS

The final chapter in this dissertation will highlight the preclinical potential of dual-modality PAT and ultrasound for atherosclerosis imaging. The previous chapter highlights that illumination geometry can improve image quality, but more sophisticated methods must be employed to increase the penetration depth for noninvasive lipid imaging. Additionally, quantification of noninvasively acquired lipid images is limited without the development of calibration methods to take into account the optical properties of more superficial tissues. The advantage of an *in situ* imaging, however, is the tissue of interest can be optimally illuminated to characterize lipid lesion formation. Therefore, this chapter first utilizes *ex vivo* methods to validate the capability of PAT to quantify lipid burden. We then perform a cross-sectional *in situ* PAT and longitudinal *in vivo* ultrasound imaging in a small animal model of atherosclerosis to correlate how changes in arterial hemodynamics and biomechanics impact lipid deposition and vessel morphology. The contents of this chapter are currently under preparation for publication. Feedback from the committee members will be used to modify the manuscript prior to publication submission to APL bioengineering.

6.1 Abstract

Dual-modality photoacoustic tomography (PAT) and 4D ultrasound (4DUS) imaging shows promise for various cardiovascular disease applications, but their use in murine atherosclerosis imaging has not been fully explored. This study used PAT and 4DUS to correlate altered arterial strain and hemodynamics to morphological changes and lipid localization in mice that have undergone partial carotid ligation (PCL) to induce atherosclerosis. We first performed validation experiments to show that PAT signal-to-noise ratio positively correlated with plaque lipid composition obtained from oil-red O histological sections. Cross-sectional *in situ* PAT and longitudinal *in vivo* ultrasound imaging was then performed using a 40 MHz transducer (VisualSonics) and a Nd:YAG pulsed laser (Surelite EX, Continuum). We performed ultrasound imaging on days 0, 1, 4, 7, 10, and 14 for hemodynamic and strain characterization, and 1100 nm and 1210 nm PAT was implemented at the study endpoint for blood and lipid characterization.

These study groups were then separated into day 4 post-PCL with (n=5) and without (n=6) Western diet feeding, as well as days 7 (n=8), 10 (n=8), and 14 (n=8) post-PCL, in addition to a sham control group on a Western diet (n=5). Overall, our data reveals heterogeneous strain throughout the carotid artery and a substantial decrease in LCA pulsatility by day 7. The hemodynamic results suggest greater disturbed flows in the proximal regions resulting in earlier vessel stenosis and greater lipid deposition than distal regions. Morphological and compositional data revealed heterogeneous vascular remodeling between days 0 and 7, with a rapid decrease in vessel volume/length and presence of both intraplaque hematoma and lipid deposition at day 10 post-PCL. Taken together, these results highlight the utility of utilizing dual-modality PAT and 4DUS to characterize and study atherosclerosis progression noninvasively.

6.2 Introduction

Development of dual-modality photoacoustic tomography (PAT) and ultrasound imaging is an emerging area of biomedical research, as these complementary modalities allow for advanced visual and quantitative interpretation for a plethora of multifaceted diseases. Ultrasound uses high-frequency sound waves to measure the acoustic impedance between tissue boundaries, allowing the user to obtain a variety of information regarding tissue morphology and hemodynamics. Conversely, PAT utilizes nanosecond pulsed laser light to thermoelastically induce acoustic waves in order to obtain spatially relevant compositional images (i.e. localization of blood and lipid[196]). The unique characteristics of these imaging techniques have the potential to improve our understanding of the world's most life-threatening diseases.

Cardiovascular disease in particular remains one of the leading causes of death globally with atherosclerosis resulting in a variety of complications ranging from impaired lower-limb mobility to ischemic myocardial infarction and strokes.[223] Current cardiovascular applications of dual-modality PAT and ultrasound are primarily focuses on diagnosis of atherosclerosis,[100; 224-229] identification of thrombus,[230; 231] or ablation of cardiac arrhythmias.[232-234] Developmental efforts in intravascular photoacoustic imaging have especially shown potential to quantify plaque burden in the hopes to identify rupture-prone vulnerable plaques versus benign stable plaques.[105; 235; 236] Moreover, recent advances in 4D ultrasound (4DUS) imaging have opened opportunities to improve kinematic characterization of cardiac[237] and vascular[238] tissues. Dynamic volumetric information provided by 4DUS can be used to estimate 3D Green-Lagrange strain using a direct deformation estimation (DDE) method.[239] One under investigated area of research, however, is consideration of how these novel techniques can be used to better understand atherosclerosis progression.

In this paper, we demonstrated the capability of using dual-modality PAT and ultrasound to characterize atherosclerosis progression in a small animal model. We first performed *ex vivo* validation studies using PAT to quantify lipid-burden in murine atherosclerotic plaques. We then performed a longitudinal *in vivo* ultrasound and cross-sectional *in situ* PAT studies to investigate the interplay between hemodynamics and vessel mechanics on atherosclerosis progression. Standard ultrasound was used to quantify changes in hemodynamics, 4DUS to quantify altered vessel kinematic, and PAT to assess blood and lipid localization throughout the carotid artery. Overall, we evaluated the hypothesis that vascular regions of disturbed flow and decreased vessel

pulsatility are more susceptible to lipid deposition during plaque formation in a murine model of atherosclerosis.

6.3 Methods

6.3.1 Photoacoustic Tomography System Specifications

Our dual-modality PAT and ultrasound system consisted of a Nd:YAG pulsed optical parametric oscillator (OPO) laser (Surelite EX, Continuum) coupled with a high-frequency small animal ultrasound system (Vevo2100, FUJIFILM VisualSonics). The Nd:YAG laser produced 5 ns pulses at 10 Hz ranging from 670-2500 nm that was delivered to the tissue of interest using a bifurcated fiber optic bundle. Our 2 meter fiber optic bundle contained an opening diameter of 1.0 cm and rectangular terminals of 18 mm x 2 mm, producing an optical fluence of 40 mJ/cm^2. The resulting acoustic waves were captured using a 40 MHz (MS550D) center frequency transducer that consisted of 256 piezoelectric element arrays. The laser and ultrasound were coupled using a pulse generator (9200, Quantum Composers) that sent appropriately timed 10 Hz, 5 V inverted signals to both the q-switch and flash lamp, as well as a normal 10 Hz, 5 V pulse signal to the ultrasound system.

6.3.2 Photoacoustic Tomography Resolution Characterization

A depth-profiling phantom was fabricated to characterize the resolution of our PAT system. This phantom consisted of tissue-mimicking 20% polyvinyl alcohol (PVA) phantom[220] with five embedded 50 μm tungsten wires[240-242] spaced 1 mm from one another. PVA was prepared using a method described previously.[243] The phantom was then imaged using 1210 nm PAT with five grayscale images collected with the transducer focused on individual tungsten wires. The PAT gain was also tuned to minimize beamforming artifacts, which are typically seen with over absorption of pulsed laser light. A MATLAB script was then used to perform plot-profile analysis, which displays pixel intensity along a user-defined line. Plot profile analysis was performed to calculate the full width at half maximum (FWHM) in both the axial and lateral directions (**Figure 6.1**). The axial and lateral resolutions were then calculated using the FWHM and the known diameter of the tungsten wire (D_t) as shown in the **Equation 6.1:**[186]

$$\text{Resolution} = \sqrt{(\text{FWHM})^2 - (D_t)^2} \qquad \textbf{Equation 6.1}$$

6.3.3 Small Animal Atherosclerosis Induction

Murine atherosclerosis was induced using the partial carotid ligation (PCL) procedure on apolipoprotein E-deficient (ApoE KO) mice (**Appendix B Figure 1**).[244] ApoE KO mice were obtained from Jackson Laboratory (Bar Harbor, ME) and fed a standard chow diet until the time of surgery. All animals were anesthetized using a small animal anesthesia system (SomnoSuite, Kent Scientific) using 2-3% isoflurane and 225 mL/min room air,[189] and vital signs were closely monitored to ensure optimal anesthetic induction. Aseptic technique was used to sterilize the animal prior to exposing the left carotid artery (LCA) and ligating the internal, external, and occipital arteries. The superior thyroid artery was left open, thus inducing disturbed flow characterized by both low and oscillatory shear stress.[244] The incision was then closed using 7-0 prolene sutures and monitored until it is fully ambulatory. Buprenorphine was subcutaneously injected near the incision site at a dose of 0.05-0.1 mg/. Finally, all animals were placed on a western diet (TD.88137, Envigo) consisting of 42.7% carbohydrates, 42% fat, and 15.2% protein. Pulsed wave Doppler was used to confirm disturbed biphasic flow, and 4DUS and color Doppler were used to verify the complete ligation of the appropriate arteries. The Purdue Animal Care and Use Committee approved all of the outlined animal procedures and experiments.

6.3.4 Murine Atherosclerotic Plaque Lipid Burden Validation

6.3.4.1 *Ex Vivo* Common Carotid Artery Image Acquisition

Ex vivo characterization on atherosclerotic carotid arteries was performed to assess the capability of our PAT system to identify and quantify lipid burden. ApoE KO mice were separated into three groups consisting of 2±0 week post-PCL male mice (n=4), 4±0 week post-PCL male mice (n=3), and 6±1.7 week post-PCL female mice (n=4). Atherosclerotic plaques were surgically induced via the PCL procedure, followed by euthanasia and excision of the LCA and supporting tissue at the appropriate timepoints. We then performed 3D PAT/US imaging of the LCA using 1210 nm light for lipid-specific imaging and 1400 nm for off-resonant imaging.

Ten frames were acquired at each location and then processed using median averaging to minimize PAT fluctuations and laser-induced noise.

6.3.4.2 PAT Lipid Burden Quantification

All excised vessels were sectioned at multiple locations (n=27) and stained with lipophilic Oil Red O (ORO). A thresholding algorithm was used to quantify the percent lipid composition from the histological sections and compared to the PAT signal-to-noise ratio (SNR) at the same anatomical locations. Briefly, a thresholding algorithm was applied to the green channel of the ORO histology images to discriminate lipid dense pockets from surrounding tissues. The area of these lipid dense pockets was then divided by the cross-sectional area of the carotid artery to quantify lipid composition. PAT SNR was obtained by measuring the lipid signal intensity from the grayscale short-axis carotid artery image divided by a 16x16 pixel background region of interest. The location of the histological section was then matched to the location of the short-axis carotid artery PAT image. Finally, regression statistics were used to assess the goodness of fit between the lipid composition and PAT signal.

6.3.5 Cross-Sectional Photoacoustic and Longitudinal Ultrasound Plaque Assessment

6.3.5.1 Photoacoustic and Ultrasound Image Acquisition

In vivo hemodynamic, morphological, and kinematic changes, as well as *in situ* plaque lipid composition and volume were quantified in both the LCA and right carotid arteries (RCA) using a small animal ultrasound system (Vevo 3100, FUJIFILM VisualSonics) and the PAT system described in section 6.3.1. **Table 6.1** contains a summary of all animal groups and imaging timepoints. PCL procedure and administration of western diet was performed on all animals at six weeks of age. Briefly, 1100 nm and 1210 nm PAT was used for blood and lipid characterization, respectively. The ultrasound imaging protocol included acquisition of pulsed wave Doppler (PWD) for mean and peak antegrade and retrograde flow quantification, M-mode for green-langrage circumferential cyclic strain measurements, and respiratory-gated 4DUS for diameter and volume quantification, as well as maximum first-principal Green-Lagrange strain using a DDE method.[239] The 4DUS data was specifically acquired using standard acquisition, sharp processing style, frame rate of 300 Hz, and a step size of 0.05 mm. Moreover, five PWD and M-mode measurements were acquired between the carotid artery bifurcation and clavicle to

track regional changes in vessel hemodynamics and kinematics. The mice were then euthanized at the study endpoint and perfused with saline and 1% agarose. The left and right common carotid artery were then exposed and imaged *in situ* using 3D PAT and ultrasound with 1100nm, 1210 nm, and 1400 nm light for blood and lipid burden quantification as described in section 6.3.2.

Table 6.1: Summary of experimental animal groups and ultrasound imaging timepoints. Light blue box, dark blue box, and E denote ultrasound, PAT, and euthanize timepoints, respectively.

Purpose	Experimental Groups	n	Imaging Timepoints (Days)					
			0	1	4	7	10	14
Lipid deposition over time	Day 7 Post-PCL	8				E		
	Day 10 Post-PCL	8					E	
	Day 14 Post-PCL	8						E
	Sham Control	5						E
Strain predictor of lipid deposition	Day 4 Post-PCL	5			E			
	Day 4 Post-PCL without WD	6			E			

6.3.5.2 Hemodynamic and Kinematic Characterization

Mean and peak blood flow velocities were quantified in Vevo LAB (FUJIFILM, VisualSonics) by segmenting five pulsed wave waveforms at each location for all timepoints. A custom MATLAB (R2018a, Mathworks Inc., Natick, MA) algorithm was used to execute a DDE method to calculate the Green-Lagrange strain as previously described.[238; 239] Briefly, we first resampled the 4DUS dataset into 50 μm^3 isotropic voxels prior to DDE analysis of the Green-Lagrange strain. This algorithm utilizes Gauss-Newton optimization to iteratively minimize voxel intensity differences between 3D volumes at successive timepoints by updating the warping function parameter. This warping function parameter spatially maps the voxels between the undeformed volumes at timepoint t_1 to deformed volumes at timepoint t_2. Following optimization, the warping function is utilized to directly compute the deformation gradient tensor, which is then used to calculate the 3D maximum principal Green-Lagrange strain. The first maximum principal Green-Lagrange strain is then overlaid onto the solid carotid artery mesh to visualize the changes in pulsatility throughout the vessel. We also compared day 14 post-PCL DDE method derived strain measurements to M-mode derived circumferential cyclic strain measurements using **Equation 6.2**. In this equation, D_{sys} and D_{dia} represent the vessel diameter at

systole and diastole, respectively. Three distinct M-mode measurements were performed at five different regions along the day 14 post-PCL dataset.

$$\epsilon = \frac{1}{2}\left[\left(\frac{D_{sys}}{D_{dia}}\right)^2 - 1\right] x\ 100\% \qquad \textbf{Equation 6.2}$$

6.3.5.3 Morphological Characterization

Carotid artery diameters and volumes were quantified by first extracting the systolic timepoints from the 4DUS data using the FSL toolbox (FMIRB, Oxford) and segmenting the lumen in SimVascular.[156] Outer wall segmentations were not performed due to difficulty differentiating the artery from surrounding tissues. The segmentation path was created by placing control-points along both the LCA and RCA, followed by placing contours along the generated path to specifically segment the lumen. Solid models of these 3D segmentations were exported as STL files and imported into Meshmixer (Autodesk Research, California) to calculate the lumen volumes. Additionally, these STL files were then imported into MATLAB to extract diameter measurements along the carotid artery to quantify regional morphological changes throughout the study.

6.3.5.4 Lipid Deposition and Hemoglobin Localization

A custom MATLAB script was utilized to quantify lipid and hemoglobin deposition and volume throughout the carotid artery. We performed quantitative analysis on all 1210 nm lipid datasets, as well as 1100 nm hemoglobin datasets that were confirmed to be successfully saline and agarose perfused using gross dissection images (**Appendix B Figure 1**). PAT-specific optical contrast was first quantified using a thresholding technique to discriminate lipid from background pixels in an approximately 7x3mm region of interest around the carotid artery.[196] Carotid arteries were then segmented from long-axis ultrasound images to ensure that the data analysis does not include contrast from extraneous tissues and image artifacts. We then calculated pixel-wise SNR by dividing the lipid-specific pixel intensity by the background noise that is measured using a 16x16 pixel region of interest. The lipid and hemoglobin-specific SNR was then averaged along the short-axis slices along the carotid artery to plot the lipid distribution throughout the vessel. The pixels associated with PAT signal in this 3D dataset were also used to calculate lipid and hemoglobin volume, as shown in **Equation 6.3**.

$$\text{Lipid Volume} = P_L \times P_W \times P_T \times P_L \qquad \textbf{Equation 6.3}$$

Here pixel length (P_L) and width (P_W) are determined by user imputed calibration using the ultrasound scale bar, pixel thickness (P_T) was set by the 0.193mm elevational resolution of our ultrasound transducer, and the number of lipid-specific pixels (P_L) was determined through the MATLAB script.

6.3.5.5 Histology and Immunohistochemistry

We dissected the LCA and RCA from the animal and fixed the tissue in 4% paraformaldehyde (Thermo Fisher Scientific) for approximately 24 hours, followed by snap freezing in optimal cutting temperature (Thermo Fisher Scientific). The vessels were then processed for hematoxylin and eosin (H&E), Movat's pentachrome, ORO histological staining, as well as F4/80 macrophage immunohistochemistry. Inflammatory burden was quantified by performing color deconvolution to calculate percent F4/80 stain with respect to the cross-sectional area of the histological section.

6.3.6 Statistical Analysis

All datasets were assessed using normality test prior to statistical testing. Linear regression statistics was performed to assess correlation between plaque lipid composition versus lipid specific PAT SNR. One way ANOVA with tukey post-hoc test was used to assess statistical significance in ex vivo plaque lipid composition, macrophage infiltration, and histological outer diameter. Additionally, linear mixed-effects models statistical tests were performed on log transformed mean and peak velocity, volume/length, diameter, strain, and compositional responses. For simplicity, p-values are defined at $p<0.05$. We performed all statistical analyses in Statistical Analysis Software (SAS) and Prism 7 (GraphPad).

6.4 Results

6.4.1 Photoacoustic Tomography Resolution Characterization

Spatial resolution was characterized using five 50 μm tungsten wires that were inserted into 20% tissue-mimicking PVA. **Figure 6.1A-B** shows the PAT images of these wires, as well as the PAT signal amplitude along the axial and lateral directions. Our results showed small depth-wise variation in resolution with the axial resolution measured to be 48±8 μm and lateral resolution measured to be 243±11 μm (**Figure 6.1C**).

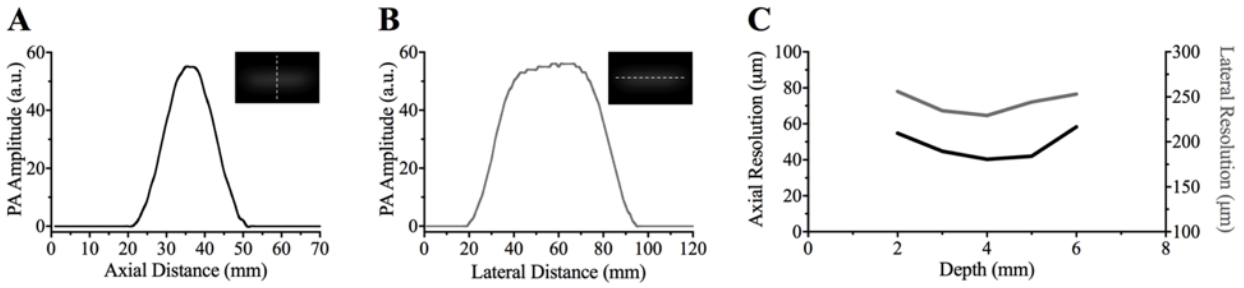

Figure 6.1: Axial (A) and lateral (B) profile of PAT signal amplitude using 20% PVA with five embedded 50 μm tungsten wires. Depth profiling resolution measurements with 1210 nm light revealed axial resolution of 48±8 μm and lateral resolution of 243±11 μm (C). Insets in A and B show PAT images of tungsten wire and profile measurement location (white dotted line).

6.4.2 *Ex Vivo* Carotid Artery Lipid Burden Results

Qualitative assessment of ORO stained LCA revealed a diverse spectrum of vessel morphology in mice two weeks post-PCL. The murine plaque phenotype ranged from fibrotic plaques with visible wall thickening (**Figure 6.2A**), complete occlusion with lipid accumulation through the lesion (**Figure 6.2B**), and severe lipid accumulation without complete occlusion of the carotid artery (**Figure 6.2C**). Quantitative assessment of PAT images (**Figure 6.2D,E**) showed that on average all three murine groups formed plaques with similar lipid dense regions regardless of sex and post-PCL euthanasia (**Figure 6.2F**). Particularly, we observed 9.4±5.6% lipid composition in 2-week post-PCL male mice, 12.4±5.7% lipid composition in 4-week post-PCL male mice, and 11.0±3.5% lipid composition in 6±1.7 week post-PCL female mice. These results also showed considerable variation in lipid dense regions and, as a result, no statistical significance amongst the three experimental groups (p>0.05). We then assessed our capability to use PAT SNR ratio to quantify lipid dense regions in the plaque-rich LCA. We found that linear

regression statistics resulted in R^2 value of 0.73 (p<0.001) when using 27 spatially correlated short-axis PAT and ORO histological sections (**Figure 6.2G**).

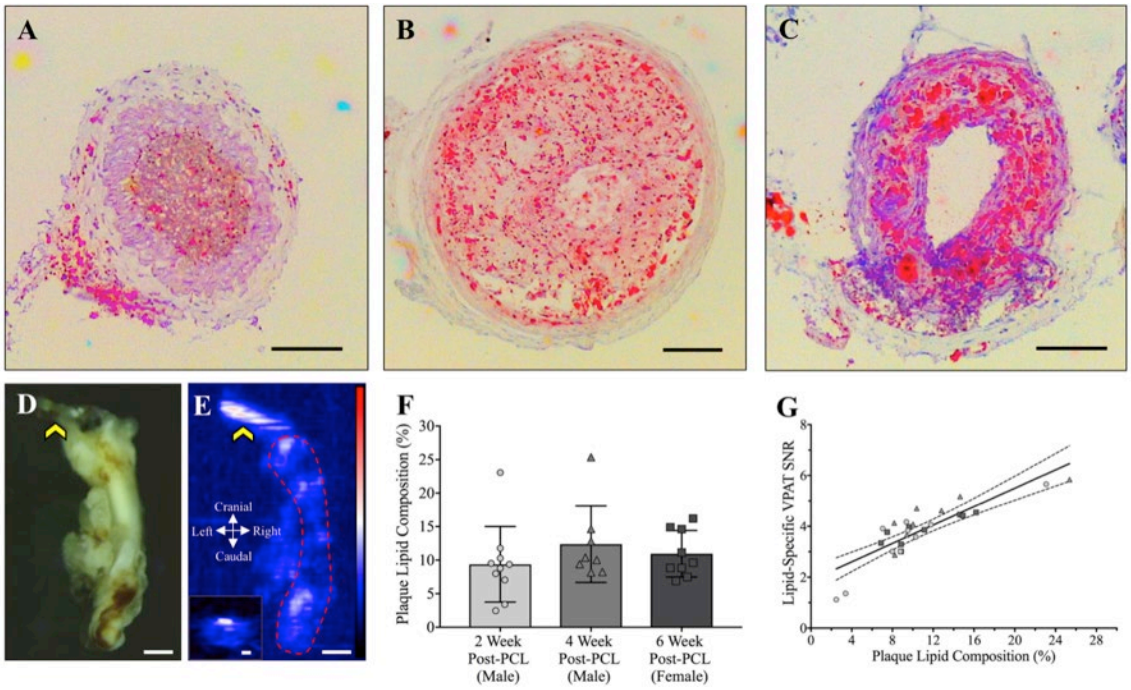

Figure 6.2: Validation of PAT to quantify lipid burden in a murine model of atherosclerosis. Lipid accumulation in mice that underwent a PCL varied greatly between animals as shown by ORO stained histology (A-C). Comparison of gross (D) and PAT (E) LCA (red dotted line) shows adequate spatial correlation of lipid signal. Suture is highlighted by yellow arrow. Plaque lipid composition did not vary significantly between 2 and 6±1.7 weeks post-PCL procedure regardless of sex (F). Linear regression statistics of plaque lipid composition versus lipid specific PAT SNR showed positive correlation (R^2=0.72, n=27, p<0.001; G). Scale bar A-C, Inset E: 100 µm, E: 1mm.

6.4.3 Hemodynamic and Kinematic Characterization Results

Hemodynamic assessment of pulsed wave Doppler images revealed initiation of disturbed flow in the LCA (**Figure 6.3A-B**) and maintenance of laminar flow in the RCA post-PCL (**Figure 6.3C**). Quantification of LCA velocities also confirmed disturbed flows with a 76% average decrease in mean antegrade velocities (**Figure 6.3D)** and an overall increase in retrograde velocities (**Figure 6.3E)** post-PCL. Regional assessment of both antegrade and retrograde velocities showed statistically greater velocities in the proximal (R4 and R5) compared to the distal (R1 and R2) regions ($p<0.05$) until day 7, and an overall significant decreased in mean velocities between days 1 and 14 post-PCL ($p<0.05$). The RCA revealed a slight decrease in mean velocities between day 0 and days 1 and 4 due to the surgical procedure. We then observed an increase in mean velocities on days 7 and 10, followed by a subsequent

decrease in mean velocity on day 14 (**Figure 6.3F**). Peak velocity measurements showed similar trends compared to the mean velocity data, as found in **Appendix B Figure 2**. The sham hemodynamic data for both carotid arteries followed a similar trend to the experimental RCA results (**Appendix B Figure 3).**

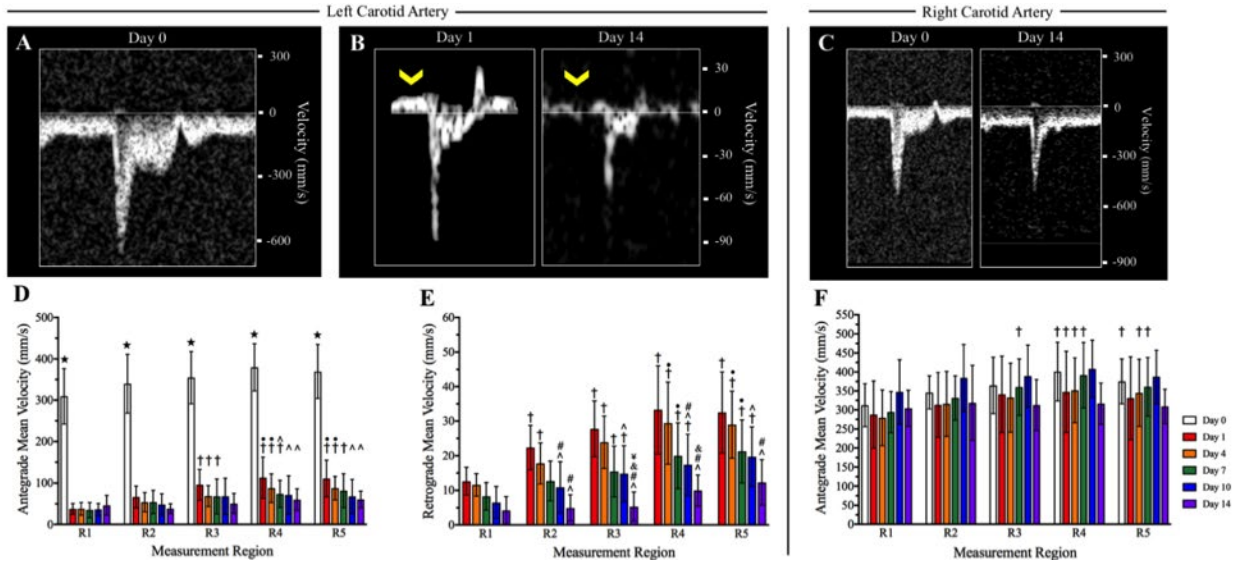

Figure 6.3: Hemodynamic characterization of LCA mean velocities between day 0 (A) and days 1 through 14 post-PCL (B) reveals statistically significant decrease in antegrade blood flow (D) and increase in retrograde blood flow (E). Proximal regions (R4 and R5) had statistically greater antegrade and retrograde velocities compared to distal regions (R1 and R2) until day 7, as well as a steady decrease in overall velocity until day 14. Conversely, the contralateral control RCA revealed healthy pulsed wave Doppler (C) and antegrade flow velocities (F) over 14 days. Statistical significance: $p<0.05$ (□ = significance compared to all other days in same region, † = significance compared to the same day in region 1, • = significance compared to the same day in region 2, ∧ = significance compared to day 1 in the same region, # = significance compared to day 4 in the same region, & = significance compared to day 7 in the same region, and ¥ = significance compared to day 10 in the same region).

Strain characterization using the DDE method revealed heterogeneous pulsatility in both the left (**Figure 6.4A-D**) and right (**Figure 6.4E-H**) carotid arteries. Regional assessment of LCA strain showed an exponential decrease in strain during the 14-day study (**Figure 6.4D**) with a large reduction in strain amongst days 0 (19.1±4.5%), 1 (12.7±4.1%), 4 (7.8±3.6%), and 7 (4.9±2.1%). The RCA strain values, however, maintained vessel pulsatility throughout the study (Day 1: 21.8±5.2%; Day 14: 22.6±4.3%; **Figure 6.4H**). Comparison of day 4 post-PCL strain results with and without Western diet feeding showed no statistical difference in vessel pulsatility (**Appendix B Figure 4)**. Interestingly, the sham strain data indicated a decrease in vessel pulsatility post-PCL, followed by return to healthy values by day 10 (**Appendix B Figure**

3). A comparison of strain values using the DDE method and M-mode analysis revealed similar pulsatility trends in both carotid arteries (**Appendix B Figure 5)**.

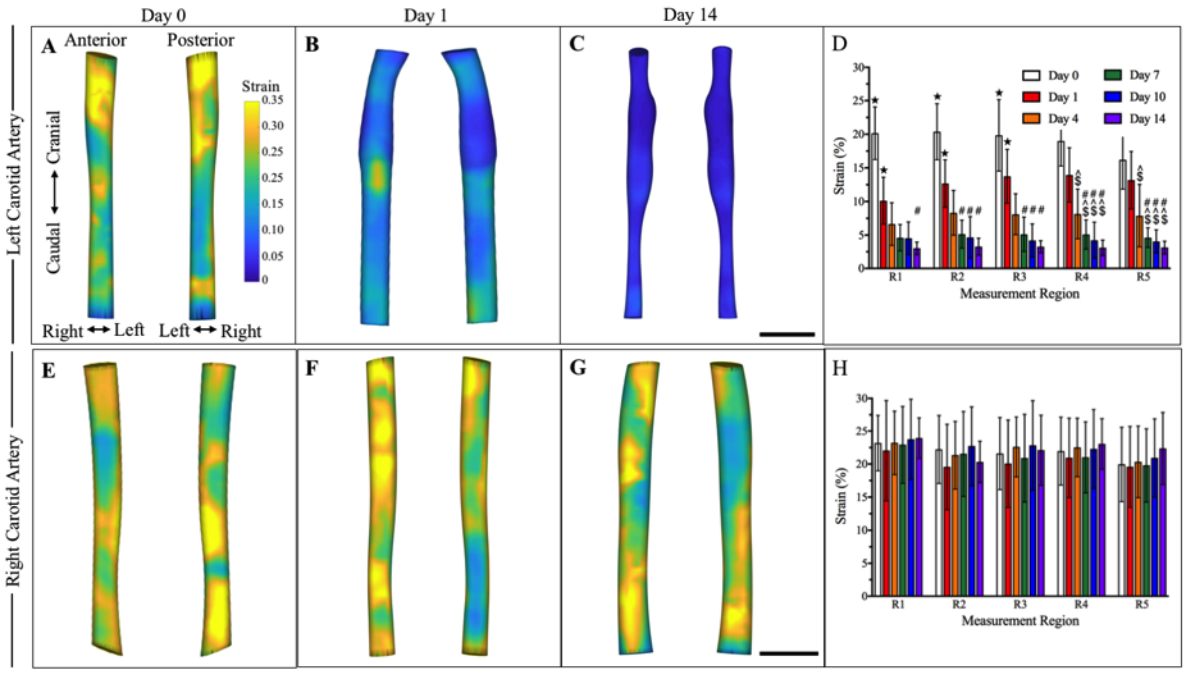

Figure 6.4: Representative 3D images of maximum first-principal Green-Lagrange strain in the LCA post-PCL (A-C) and the contralateral control RCA (E-G). Regional assessment of strain in the LCA (D) suggest decrease in vessel pulsatility after suture placement at day 1 followed by steady decrease until day 7. Strain measurements in the RCA suggest healthy vessel pulsatility. Strain values were overlaid on segmented volumes for visualization. Statistical significance determined at $p<0.05$ (= significance compared to all other days in same region, $ = significance compared to day 0 in the same region, ∧ = significance compared to day 1 in the same region, and # = significance compared to day 4 in the same region). Scale bar: 1mm.

6.4.4 Morphological and Compositional Characterization Results

Morphological analysis indicated interesting vessel remodeling in both the left (**Figure 6.5A-B**) and right (**Figure 6.5C-D**) carotid arteries. Diameter measurements suggest no changes in vessel morphology between days 0 and 4 (**Figure 6.5F)**. Volume/length measurements, however, clearly show dynamic changes in the LCA size between days 1 and 4 with some animals experiencing an increase in volume/length and others experiencing a decrease in volume/length (**Figure 6.5E**). At days 10 we observe a 24.7% decrease in volume/length and at day 14 we find a 53.6% decrease in volume/length compared to day 4 ($p<0.05$). Interestingly, the diameter measurements reveal statistically significant stenosis in region 5 by day 4 ($p<0.05$), while regions 1-4 show a statistically significant decrease in diameter much later at day 10 ($p<0.05$). Compensatory effects of RCA due to LCA stenosis can be seen in volume/length

values as early as day 4 (**Figure 6.5G**; $p<0.05$). The RCA also shows signs of gradual increase in diameter (**Figure 6.5H**) between days 0 (0.46±0.05mm) and 14 (0.51±0.05mm). Sham morphological data show no statistically significant changes in vessel diameter or volume/length (**Appendix B Figure 3)**. Volume data has been provided in **Appendix B Figure 6**.

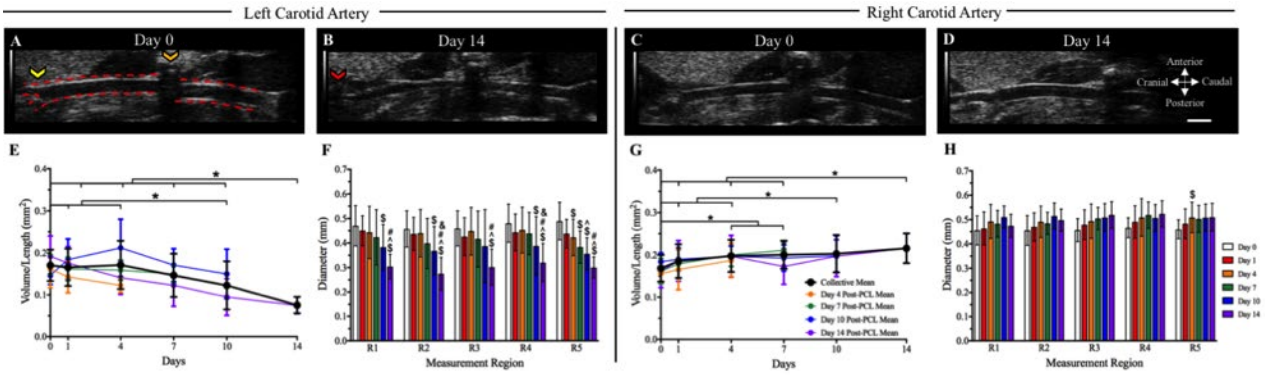

Figure 6.5: Morphological characterization of LCA between days 0 (A) and 14 (B) suggests heterogeneous remodeling response due to PCL until day 7, followed by rapid reduction of both volume/length (E) and diameter (F). Moreover, statistically significant increase in RCA volume/length (G) and increase in diameter (H) from day 0 (C) through day 14 (D) suggests compensatory remodeling due to LCA stenosis. Statistical significance determined at $p<0.05$ (* = significance between groups, $ = significance compared to day 0 in the same region, ∧ = significance compared to day 1 in the same region, # = significance compared to day 4 in the same region, & = significance compared to day 7 in the same region, and ¥ = significance compared to day 10 in the same region). Scale bar: 1mm.

Hemoglobin PAT contrast revealed regions of blood accumulation at days 10 and 14 (**Figure 6.6A-F**). We observed rapid, yet variable, hemoglobin accumulation between days 7 and 10 post-PCL ($p<0.05$,**Figure 6.6M**), especially in the cranial most region. Hemoglobin volume data suggests a 98.9% increase in blood accumulation between days 10 and 14 (**Figure 6.6N**). PAT lipid deposition and volume measurement revealed similar trends as the morphological data. We see a statistically significant increase in lipid deposition, as quantified by 1210 nm SNR, at day 10 along the carotid artery (**Figure 6.6G-I**). Interestingly, two out of eight animals showed the presence of lipid accumulation at day 7. We also observe a 131.5% increase in lipid-specific SNR between days 10 and 14 with statistically greater lipid deposition ($p<0.05$) in the proximal region (R4 and R5) compared to the distal region (R1 and R2; **Figure 6.6G**). The day 4, sham, and contralateral control carotid arteries showed no to minimal signs of lipid or hemoglobin accumulation. Lipid volume data indicated a similar trend with a statistically significant increase ($p<0.001$) in lipid volume between days 7 (0.27±0.33mm^3) and 14 (0.91±0.42 mm^3; **Figure 6.6H**). Additionally, we observe an increase in lipid accumulation between 7 and 10 but maintenance of lumen volume/length followed by a substantial decrease in day 14 volume/length

(**Figure 6.6I**). Hemoglobin and lipid deposition graphs for individual groups have been provided in **Appendix B Figure 7 and 8**.

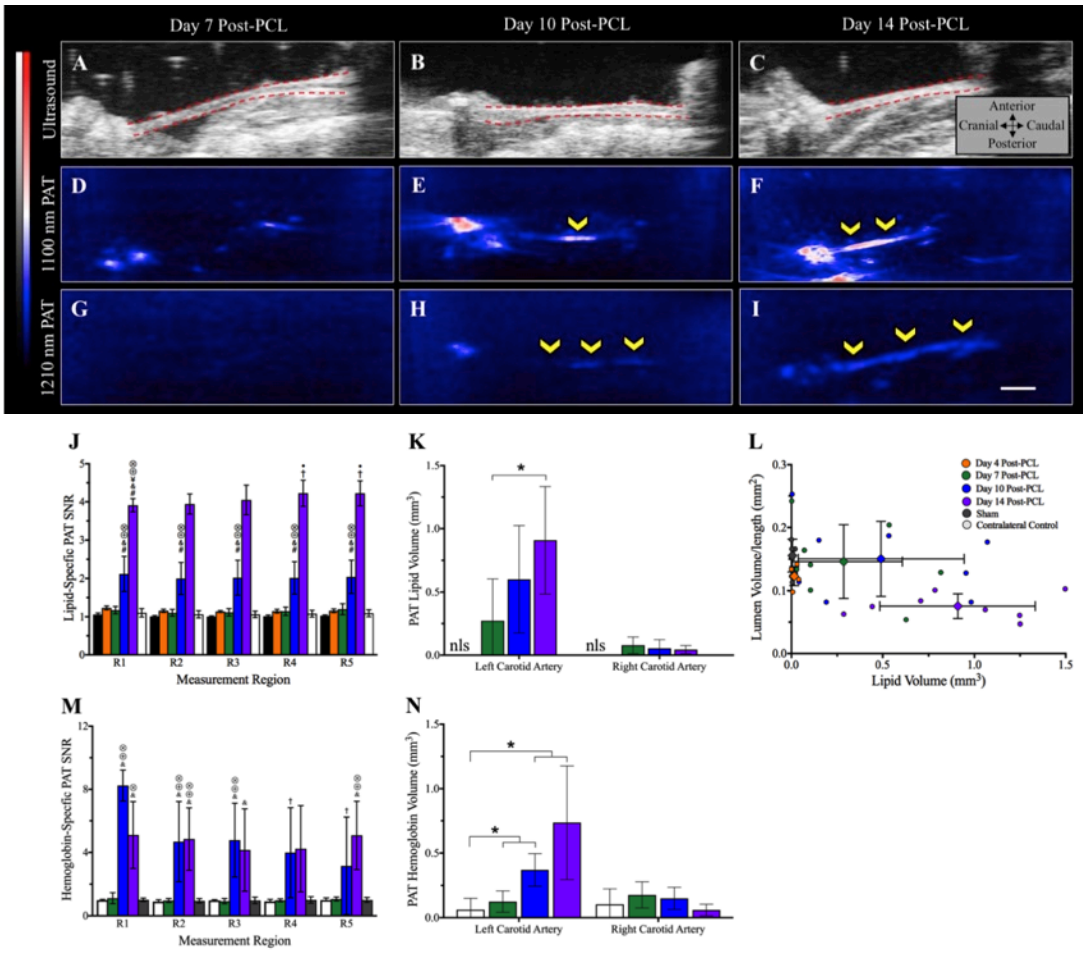

Figure 6.6: Representative *in situ* ultrasound (A-C), 1100 nm PAT (D-F), and 1210 nm PAT (G-I) images of LCA at days 7, 10, and 14 post-PCL. Regional assessment of lipid specific PAT SNR (G) and PAT lipid volume (H) suggests statistically significant and rapid lipid accumulation between days 7 and 14, with greater lipid accumulation in the proximal most regions at day 14. Comparison of the lipid volume and lumen volume/length suggests compensatory remodeling of the LCA until day 10, potentially due to Glagov remodeling, followed by rapid decrease in lumen volume and increase in lipid volume. Statistical significance determined at $p<0.05$ (* = significance between groups, † = significance compared to the same day in region 1, # = significance compared to day 4 in the same region, & = significance compared to day 7 in the same region, ⊗ = significance compared to sham group, ⊕ = significance compared to right contralateral control RCA). Scale bar: 1mm.

6.4.5 Histology

Histological assessment of the LCA confirmed significant vessel remodeling during the first two weeks post-PCL. H&E staining revealed LCA stenosis by day 10 for all experimental animals (**Figure 7A-D**) and at day 7 in two out of the eight experimental animals (**Figure 7B**). The ORO histology verified the rapid LCA lipid accumulation between days 7 and 10 (**Figure**

7E-H). Interestingly, Movat's pentachrome confirms the presence of neovascular formation by day 10 post-PCL (**Figure 7I-L**), as shown by red muscle staining around vessel-like structures. Magnified images of histology sections can be found in **Appendix B Figure 10.** Finally, F4/80 immunohistochemistry suggests inflammatory response initiation between days 4 (**Figure 6.7P-T**, **Appendix B Figure 10P-T**) and 7 (**Figure 6.7N**) followed by a slight increase in macrophage infiltration between days 7 and 14 (**Figure 6.7O,P**). Quantitative analysis of our F4/80 histology suggests percent macrophage compositions of 0% in the sham group and day 4 post-PCL without western diet, 1.2±1.4% in day 4 post-PCL with western diet mice, 2.6±2.4% in day 7 post-PCL mice, 11± 6.9% in day 10 post-PCL mice, and 17.8±2.6% in day 14 post-PCL mice. Further analysis of arterial cross-section revealed diameter measurement of 377.6±26.5µm at day 4 post-PCL without western diet, 352.1±29.5µm at day 4 post-PCL with western diet, 426.8±41.2µm at day 7 post-PCL, 496.5±67.6µm at day 10 post-PCL, and 543.6±72.3µm at day 14 post-PCL. The sham and contralateral control RCA histology shows diameter measurements of 360.6±32.8µm and 377.8±9.7µm, respectively, as well as patent vessels and no signs of inflammation.

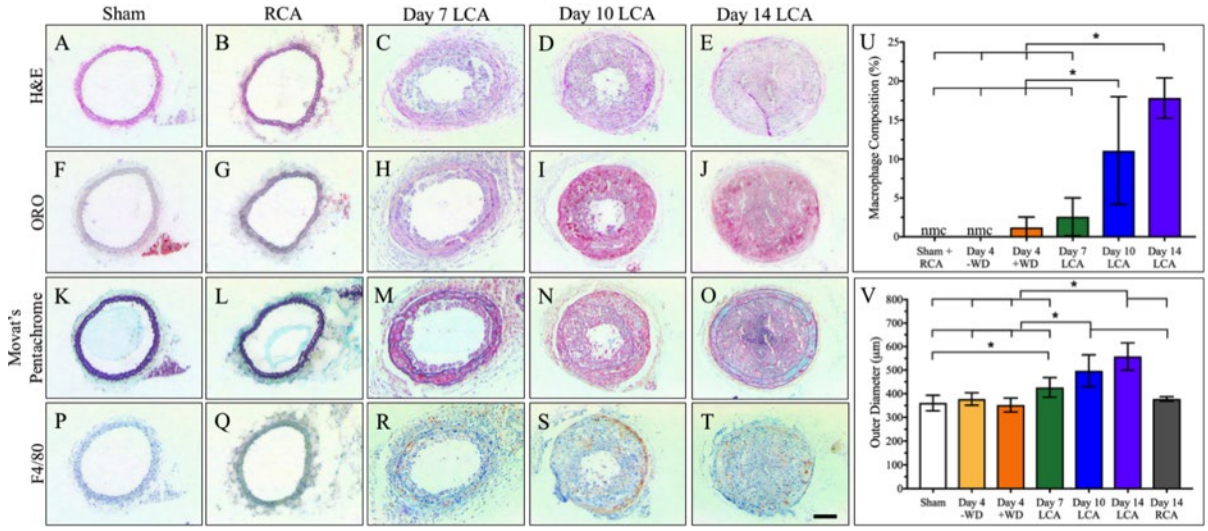

Figure 6.7: Histology and macrophage immunohistochemistry of day 7, 10, 14 post-PCL and sham groups, as well as contralateral control RCA. Staining consisted of H&E (A-E), ORO (F-J), Movat's pentachrome (K-O). Macrophage infiltration was assessed with F4/80 immunohistochemistry (P-T) and revealed rapid inflammation between days 4 and 10 (U). LCA measurements showed a 46.1% greater outer wall diameter in day 14 post-PCL compared to sham mice (V). Statistical significance determined at $p<0.05$. Scale bar: 100 µm.

6.5 Discussion

Here, we investigate using dual-modality PAT and ultrasound to study disease progression in a surgically induced murine model of atherosclerosis. Numerous mouse models

have been developed to mimic various aspects of atherosclerosis pathology that include western diet feeding,[245] perivascular carotid cuff placement,[246] complete carotid artery ligation,[247; 248] and PCL[244] in atheroprone mice. This study specifically utilized the ApoE KO PCL procedure as this model has been shown to create disturbed flow throughout the carotid artery that leads to rapid and measurable plaque accumulation.[244; 249-251] The presence of decreased antegrade flow and increased retrograde flow also allows for a general measure of laminar and oscillatory shear stress. Moreover, histological assessment of these atherosclerotic lesions reveals diverse plaque morphology with regions of complete stenosis but limited lipid accretion and other partially stenosed lipid dense regions (**Figure 6.2**). Indeed, surgical induction of atherosclerosis using the PCL provides a robust model to assess how hemodynamics and kinematics impact vessel morphology and lipid deposition.

Current applications for murine PAT imaging of atherosclerosis is limited, as the literature has primarily focused on developing this technique for intravascular assessment of plaque stability in humans. Therefore, we provide evidence to assess the lipid composition of murine plaques by characterizing the resolution of our PAT system and performing quantitative *ex vivo* validation experiments. The resolution characterization of our PAT system revealed an axial resolution of 48±8 μm and a lateral resolution of 243±11 μm. All 3D PAT images were therefore acquired in the long-axis plane to account for our PAT resolution. Our *ex vivo* validation study provides further evidence of quantifying lipid burden as PAT SNR and plaque lipid composition have a positive correlation with R^2 of 0.72 ($p<0.001$). These results also suggest that on average all PCL-induced animals have comparable lipid accumulation past 2 weeks post-procedure. This is likely due to a reduction in proatherogenic agents as blood flow velocity (**Figure 6.3**) and lumen diameter decreases (**Figure 6.5**). Together, these validation experiments provide strong evidence to use PAT to quantify lipid burden in small animals.

Maximum first-principal Green-Lagrange strain values obtained from 4DUS datasets using the DDE methods were also compared to conventional M-mode analysis of circumferential cyclic strain. Our circumferential cyclic strain values for both LCA and RCA were comparable to previously published data.[252] Additionally, our maximum first-principal strain and circumferential cyclic strain values showed similar trends with both showing an exponential decrease in vessel pulsatility between days 0 and 7 (**Appendix B Figure 5**). Our maximum first-principal strain values, however, were slightly lower than the circumferential cyclic strain data

likely due to averaging between the more pulsatile anterior walls with the less pulsatile posterior walls.

Hemodynamic and kinematic characterization revealed abrupt changes in LCA forces as early as day 1 post-PCL. Mean velocity measurements show a 76% decrease in antegrade flow suggesting initiation of low shear stress and an increase in retrograde flow suggesting the presence of oscillatory shear stress. The manifestation of these altered forces in combination with suture-induced decrease in vessel pulsatility explains the rapid atherosclerosis progression in this mouse model. Regional assessment of LCA hemodynamics revealed statistically greater antegrade and retrograde velocity ($p<0.05$) in the proximal (R4 and R5) compared to distal regions (R1 and R2). This data suggests greater disturbed flow patterns in the proximal region, which may lead to increased endothelial dysfunction and more significant lipid deposition.

According to Bernoulli's principle, as the vessel diameter decreases the blood flow velocity should increase. Therefore, another noteworthy observation was statistically significant ($p<0.05$) decrease in antegrade and retrograde velocity throughout the study. Our color Doppler images (data not shown) revealed increased blood flow near the LCA bifurcation by day 7 post-PCL suggesting increase collateral artery formation or dilation of the superior thyroid artery. Additionally, our 1100 nm PAT images and Movat's pentachrome histology provided evidence for neovascular formation throughout the plaque. Day 10 hemoglobin-specific PAT contrast also suggests greater blood vessel formation towards the cranial compared to the caudal region. We suspect these regions to be intraplaque hemorrhages as we were able to obtain hemoglobin-specific optical contrast post-saline perfusion. These intraplaque hemorrhages can also be visualized through gross dissection images (**Appendix B Figure 1**). Together, our results suggest that blood flow velocity decreases in the LCA due to neovascular formation within and surrounding the vessel.

Morphological and lipid data provide additional supportive evidence to suggest that more proximal regions experience more aggressive atherosclerosis progression due to greater disturbed flows. Diameter measurements in region 5 revealed statistically significant stenosis as early as day 4 compared to statistically significant stenosis by day 10 in regions 1-4. Moreover, our lipid deposition results show a statistically greater lipid accumulation in the proximal region (R4 and R5) compared to the distal regions (R1 and R2) on day 14. This especially interesting as our volume/length data shows a dynamic change in vessel size between days 0 and 4, followed by

significant stenosis on days 10 and 14 ($p<0.05$) where we also observe the presence of robust lipid signal. We also observed lipid contrast through PAT in two out of eight day 7 post-PCL animals, which was confirmed with H&E and ORO histology. Analysis of lipid volume versus lumen volume/length provides evidence for Glagov remodeling as the vessel resists stenosis between days 4 and 10 followed by a rapid decrease in lumen volume/length by day 14 (**Figure 6.6**).[253-255] Quantitative histological analysis revealed a 46.1% greater LCA outer diameter in day 14 post-PCL compared to sham animals. In humans, approximately 60% of large elastic arteries adhere to Glagov remodeling, which may explain the large variability in our murine study.[255; 256]

Contralateral control RCA metrics were also quantified and compared to the experimental LCA. Overall, we observe maintenance of healthy pulsatility and increase in volume/length ($p<0.05$) and diameter to compensate for the decreased flow through the LCA. Interestingly, the statistically significant increase in RCA volume/length as early as day 4, before LCA stenosis, may suggest a preparatory remodeling response due to decrease flow through the LCA. Sham animals did not show an increase in carotid volume/length, thus confirming that this change is not attributed to the natural growth of these young animals. Further, we observed a decrease in RCA velocity at days 1 and 4 post-PCL as the animals recover from the procedure (**Appendix B Figure 9**). The velocity in the RCA returns by day 7 but decreases again by 19% between days 10 and 14 post-PCL. The sham group shows a similar response suggesting that the Western diet may have systemic effects on cardiovascular hemodynamics.[257; 258]

We also investigated the use of strain as a predictor of atherosclerosis induction. We observed a statistically significant decrease in vessel pulsatility at day 1 post-PCL due to suture placement and a second substantial decrease in strain at day 4 post-PCL. We hypothesized that this second decrease in strain may be due to the initiation of atherosclerosis progression as marked by macrophage infiltration and early lipid deposition. Therefore, subsets of animals were imaged until day 4 post-PCL with (n=5) and without (n=6) Western diet feeding. We did not see a significant difference in regional strain between these groups suggesting that acute changes in vessel pulsatility are mainly due to the suture placement, as previously shown in the iliac artery.[259] H&E, ORO, and F4/80 staining also confirmed the lack of inflammation and subsequent plaque formation.

Indeed, previous works have utilized advanced imaging techniques to study the multifaceted nature of atherosclerosis pathology,[252; 260-263] however, limited work has been done

towards using PAT to correlate regional changes in hemodynamics and kinematics to lipid deposition and vascular remodeling. The work highlighted here is novel as we provide evidence to show the positive correlation between plaque lipid composition and lipid-specific PAT SNR using a small animal model of atherosclerosis ($R^2 = 0.72$, $p<0.001$). Advanced methods using 4DUS were also developed for morphological and strain quantification. Finally, we performed a study with 40 animals to demonstrate the capability of dual-modality PAT and ultrasound to elucidate the complex nature of lipid lesion development.

This study also highlights several limitations that may inspire future work. The advantage of *in situ* PAT is that the majority of the light is delivered to the tissue of interest; thus, calibration methods are not required to account for optical properties of more superficial endogenous absorbers. The disadvantage, however, is the lack of longitudinal *in vivo* imaging limits lesion development characterization. Moreover, the lack of vascular pressure makes it is difficult to correlate heterogeneous 4DUS strain data with lipid deposition and assess differences in lipid accumulation in the anterior versus posterior walls. Future work should, therefore, be performed to identify the optimal illumination geometry and transducer bandwidth for deep murine lipid imaging.[1; 264; 265]

6.6 Conclusions

The data presented here provides proof-of-concept towards using PAT for murine atherosclerosis imaging. Strain analysis reveals the heterogeneous pulsatility throughout both the LCA and RCA. Morphological and lipid data also provide evidence of murine Glagov remodeling with diverse vessel remodeling between days 0 and 7 followed by a rapid decrease in vessel size after day 10. Hemoglobin-specific PAT contrast also suggests intraplaque hematoma formation as early as day 10. These results revealed that regions of greater oscillatory flows experience more aggressive lipid deposition and earlier vascular remodeling failure than regions of healthier flows. Taken together, these results highlight the preclinical potential of utilizing dual-modality PAT and 4DUS to characterize and study atherosclerosis progression in small animal models.

6.7 Acknowledgements

The authors would like to acknowledge Dr. Arvin Soepriatna, Alycia G. Berman, and Daniel Romary for their support in the DDE method implementation, as well as Andrew Needles and Andrew Heinmiller for their support in the PAT system development. Funding was provided to Dr. Craig J. Goergen through the AHA Scientist Development Grant (14SDG18220010), Gurneet S. Sangha through the NSF Graduate Research Fellowship (DGE-1333468) and the NIH T32 Bioengineering Interdisciplinary Training for Diabetes Research (T32DK101001-05).

7. CONTRIBUTIONS TO SCIENTIFIC KNOWLEDGE

Recent advances in PAT have created various avenues for preclinical and clinical applications towards characterizing the development of atherosclerotic lesions. The work outlined in this dissertation builds on this knowledge for murine cardiovascular applications. Conventional quantitative vascular capabilities of standard small animal ultrasound were highlighted using a murine aneurysm model to assess changes in hemodynamics, biomechanics, and morphology. The feasibility of noninvasive *in vivo* lipid and blood imaging was then demonstrated and validated in a study with 24 animals. We carefully characterized the resolution, optimal illumination geometry, and penetration depth of a high-resolution PAT system capable of imaging in the second near-infrared window. A proof of concept study was performed to show the positive correlation between plaque lipid composition and lipid-specific PAT SNR using a small animal model of atherosclerosis ($R^2 = 0.72$, $p<0.001$, n = 27). Advanced methods using 4DUS and the DDE method were also introduced for morphological and strain quantification. Finally, we performed a study with 40 animals to demonstrate the capability of dual-modality PAT and ultrasound to elucidate the complex nature of lipid lesion development. These results revealed that regions of higher oscillatory flows experience more aggressive lipid deposition and earlier vascular remodeling failure than regions of healthier flows. Together, the work highlighted here provides a strong foundation towards expanding PAT capability for cardiovascular imaging with profound potential to improve knowledge regarding atherosclerosis pathophysiology, evaluation of novel therapeutics, and translation of clinically relevant techniques.

8. FUTURE WORK

The research described here has laid the foundation for future work regarding novel applications of dual-modality PAT and ultrasound. Further development of PAT techniques for noninvasive *in vivo* lipid imaging would expand our knowledge of disease pathology through longitudinal assessment of plaque formation. This technical advancement may be achieved through trans-tracheal catheter insertion, as well as investigation into optimal transducer bandwidths and illumination geometries. The following proposed proof-of-concept studies will showcase the utility of dual-modality PAT and ultrasound for advanced plaque and thrombus characterization. The results of these studies can potentially lead to the development of novel diagnostic imaging techniques to determine plaque rupture risk and thrombus composition. If successful, these methods will improve medical intervention for both arterial and venous disease.

Study 1: Lipidomics analysis of atherosclerotic plaques using PAT and mass spectrometry. Assessing the lipidomics during atherosclerotic plaque development may provide insight into lesion severity and help clinicians deliver more accurate treatment regimens. The work provided in this dissertation has shown utility in using PAT to quantify lipid localization, density, and volume. The objective of this study, however, is to develop methods to assess plaque lipidomics during atherosclerosis development. We hypothesize that multispectral PAT between 1100-1300 nm will produce unique spectra based on lipid-type that can then be used to perform nondestructive lipidomics in plaques. Our rationale is based on previous work that has shown the utility of using PAT to differentiate cholesterols fractions and perivascular fat [266]. Therefore, we expect to obtain unique spectra from other lipids commonly found in atherosclerotic lesions.

Lipidomics characterization capabilities of PAT will be validated through *in vitro* experiments by imaging the main constituents of atherosclerotic lesions; cholesterol, cholesterol esters, phospholipids, and triglycerides (Sigma Aldrich; [267]. Reagents will be placed in polyethylene tubing and imaged using multispectral PAT between 1100-1300 nm light in increments of 10 nm. We will then assess lipid composition of murine atherosclerotic plaques induced using the partial carotid ligation model [244]. Experimental groups will undergo atherosclerosis induction and will be euthanized at week 2 (n=10), 3 (n=10), and 4 (n=10) post-

PCL. A sham group will also be used as a control (n=10). We will perfuse saline and 1% agarose in the left and right carotid arteries, followed by volumetric multispectral PAT using the same imaging protocol as our *in vitro* experiments. The excised carotids will then be cut into 1 mm segments for mass spectrometry lipidomics analysis. We will then compare our atherosclerotic lesion PAT spectra to lipid reagent PAT spectra, as well as to our mass spectrometry results.

Anticipated Results: The relative breakdown of fatty acids in atherosclerotic plaques is 25% free cholesterol, 52% cholesterol esters, 14% phospholipids, and 9% triglycerides (263). We expect to see unique spectra for all of these lipid components, which will allow us to assess regional lipidomics in our murine atherosclerotic arteries. Mass spectrometry will verify the fraction of these lipids in our 1 mm tissue segments.

Potential Problems and Alternative Solutions: We may observe unique spectra in our *in vivo* studies that are not observed in our *in vitro* experiments due to more complex lipid composition. In this case, mass spectroscopy will be used to assess the complex composition of these lesions to begin a PAT plaque lipidomics library. We will then perform *in vitro* experiments mimicking these results to assess the accuracy of our *in vivo* PAT and mass spectroscopy observations.

Study 2: Characterization of deep vein thrombus composition using multispectral PAT. Thrombus has been shown to be biologically active and a promoter of cardiovascular disease. The objective of this study is to utilize multispectral PAT to characterize the composition and age of thrombus. We hypothesize that 760 nm and 850 nm blood-specific PAT contrast and ultrasound echogenicity differences can be used to assess the age and composition of venous thrombus. Thrombus composition is classified as phase I (fresh), phase II (young), phase III (intermediate), and phase IV (old) [268]. Our rationale is as thrombus matures the composition changes from largely red blood cells to fibrotic tissue; thus we can expect changes in PAT contrast and ultrasound echogenicity during disease development. C57BL/6J wild-type mice will undergo inferior vena cava ligation to induce deep vein thrombus, as previously described (265). Euthanasia timepoints are defined at day 1 post-procedure to produce acute thrombus (n=10) and 2 weeks post-procedure to produce chronic thrombus (n=10), as well as and 2 weeks post-procedure sham control group (n=10). Acute thrombus will be imaged on day 0, as well as 12- and 24-hours post-procedure, and chronic thrombus and sham control groups will be imaged

on days 0, 1, 4, 7, 10, and 14. Imaging protocol will include volumetric PAT and ultrasound imaging to obtain tissue-specific compositional information, which we can then use to assess thrombus age *in vivo*. After euthanasia, the vessels will be extracted to validate our *in vivo* results with hematoxylin and eosin, Elastica van Gieson, and movat's pentachrome histological analysis.

Anticipated Results: As the thrombus ages, we expect to see a decrease in blood-specific PAT signal and an increase in ultrasound echogenicity within each layer. "Young" and "fresh" thrombus should have abundant red blood cells and produce optical contrast with 850 nm with high ultrasound echogenicity. Red blood cells in "intermediate" thrombus will become deoxygenated and produce optical contrast at 750 nm with attenuation in ultrasound echogenicity. "Old" thrombus is typically fibrotic and will have limited optical contrast at 760nm and 860 nm with a hypoechogenic ultrasound signal.

Potential Problems and Alternative Solutions: Deep vein thrombus will be induced in the infrarenal aorta, which is susceptible to artifacts due to abdominal gas. We will stop volumetric PAT and ultrasound imaging acquisition for 1 hour to alleviate abdominal gas if these artifacts are present and severe.

APPENDIX A

A.1 Elastase Infusion Surgery

A small animal anesthesia system (SomnoSuite, Kent Scientific) was used to anesthetize all animals using 1-3% isoflurane and 225 mL/min room air, and toe pinch was used to ensure proper anesthetic depth. Mice were placed on a heated surgical stage (SurgiSuite, Kent Scientific), eye lubricant was applied to prevent corneal desiccation, and depilatory cream was used to remove hair from the abdomen. Aseptic technique was then used to clean and sterilize the animal prior to surgery. A mid-line incision was made through skin and muscle layers, and the organs were retracted to expose the inferior vena cava and aorta. We then used a surgical scope (M60, Leica Microsystems, Wetzlar, Germany) to separate the inferior vena cava and aorta, and temporarily ligate branching arteries. Sutures were also placed below the left renal vein and above the aortic trifurcation to create a 3 mm isolated elastase infusion zone. An aortotomy was created by placing a 30 gauge needle and a thinned polyethylene-10 catheter in the aorta, followed by holding the catheter in place using 6-0 silk suture. Porcine pancreatic elastase (PPE) at 2 U/ml was infused for 10 minutes, followed by closing of the aortotomy using 10-0 suture. Finally, we used 4-0 vicryl and 6-0 prolene sutures to close the muscle layer and skin later, respectively. Buprenorphine (0.03 mg/mL) was subcutaneously injected near the incision site at 0.05 mg/kg for pain management.

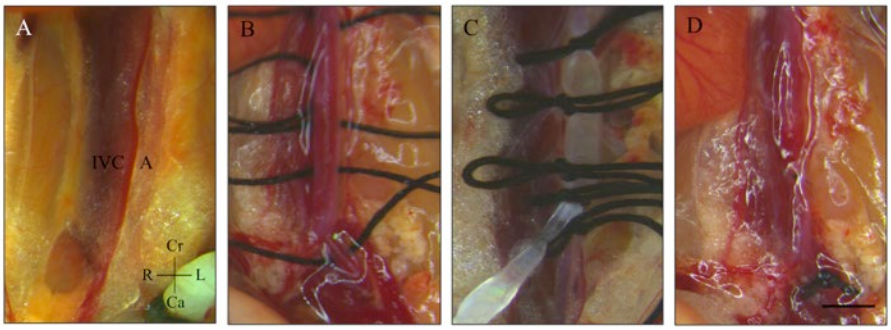

Appendix A Figure 7: Summary of PPE infusion procedure. Aorta and inferior vena cava were first exposed (A) and separated. 6-0 silk sutures were then placed to temporarily ligate branching vessels and infusion inlet and outlet zones, and permanently placed to partially ligate the iliac artery (B). Catheter was placed in the aorta via aortotomy (C) for 10-minute elastase infusion. Aortotomy was then closed using 10-0 suture, temporary sutures are removed, and single iliac artery was partially ligated (D). Cr: Cranial, Ca: Caudal, L: Left, R: Right. Scale bar denotes 2mm.

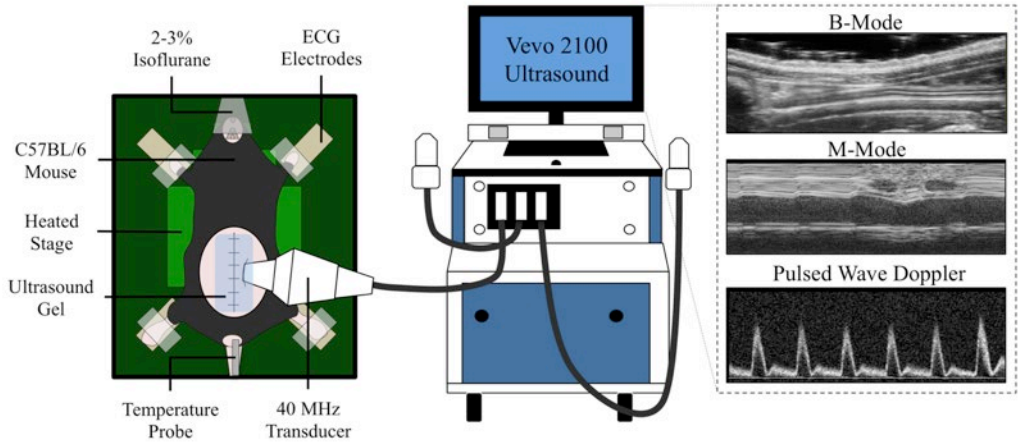

Appendix A Figure 8: Overview of ultrasound imaging procedure. Mice were anesthetized and placed on a heated stage where heart rate, respiration, and temperature are closely monitored to ensure animal safety. Ultrasound probe was appropriately placed on the animal to minimize artifacts due to suture and intestinal gas. After ensuring proper anesthesia induction, ultrasound imaging was performed to obtain structural and hemodynamic information.

A.2 Ultrasound Imaging

Mice were imaged using a high-resolution small animal ultrasound system (Vevo2100, FUJIFILM VisualSonics) with a 40 MHz central frequency transducer (MS550D). All animals were anesthetized using 2-3% isoflurane and 1.5 L/min medical grade air. To maintain and monitor healthy vital signs the mice were placed on a heated stage, all four paws were taped to gold electrodes to track heart rate and respiration, and a rectal probe was used to monitor body temperature. The orientation of the stage was adjusted to optimize view of the infrarenal aorta and iliac arteries and to minimize artifacts due to abdominal gas and surgical sutures. Hair on the animal was removed using depilatory cream and transmission ultrasound gel was used as an acoustic coupling agent between the ultrasound transducer and the skin (**Appendix Figure A2**).

A3 Murine Ultrasound Data Analysis

A3.1 Diameter and Volume Measurements

We quantified aortic diameters from the long-axis B-mode images, and aortic volumes were acquired from the 3D ultrasound data using the VevoLab software (FUJIFILM VisualSonics). For consistency, AAA diameter measurements were taken in the middle of the infrarenal aorta between the left renal vein and aortic trifurcation for all animals and time points (**Figure 2A**). Control contralateral iliac artery diameter measurements were acquired near the

aortic trifurcation and in the middle of the iliac artery (**Figure 3A**), while modified iliac artery diameter measurements were taken proximal and distal to the suture placement (**Figure 3B**). Five measurements were taken from each B-mode image to minimize location-dependent error. We obtained volume measurements by segmenting the infrarenal aorta using 3D short-axis B-mode data from the left renal vein to the aortic trifurcation, as described previously (**Figure 2B**).[269]

A3.2 Mean and Peak Velocities

To measure centerline blood flow velocity, we acquired velocity waveforms by PWD ultrasound. Cine loop acquisitions over 5 seconds were collected in long-axis along the infrarenal aorta and both the left and right iliac arteries. The waveform data were exported as DICOM files for analysis with a custom MATLAB script to obtain measurements of mean and peak blood flow velocity.[270; 271] As part of the MATLAB script, respiration-induced artifacts were removed to eliminate breathing related velocity errors.

A3.3 Circumferential Cyclic Strain Measurements

Circumferential cyclic strain was calculated using M-mode diameter measurements in the middle of the PPE exposed infrarenal aorta, as well as the left and right iliac arteries. Specifically, the anterior and posterior walls of the aorta were first identified using the echogenicity of the flowing blood. We then measured the minimum (end diastole; D_D) and maximum (peak systole; D_S) inner vessel wall diameter (**Figure 2C**). Green-Lagrange circumferential cyclic strain was calculated using:[192; 272]

$$(1) \qquad E_{\theta\theta} = \frac{1}{2}\left[\left(\frac{D_S}{D_D}\right)^2 - 1\right] x\ 100\ \%$$

A.4 Aortic Segmentation and Centerline Path Extraction

We performed 3D segmentation by first creating control-points along the path that was segmented. This path was then smoothed based on control points using Fourier mode number of 10. Contours were then created along the path to segment both the lumen and the outer wall of the diseased and projected healthy aorta. After segmentation we created a model that allowed us

to extract the centerline path of the vessel, which was used to quantify the magnitude and direction of centerline deviation.

A.5 Tissue Processing, Histology, and Cell Counting

The infrarenal aorta was resected en bloc with the adjacent vena cava, renal arteries, and kidneys. The bottom half of this tissue segment was carefully dissected to separate the aorta from adjacent tissues, stored in RNA later (Qiagen), and snap-frozen in liquid nitrogen for storage at –80°C. The upper half and adjacent tissues were fixed in 4% paraformaldehyde (Thermo Fisher Scientific) overnight for histology. Five μm sections of paraffin-embedded samples were mounted on SuperFrost © slides (Menzel) and stained with hematoxylin and eosin (H&E) and Elastica van Gieson (EvG). Finally, ImageJ was used to determined the cellular content in H&E aneurysm sections by counting cell nuclei in a 1 cm^2 region of interest (including the aortic media and intima) three times at 100x magnification.[157; 158]

A.6 Gene Expression Experiments

Gene expression was analyzed with quantitative RT-PCR. Total cellular RNA was extracted from 5 control aortae (non-operated C57BL/6J wild-type mice, 12 weeks old) and all PPE-treated mice in the study with TRIzol reagent (Invitrogen Life Technologies) as recommended by the manufacturer. RNA integrity was verified using the Experion automated electrophoresis station (Bio-Rad Laboratories Inc). Primer sets (Qiagen) were designed using PrimerBlast (http://www.ncbi.nlm.nih.gov/tools/primer-blast/) for IL-6 (Mm00446190_m1), VEGFA (Mm00437306_m1), KLF4 (Mm00516104_m1), and TGFß (Mm01178820_m1). The housekeeping gene was β-actin (ACTB) (Mm00607939_s1). For first-strand cDNA synthesis, 1 μg of total RNA was employed using the iScriptcDNA synthesis kit (Bio-Rad). Quantitative PCR was performed with the qPCRMasterMix kit for SYBR Green (BioRad). All PCR were carried out with a CFX96 RT-PCR system (Bio-Rad) operated by CFX Manager software (version 3.0). Each run was 40 cycles with denaturing conditions at 95°C for 15 s, annealing at 60°C for 1 min and extension at 65°C for 3 minutes. Results are displayed using the $2^{-\Delta\Delta Ct}$ value for fold change of expression compared to non-PPE-treated control aortae.

A.7 Ki67 and TGFβ Immunohistochemistry

Cryosections were for thawed for 20 minutes and fixed for 20 minutes in 4% PFA. To quench endogenous peroxidase activity, slides were incubated for 30 minutes in 3% H2O2 (Merck) at room temperature. Immunohistochemistry protocol for Ki67 and TGFβ was executed by first blocking for 1 hour in 5% normal goat serum with 1% bovine serum albumin (Sigma), followed by overnight incubation at 4°C with primary antibody diluted in blocking serum (Ki67 1: 200, Abcam; TGF-b-1 1:100, ab92486 rabbit polyclonal Abcam). The sections were then diluted for 30 minutes with biotinylated secondary antibody (goatantirabbit,1:200inPBS-T 5% goat serum). Afterwards the Vectastain ABC Reagent was applied according to the manufacturer's protocol (Vector Laboratories). Nuclear counterstaining was performed with DAPI (diluted 1:2000 in water; Carl Roth) or Mayer' s hematoxylin (Carl Roth) for 20 minutes at room temperature. Negative control experiments, including incubation with phosphate buffered saline instead of primary antibody, were done for each antibody. Slides were then photographed with a Keyence BZ9000 microscope (Keyence, Kyoto, Japan) or scanned with a NanoZoomer 2.0-HT Digital slide scanner C9600 (Meyer Instruments, Hamamatsu, Japan) and images were taken with the NDP.view2 software (Meyer Instruments, Hamamatsu, Japan).

A.8 Case Report 1: AAA with Left Common Iliac Artery Occlusion

Tissue was acquired from a 77 year old female patient with an asymptomatic fusiform AAA of 58 mm at the time of operation. The aneurysm had been under surveillance for 9 years from a diameter of 44mm, suggesting a rather slow growth. Additionally, the patient had a complete occlusion of the left common iliac artery, without signs of claudication or leg ischemia on the left side, due to good collateralization. She was operated with an aorto-biiliac graft interposition with a transperitoneal open approach. The patient also had chronic kidney disease (KDIGO III) and smoked until the time of surgery, as well as other co-morbidities including hyperlipidemia and hypertensive disease.

A.9 Case Report 2: AAA with Right Leg Amputation

Tissue was acquired from a 67 year old female with asymptomatic AAA of 51 mm. The patient was under surveillance for 7 years until reaching a surgical threshold. She had undergone

above the knee right leg amputation 7 years prior due to leg ischemia as a result of a thrombosed popliteal aneurysm (PAA). The left leg had been treated with a femoropopliteal bypass due to PAA of 27 mm 6.5 years prior. She had a pronounced cardiovascular risk profile with metabolic syndrome, including hypertension, hyperlipidemia, type II diabetes and obesity, as well as other co-morbidities such as heart insufficiency NYHA II and chronic obstructive pulmonary disease. Additionally she had been a longtime smoker before the major amputation. The patient was operated with a tube graft interposition by an open retroperitoneal approach. Although surgery went well and without complications, the patient never recovered from anesthesia due to a cerebral non-perfusion caused by subarachnoidal hemorrhages due to hypertensive emergency during anesthesia induction.

A.10 Statistical Methods

We used two-way analysis of variance (ANOVA) with Tukey's HSD post-hoc analysis to determine statistical significance for aortic diameter, volume/length, and strain data, as well as both aortic and iliac artery mean and peak velocities. Additionally, we used one-way ANOVA with Tukey's HSD post-hoc analysis to determine statistical significance for day 56 iliac artery strain, mean velocity, diameter. Further, one-way ANOVA with Tukey's HSD post-hoc was also used to evaluate significance for aortic ΔCt gene expression, cell counting, and centerline deviation magnitude data. Centerline deviation direction statistics was performed using MATLAB CircStat Toolbox.[160] All values are reported and plotted as average ± standard deviation.

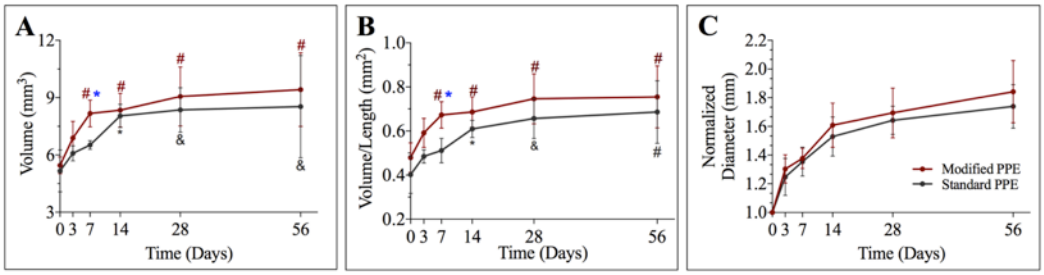

Appendix A Figure 9: Comparison of aortic volume (A), volume/length (B), and normalized diameter (C) changes over 56 days between the standard and modified PPE groups. Both volume and volume/length reveal rapid aneurysm growth over the first seven days post-PPE infusion. Normalized aortic diameter shows steady AAA growth up to day 56. Statistical significance compared with day 0 and defined at $p<0.05$ (*), $p<0.01$ (&), and $p<0.001$ (#). Blue asterisk represents statistical significance between the standard and modified PPE groups at day 7.

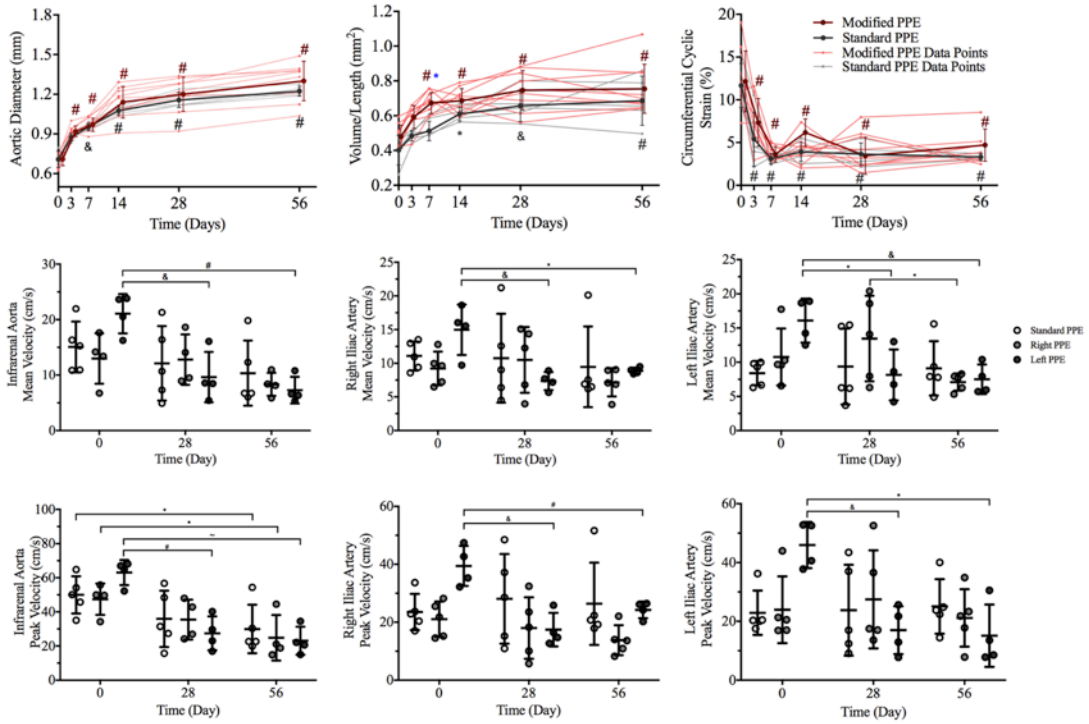

Appendix A Figure 10: Morphological, kinematic, and hemodynamic changes in infrarenal aorta, and left and right iliac arteries due to PPE infusion and partial iliac ligation. Diameter measurements show gradual increase in AAA size up to day 56, with volume/length showing rapid aneurysm expansion in the first seven days. Circumferential cyclic strain measurements reveal rapid decrease in aortic pulsatility post-PPE infusion for all animals. Overall, infrarenal aorta, and modified left and right PPE velocities decrease after surgical AAA induction and partial iliac ligation, respectively by day 56. Statistical significance defined at $p<0.05$ (*), $p<0.01$ (&), and $p<0.001$ (#).

Appendix A Table 1: Summary of iliac artery mean velocities for the standard PPE, as well as modified left and right PPE groups at day 56. Standard PPE group shows slightly greater and more variable mean velocities in the left and right iliac arteries.

	Standard PPE		Left PPE		Right PPE	
Iliac Artery	Left	Right	Left (ligated)	Right (contralateral)	Left (contralateral)	Right (ligated)
Mean Velocity (cm/s)	9.11 ± 3.97	9.46 ± 5.99	7.17 ± 2.10	8.88 ± 0.48	7.51 ± 2.17	7.10 ± 1.26

Appendix A Table 2: Day 28 and 56 centerline deviation results showing magnitude and direction of AAA growth in standard PPE, as well as left and right modified PPE groups.

Day	Measurement	Standard PPE	Left PPE	Right PPE
28	Magnitude (mm)	0.02 ± 0.12	0.11 ± 0.06	0.08 ± 0.22
	Direction (°)	170.2 ± 22.5	189.2 ± 72.6	66.7 ± 24.3
56	Magnitude (mm)	0.04 ± 0.10	0.12 ± 0.25	0.12 ± 0.10
	Direction (°)	354.2 ± 51.7	210.0 ± 30.5	171.3 ± 27.2

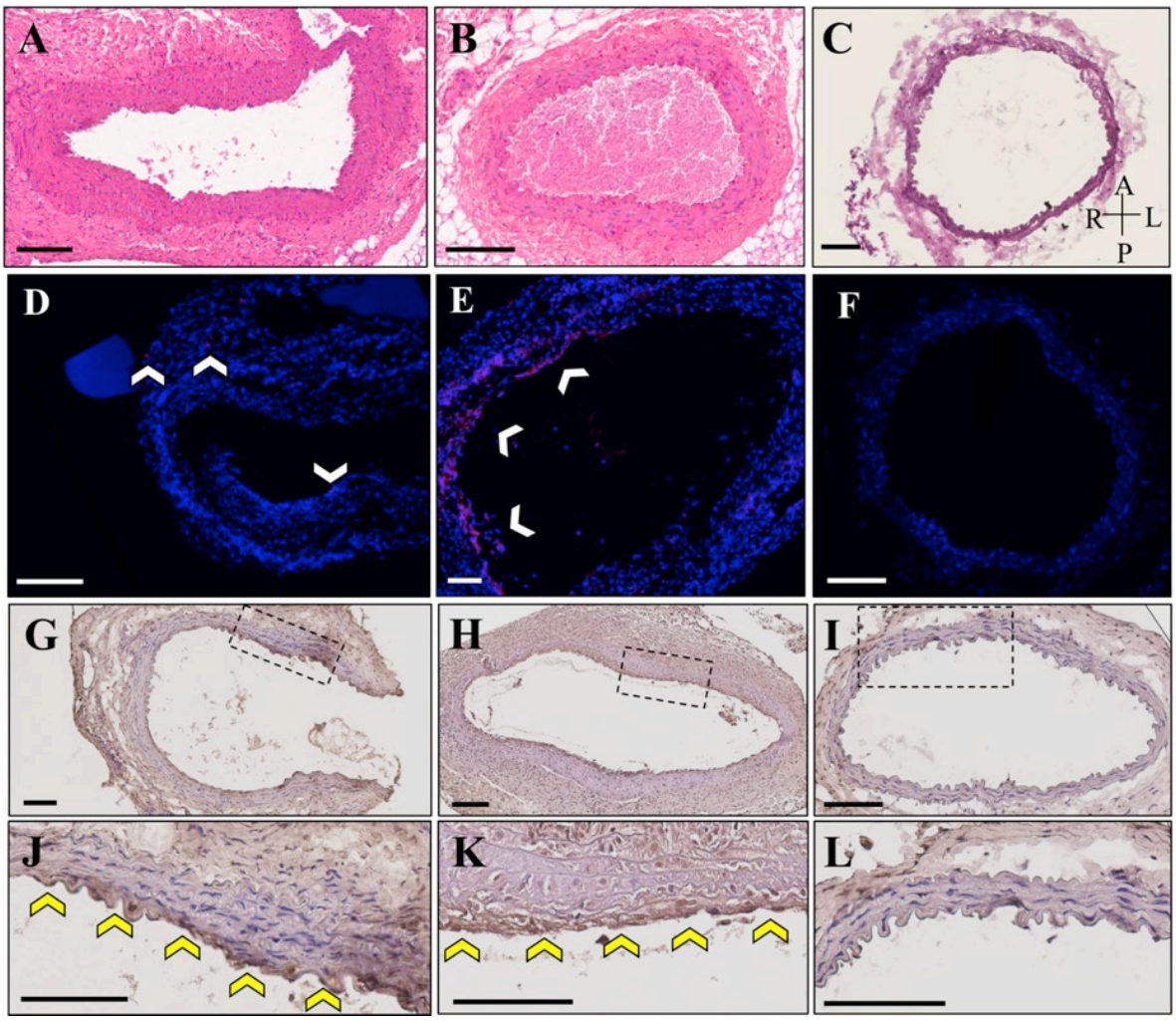

Appendix A Figure 11: Histological and immunohistochemistry analysis of PPE infused aortic tissue. H&E stained standard (A) and modified (B) PPE aortae showed vessel wall thickening compared to control aortae (C). Ki67 staining confirmed cell proliferation (white arrow) in standard (D) and modified (E) aortae compared to control aortae (F). Immunohistochemistry revealed TGFβ1 expression (yellow arrows) in standard (G,J) and modified (H,K) animals compared to control animals (I,L). A: Anterior, P: Posterior, L: Left, R: Right. Scale bar denotes 100 μm.

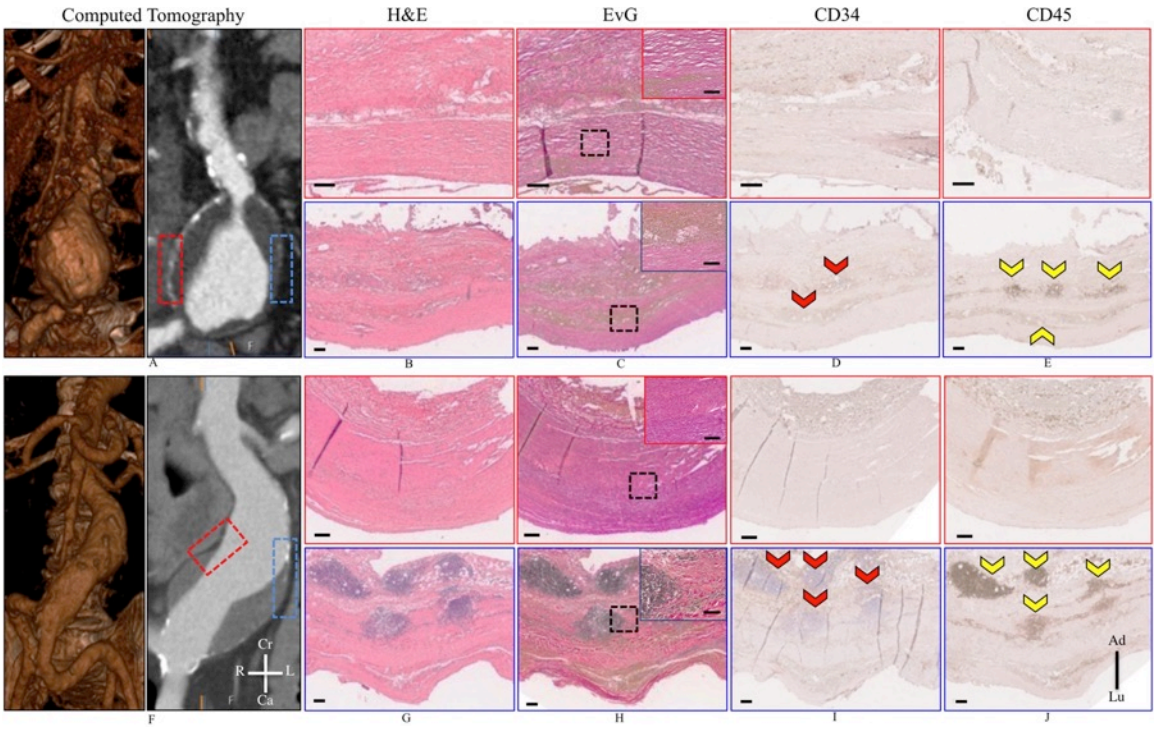

Appendix A Figure 12: Computed tomography imaging of two AAA patients, one with a left common iliac occlusion (A) and one with a right leg amputation (F), reveals asymmetrical aneurysm formation. Closer examination with H&E staining shows signs of increased cellular infiltration on the left side of the AAA in both the modified left (B) and right (G) iliac outflow. EvG staining reveals widespread destruction of elastin laminar units (C,H). High resolution images of elastin destruction are shown in the EvG insets with the location of the inset shown in black dotted boxes. Cellular infiltrate was primarily comprised of inflammatory cells via CD34 (red arrows; D, I) and CD45 (yellow arrows; E, J) immunohistochemistry. Cr: Cranial, Ca: Caudal, L: Left, R: Right, Av: adventitia, Lu: Lumen. Scale bar denotes 200 μm.

APPENDIX B

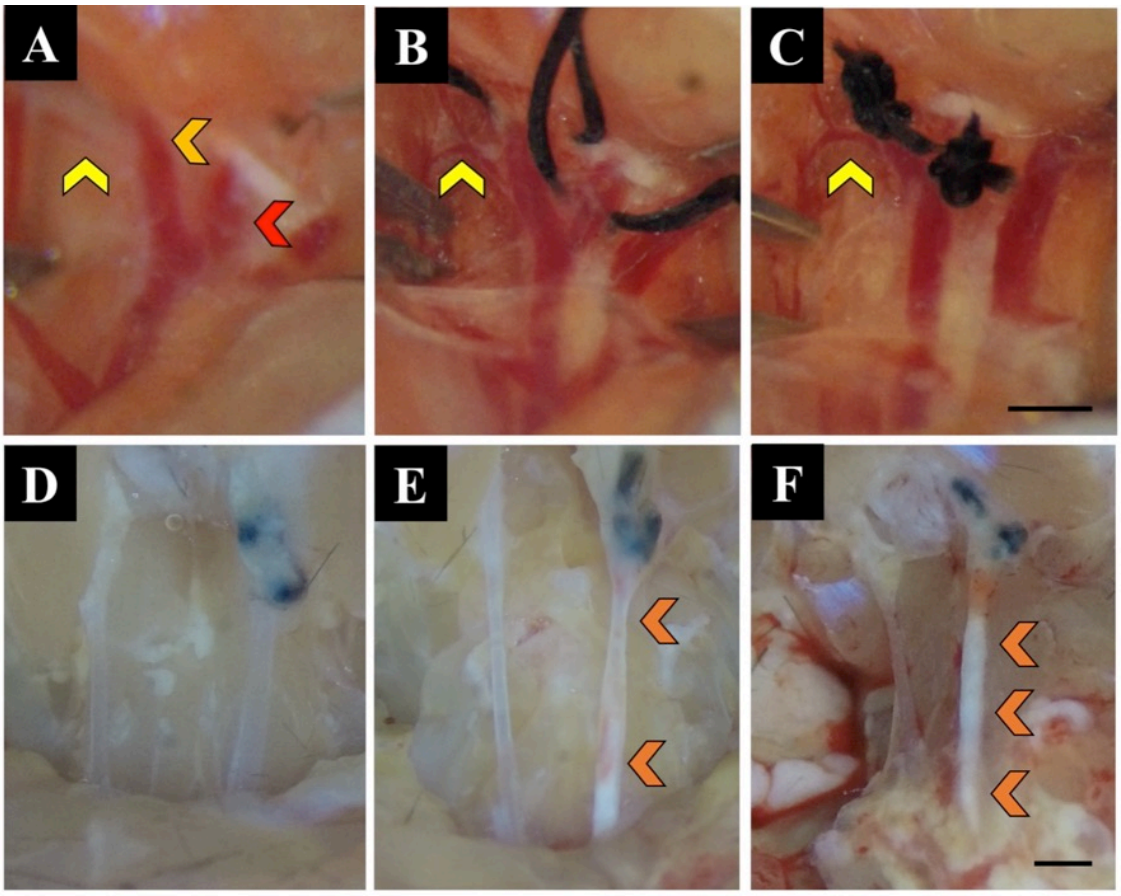

Appendix B Figure 1: Summary of PCL procedure and representative gross images post-PCL. The LCA was first exposed and the internal (red arrow) and external (orange arrow) carotid artery, as well as the occipital (red arrow) and superior thyroid artery (yellow arrow) were identified (A). A 6-0 black braided silk suture was then placed around the internal and occipital carotid arteries, as well as the external carotid artery (B) and tied off to redirect flow into the superior thyroid artery (C). Gross images of the LCA (D-E) revealed robust plaque accumulation as early as day 10 followed by aggressive lipid lesions by day 14. Scale bar: 1mm.

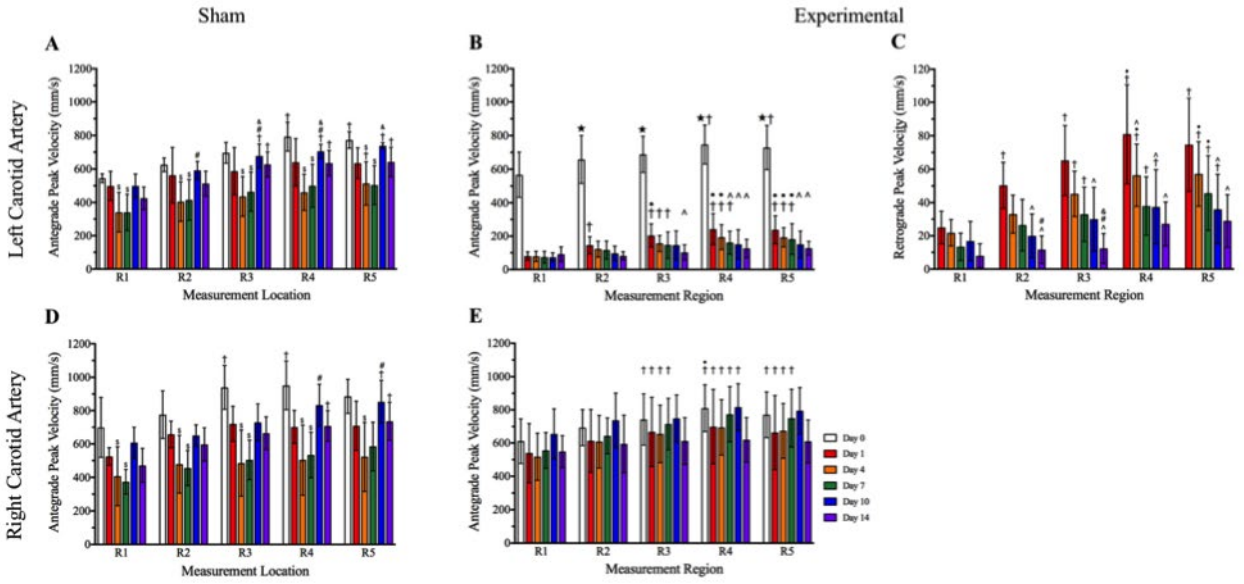

Appendix B Figure 2: Hemodynamic changes in the sham and experimental groups post-PCL. The sham group showed a decrease in LCA and RCA velocities as the mice recover from the surgery. Experimental group peak velocities are comparable to mean velocities that are also shown in Figure 3. Statistical significance determined at $p<0.05$ (★ = significance compared to all other days in same region, † = significance compared to the same day in region 1, • = significance compared to the same day in region 2, ∧ = significance compared to day 1 in the same region, # = significance compared to day 4 in the same region, and & = significance compared to day 7 in the same region).

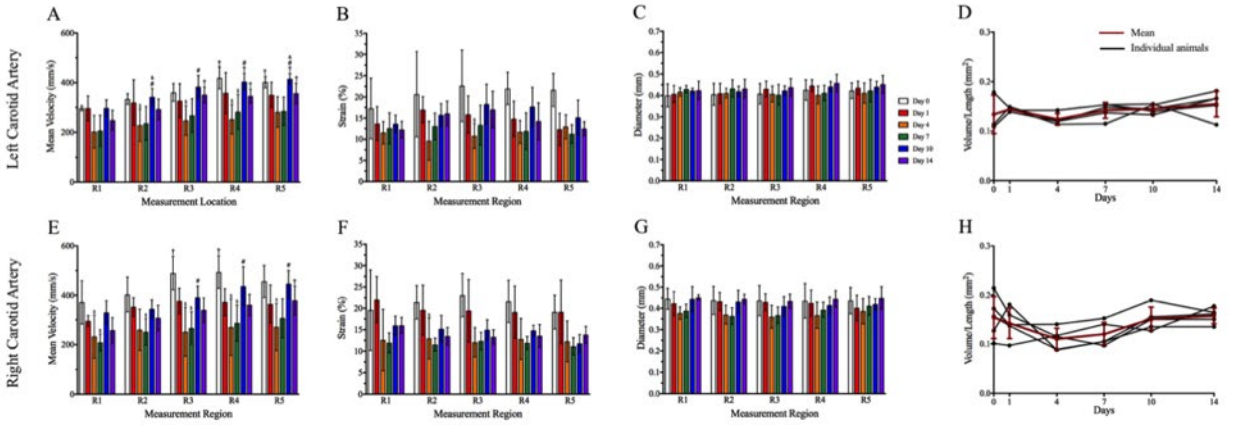

Appendix B Figure 3: Mean velocity, strain, diameter, and volume/length changes in both the LCA and RCA in the sham group. These metrics were fairly consistent when comparing baseline and day 14 data. Statistical significance determined at $p<0.05$ († = significance compared to the same day in region 1, $ = significance compared to day 0 in the same region, ∧ = significance compared to day 1 in the same region, # = significance compared to day 4 in the same region, and & = significance compared to day 7 in the same region).

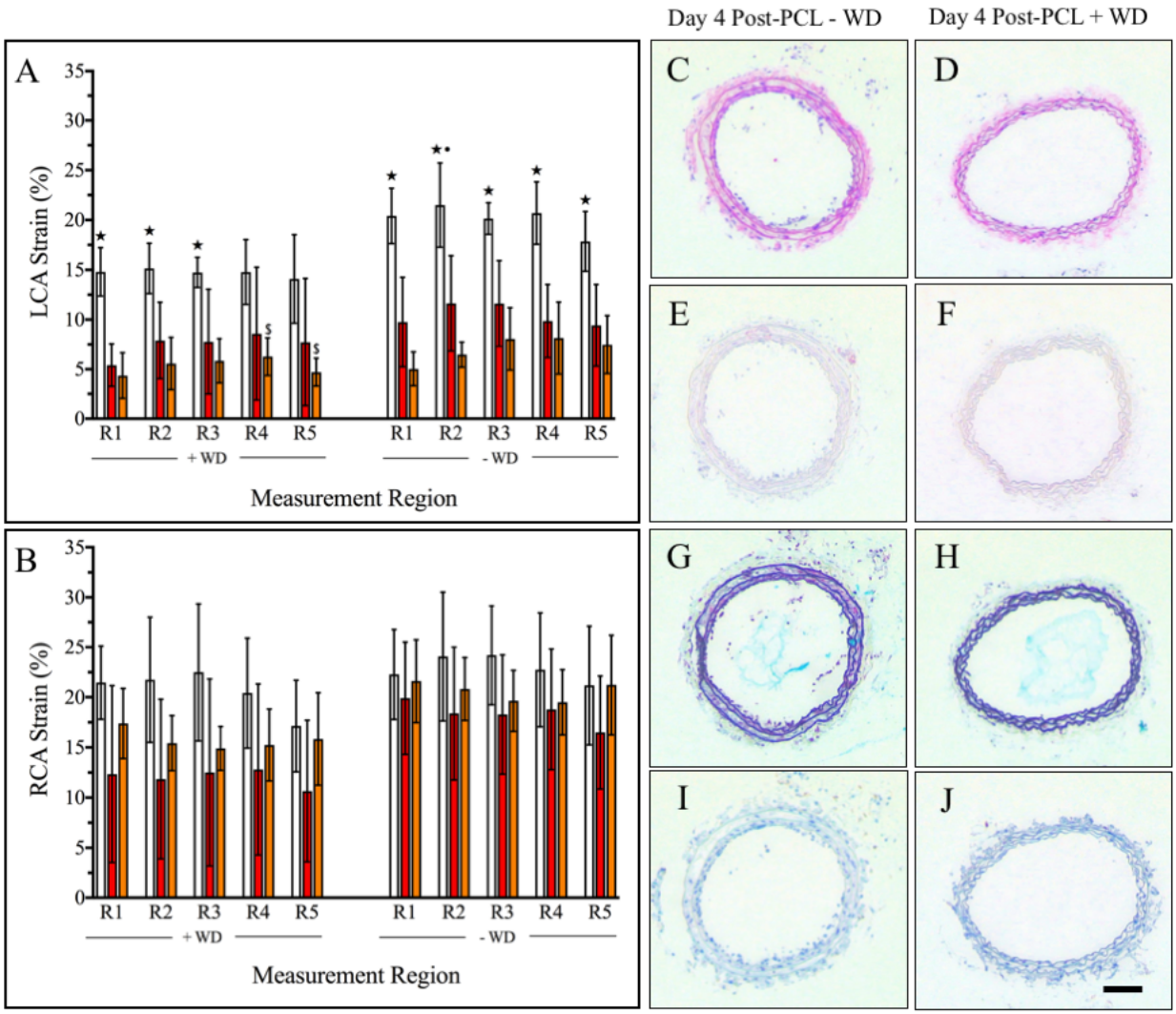

Appendix B Figure 4: Day 4 strain data in the LCA (A) and RCA (B) post-PCL showed comparable values with and without WD feeding. H&E (C-D), ORO (E-F), Movat's pentachrome (G-H) staining, as well as F4/80 immunohistochemistry revealed no signs of vessel stenosis or inflammation. Statistical significance determined at $p<0.05$ (= significance compared to all other days in same region, • = significance compared to the same day in region 2). Scale bar: 100 μm.

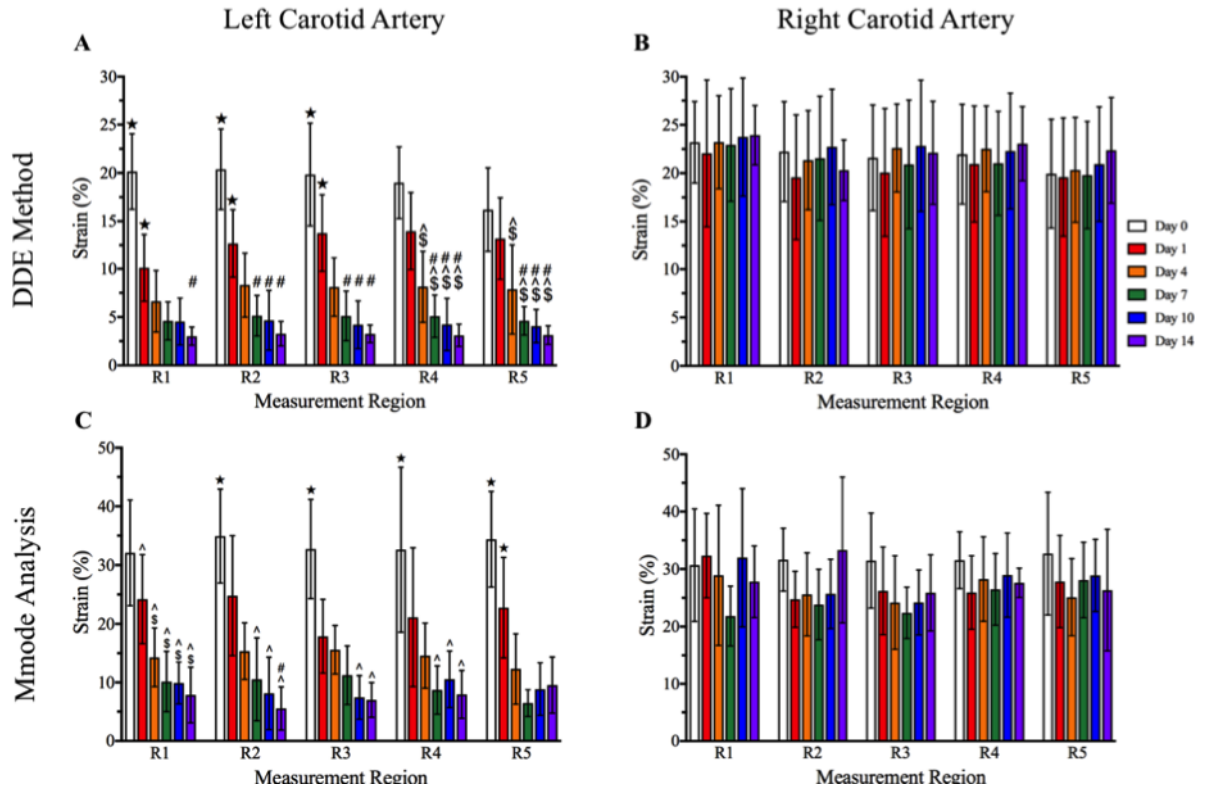

Appendix B Figure 5: Strain comparison between the DDE and conventional MMode analysis for LCA and RCA. The DDE method shows similar trend in the LCA with large decrease in pulsatility between days 0 and 4. Statistical significance determined at $p<0.05$ (★ = significance compared to all other days in same region, $ = significance compared to day 0 in the same region, ∧ = significance compared to day 1 in the same region, and # = significance compared to day 4 in the same region).

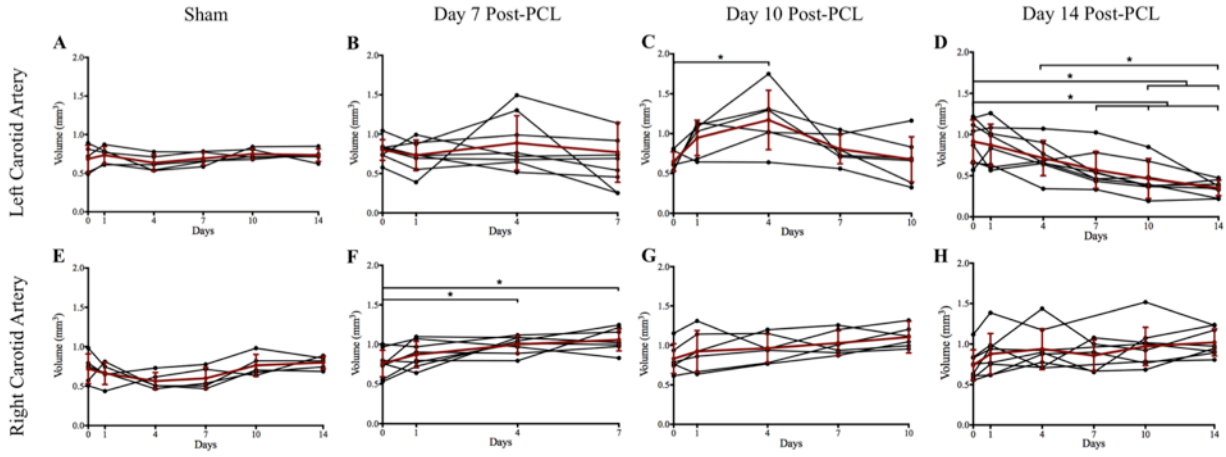

Appendix B Figure 6: Volume changes in the LCA and RCA post-PCL. We observed a decrease in LCA volume after day 7, and a gradual increase in RCA volume throughout the 14 day study in the PCL group. The sham group did not show changes in carotid artery volumes.

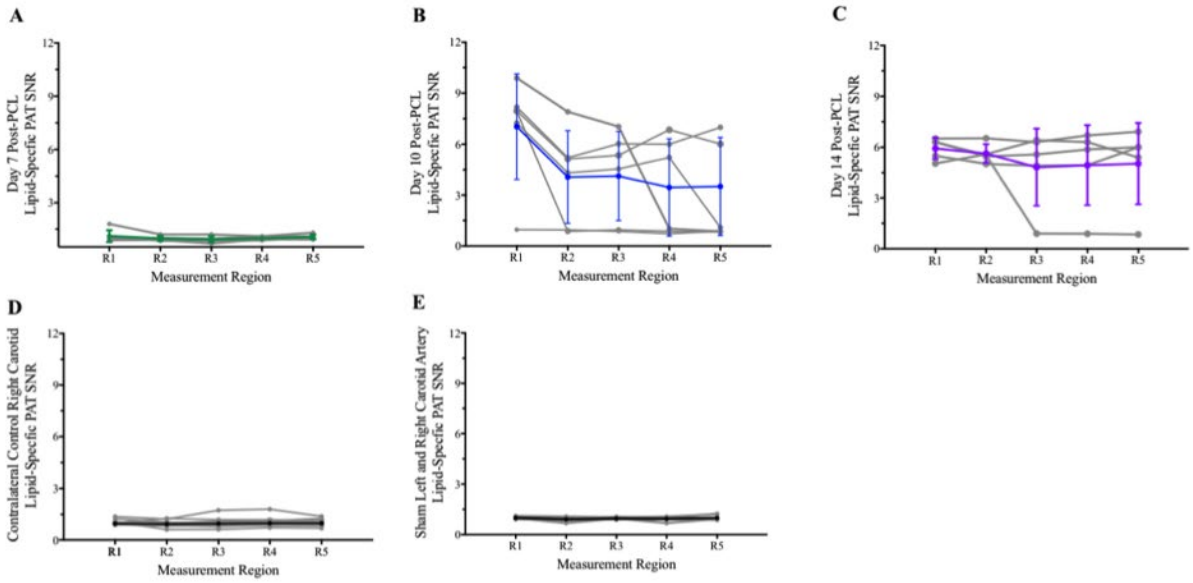

Appendix B Figure 7: Quantitative 1100nm PAT lipid distribution along carotid artery for day 7 (A), 10 (B), 14 (C), RCA (D), and sham carotid arteries (E). Individual animal data points plotted in gray.

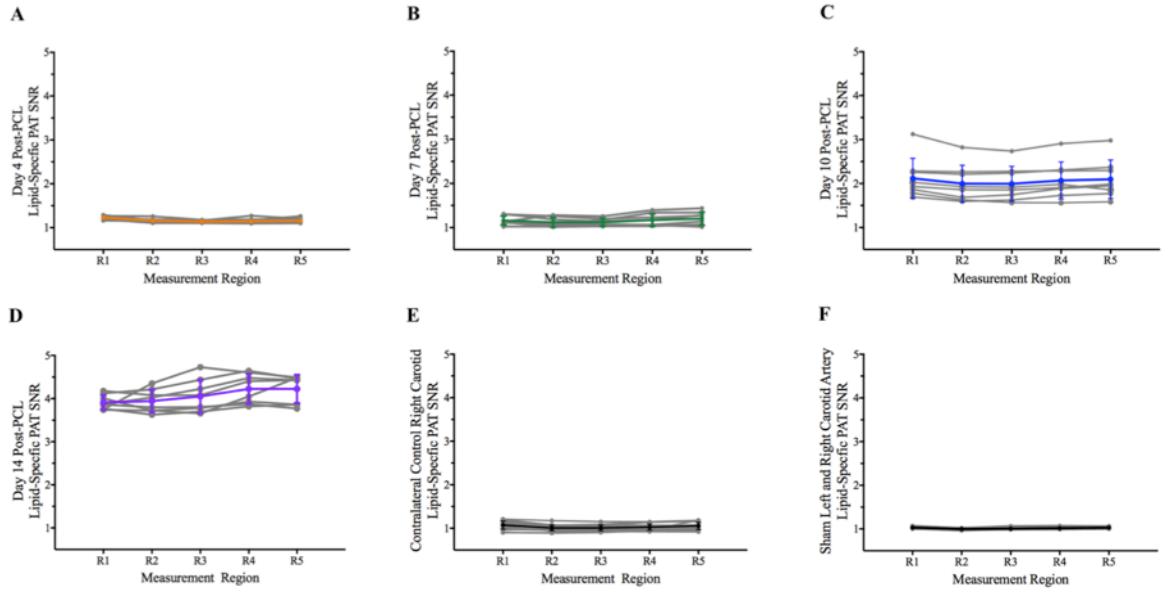

Appendix B Figure 8: Quantitative 1210 nm PAT lipid distribution along carotid artery for day 4 (A), 7 (B), 10 (C), 14 (D), RCA (E), and sham carotid arteries (F). Individual animal data points plotted in gray.

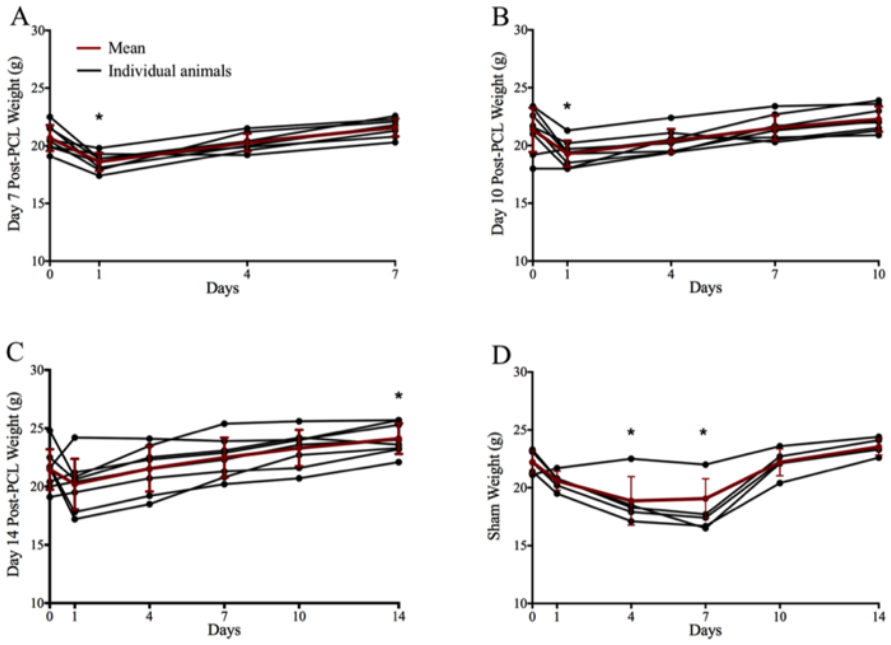

Appendix B Figure 9: Individual mouse weights for day 4, 7, 10, 14 post-PCL groups, as well as the sham group. On average, we observed a decrease in weight after the surgical procedure followed by gradual increase in weight through the course of the study. Statistical significance determined at $p<0.05$ and compared to baseline.

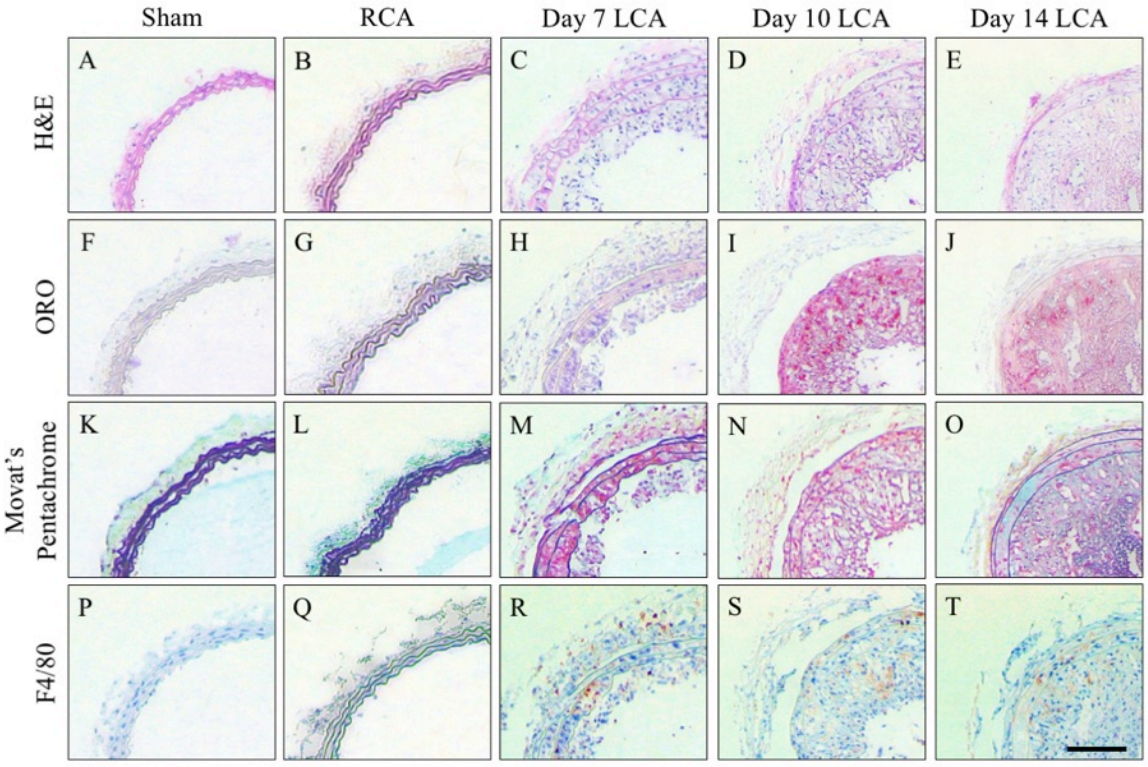

Appendix B Figure 10: Representative magnified H&E (A-D), ORO (E-H), Movat's pentachrome (I-L) staining, as well as F4/80 immunohistochemistry (M-P). Scale bar: 100 μm

REFERENCES

1. Sangha GS, Goergen CJ. 2016. Photoacoustic tomography: applications for atherosclerosis imaging. *Journal of Optics* 18:084005

2. Lin JB, Phillips EH, Riggins TAE, Sangha GS, Chakraborty S, et al. 2015. Imaging of small animal peripheral artery disease models: recent advancements and translational potential. *International journal of molecular sciences* 16:11131-77

3. Sowers T, VanderLaan D, Karpiouk A, Donnelly EM, Smith E, Emelianov S. 2019. Laser threshold and cell damage mechanism for intravascular photoacoustic imaging. *Lasers in surgery and medicine* 51:466-74

4. Iskander-Rizk S, Wu M, Springeling G, van Beusekom H, Mastik F, et al. 2019. In vivo intravascular photoacoustic imaging of plaque lipid in coronary atherosclerosis. *Photoacoustics for Cardiovascular Applications*:115

5. Cao Y, Kole A, Hui J, Sturek M, Cheng J-X. In Vivo Intravascular Photoacoustic Tomography for Depth-Resolved Lipid-Rich Plaque Assessment. *Proc. Clinical and Translational Biophotonics*, *2018*:CW4B. 2: Optical Society of America
6. Lucas AJ. 2000. Atherosclerosis. *Nature* 407:233-41

7. Roger VL, Go AS, Lloyd-Jones DM, Benjamin EJ, Berry JD, et al. 2012. Heart disease and stroke statistics—2012 update a report from the American heart association. *Circulation* 125:e2-e220

8. Beckman JA, Creager MA, Libby P. 2002. Diabetes and atherosclerosis: epidemiology, pathophysiology, and management. *Jama* 287:2570-81

9. Greenland P, Alpert JS, Beller GA, Benjamin EJ, Budoff MJ, et al. 2010. 2010 ACCF/AHA Guideline for Assessment of Cardiovascular Risk in Asymptomatic Adults: A Report of the American College of Cardiology Foundation/American Heart Association Task Force on Practice Guidelines Developed in Collaboration With the American Society of Echocardiography, American Society of Nuclear Cardiology, Society of Atherosclerosis Imaging and Prevention, Society for Cardiovascular Angiography and Interventions, Society of Cardiovascular Computed Tomography, and Society for Cardiovascular Magnetic Resonance. *Journal of the American College of Cardiology* 56:e50-e103

10. Hirsch AT, Criqui MH, Treat-Jacobson D, Regensteiner JG, Creager MA, et al. 2001. Peripheral arterial disease detection, awareness, and treatment in primary care. *Jama* 286:1317-24

11. Stary HC, Chandler AB, Dinsmore RE, Fuster V, Glagov S, et al. 1995. A definition of advanced types of atherosclerotic lesions and a histological classification of atherosclerosis A report from the Committee on Vascular Lesions of the Council on Arteriosclerosis, American Heart Association. *Circulation* 92:1355-74

12. Balch GC, Mithani SK, Simpson JF, Kelley MC. 2005. Accuracy of intraoperative gross examination of surgical margin status in women undergoing partial mastectomy for breast malignancy. *Am Surg* 71:22-7; discussion 7-8

13. Glagov Sa, Zarins C, Giddens DP, Ku DN. 1988. Hemodynamics and atherosclerosis. Insights and perspectives gained from studies of human arteries. *Archives of pathology & laboratory medicine* 112:1018-31

14. Ku DN. 1997. Blood flow in arteries. *Annual Review of Fluid Mechanics* 29:399-434
15. Falk E. 2006. Pathogenesis of Atherosclerosis. *Journal of the American College of Cardiology* 47:C7-C12

16. Naghavi M, Libby P, Falk E, Casscells SW, Litovsky S, et al. 2003. From vulnerable plaque to vulnerable patient a call for new definitions and risk assessment strategies: part I. *Circulation* 108:1664-72

17. Suri JS, Kathuria C, Molinari F. 2010. *Atherosclerosis disease management*. Springer Science & Business Media

18. Armstrong ML, Heistad DD, Marcus ML, Megan MB, Piegors DJ. 1985. Structural and hemodynamic response of peripheral arteries of macaque monkeys to atherogenic diet. *Arteriosclerosis, Thrombosis, and Vascular Biology* 5:336-46

19. Zarins CK, Zatina MA, Giddens DP, Ku DN, Glagov S. 1987. Shear stress regulation of artery lumen diameter in experimental atherogenesis. *Journal of Vascular Surgery* 5:413-20

20. Korshunov VA, Schwartz SM, Berk BC. 2007. Vascular Remodeling Hemodynamic and Biochemical Mechanisms Underlying Glagov's Phenomenon. *Arteriosclerosis, thrombosis, and vascular biology* 27:1722-8

21. Lin JB, Phillips EH, Riggins TE, Sangha GS, Chakraborty S, et al. 2015. Imaging of Small Animal Peripheral Artery Disease Models: Recent Advancements and Translational Potential. *International journal of molecular sciences* 16:11131-77

22. Nissen SE. 2008. Limitations of Computed Tomography Coronary Angiography∗. *Journal of the American College of Cardiology* 52:2145-7

23. Webb A. 2003. *Introduction to biomedical imaging*. Wiley-Interscience

24. Grant EG, Benson CB, Moneta GL, Alexandrov AV, Baker JD, et al. 2003. Carotid Artery Stenosis: Gray-Scale and Doppler US Diagnosis—Society of Radiologists in Ultrasound Consensus Conference1. *Radiology*

25. Macharzina RR, Schmid SF, Beschorner U, Noory E, Rastan A, et al. 2015. Duplex Ultrasound Assessment of Native Stenoses in the Superficial Femoral and Popliteal Arteries A Comparative Study Examining the Influence of Multisegment Lesions. *Journal of Endovascular Therapy* 22:254-60

26. Mintz GS, Nissen SE, Anderson WD, Bailey SR, Erbel R, et al. 2001. American College of Cardiology clinical expert consensus document on standards for acquisition, measurement and reporting of intravascular ultrasound studies (ivus): A report of the american college of cardiology task force on clinical expert consensus documents developed in collaboration with the european society of cardiology endorsed by the society of cardiac angiography and interventions. *Journal of the American College of Cardiology* 37:1478-92

27. Piazza N, Peter de Jaegere MD, Schultz C, Becker AE, Serruys PW, Anderson RH. 2008. Contemporary Reviews in Interventional Cardiology.

28. Nair A, Kuban BD, Tuzcu EM, Schoenhagen P, Nissen SE, Vince DG. 2002. Coronary plaque classification with intravascular ultrasound radiofrequency data analysis. *Circulation* 106:2200-6

29. Lee W. 2013. General principles of carotid Doppler ultrasonography. *Ultrasonography* 33:11-7

30. Collins R, Burch J, Cranny G, Aguiar-Ibáñez R, Craig D, et al. 2007. Duplex ultrasonography, magnetic resonance angiography, and computed tomography angiography for diagnosis and assessment of symptomatic, lower limb peripheral arterial disease: systematic review. *Bmj* 334:1257

31. Feldman MK, Katyal S, Blackwood MS. 2009. US artifacts 1. *Radiographics* 29:1179-89

32. Cheng K-S, Mikhailidis DP, Hamilton G, Seifalian AM. 2002. A review of the carotid and femoral intima-media thickness as an indicator of the presence of peripheral vascular disease and cardiovascular risk factors. *Cardiovascular research* 54:528-38

33. Touboul PJ, Hennerici MG, Meairs S, Adams H, Amarenco P, et al. 2007. Mannheim carotid intima-media thickness consensus (2004–2006). *Cerebrovascular diseases* 23:75-80

34. Briguori C, Anzuini A, Airoldi F, Gimelli G, Nishida T, et al. 2001. Intravascular ultrasound criteria for the assessment of the functional significance of intermediate coronary artery stenoses and comparison with fractional flow reserve. *The American journal of cardiology* 87:136-41

35. Chilcote WA, Modic MT, Pavlicek WA, Little JR, Furlan AJ, et al. 1981. Digital subtraction angiography of the carotid arteries: a comparative study in 100 patients. *Radiology* 139:287-95

36. Buonocore E, Meaney TF, Borkowski GP, Pavlicek W, Gallagher J. 1981. Digital subtraction angiography of the abdominal aorta and renal arteries. Comparison with conventional aortography. *Radiology* 139:281-6

37. Tendera M, Aboyans V, Bartelink M-L, Baumgartner I, Clément D, et al. 2011. ESC Guidelines on the diagnosis and treatment of peripheral artery diseases. *European heart journal* 32:2851-906

38. Hirsch AT, Haskal ZJ, Hertzer NR, Bakal CW, Creager MA, et al. 2006. ACC/AHA 2005 Practice Guidelines for the management of patients with peripheral arterial disease (lower extremity, renal, mesenteric, and abdominal aortic): a collaborative report from the American Association for Vascular Surgery/Society for Vascular Surgery, Society for Cardiovascular Angiography and Interventions, Society for Vascular Medicine and Biology, Society of Interventional Radiology, and the ACC/AHA Task Force on Practice Guidelines (Writing Committee to Develop Guidelines for the Management of Patients With Peripheral Arterial Disease): endorsed by the American Association of Cardiovascular and Pulmonary Rehabilitation; National Heart, Lung, and Blood Institute; Society for Vascular Nursing; TransAtlantic Inter-Society Consensus; and Vascular Disease Foundation. *Circulation* 113:e463-654

39. Cosottini M, Pingitore A, Puglioli M, Michelassi MC, Lupi G, et al. 2003. Contrast-enhanced three-dimensional magnetic resonance angiography of atherosclerotic internal carotid stenosis as the noninvasive imaging modality in revascularization decision making. *Stroke* 34:660-4

40. Yorgun H, Canpolat U, Aytemir K, Hazırolan T, Sunman H, et al. 2013. Prognosis of patients with mild–moderate coronary artery stenosis detected by coronary computed tomography angiography. *International journal of cardiology* 168:1195-200

41. Ruehm SG, Goyen M, Barkhausen J, Kröger K, Bosk S, et al. 2001. Rapid magnetic resonance angiography for detection of atherosclerosis. *The Lancet* 357:1086-91

42. Met R, Bipat S, Legemate DA, Reekers JA, Koelemay MJW. 2009. Diagnostic performance of computed tomography angiography in peripheral arterial disease: a systematic review and meta-analysis. *Jama* 301:415-24

43. Laswed T, Rizzo E, Guntern D, Doenz F, Denys A, et al. 2008. Assessment of occlusive arterial disease of abdominal aorta and lower extremities arteries: value of multidetector CT angiography using an adaptive acquisition method. *European radiology* 18:263-72

44. Schernthaner R, Stadler A, Lomoschitz F, Weber M, Fleischmann D, et al. 2008. Multidetector CT angiography in the assessment of peripheral arterial occlusive disease: accuracy in detecting the severity, number, and length of stenoses. *European radiology* 18:665-71

45. Brenner DJ, Hall EJ. 2007. Computed tomography—an increasing source of radiation exposure. *New England Journal of Medicine* 357:2277-84

46. Hausleiter J, Meyer T, Hadamitzky M, Huber E, Zankl M, et al. 2006. Radiation dose estimates from cardiac multislice computed tomography in daily practice impact of different scanning protocols on effective dose estimates. *Circulation* 113:1305-10

47. Einstein AJ, Henzlova MJ, Rajagopalan S. 2007. Estimating risk of cancer associated with radiation exposure from 64-slice computed tomography coronary angiography. *Jama* 298:317-23

48. Walker LJ, Ismail A, McMeekin W, Lambert D, Mendelow AD, Birchall D. 2002. Computed tomography angiography for the evaluation of carotid atherosclerotic plaque correlation with histopathology of endarterectomy specimens. *Stroke* 33:977-81

49. Visser K, Hunink MGM. 2000. Peripheral Arterial Disease: Gadolinium-enhanced MR Angiography versus Color-guided Duplex US—A Meta-analysis1. *Radiology*

50. Poon E, Yucel EK, Pagan-Marin H, Kayne H. 1997. Iliac artery stenosis measurements: comparison of two-dimensional time-of-flight and three-dimensional dynamic gadolinium-enhanced MR angiography. *AJR. American journal of roentgenology* 169:1139-44

51. Ho KY, De Haan MW, Kessels AG, Kitslaar PJ, Van Engelshoven JM. 1998. Peripheral vascular tree stenoses: detection with subtracted and nonsubtracted MR angiography. *Radiology* 206:673-81

52. Nelemans PJ, Leiner T, de Vet HCW, van Engelshoven JMA. 2000. Peripheral Arterial Disease: Meta-analysis of the Diagnostic Performance of MR Angiography 1. *Radiology* 217:105-14

53. Patel MR, Klufas RA, Kim D, Edelman RR, Kent KC. 1994. MR angiography of the carotid bifurcation: artifacts and limitations. *AJR. American journal of roentgenology* 162:1431-7

54. Nederkoorn PJ, van der Graaf Y, Eikelboom BC, van der Lugt A, Bartels LW, Mali WPTM. 2002. Time-of-flight MR angiography of carotid artery stenosis: does a flow void represent severe stenosis? *American journal of neuroradiology* 23:1779-84

55. Baumgartner RW, Mattle HP, Aaslid R. 1995. Transcranial color-coded duplex sonography, magnetic resonance angiography, and computed tomography angiography: Methods, applications, advantages, and limitations. *Journal of clinical ultrasound* 23:89-111

56. Kuo PH, Kanal E, Abu-Alfa AK, Cowper SE. 2007. Gadolinium-based MR contrast agents and nephrogenic systemic fibrosis 1. *Radiology* 242:647-9

57. Grobner T, Prischl FC. 2007. Gadolinium and nephrogenic systemic fibrosis. *Kidney international* 72:260-4

58. Thakral C, Alhariri J, Abraham JL. 2007. Long-term retention of gadolinium in tissues from nephrogenic systemic fibrosis patient after multiple gadolinium-enhanced MRI scans: case report and implications. *Contrast media & molecular imaging* 2:199-205

59. Károlyi M, Seifarth H, Liew G, Schlett CL, Maurovich-Horvat P, et al. 2013. Classification of coronary atherosclerotic plaques ex vivo with T1, T2, and ultrashort echo time CMR. *JACC: Cardiovascular Imaging* 6:466-74

60. Trivedi RA, U-King-Im J, Graves MJ, Horsley J, Goddard M, et al. 2004. Multi-sequence in vivo MRI can quantify fibrous cap and lipid core components in human carotid atherosclerotic plaques. *European journal of vascular and endovascular surgery* 28:207-13

61. LaMuraglia GM, Southern JF, Fuster V, Kantor HL. 1996. Magnetic resonance images lipid, fibrous, calcified, hemorrhagic, and thrombotic components of human atherosclerosis in vivo. *Circulation* 94:932-8

62. Hatsukami TS, Ross R, Polissar NL, Yuan C. 2000. Visualization of fibrous cap thickness and rupture in human atherosclerotic carotid plaque in vivo with high-resolution magnetic resonance imaging. *Circulation* 102:959-64

63. Betzig E, Patterson GH, Sougrat R, Lindwasser OW, Olenych S, et al. 2006. Imaging intracellular fluorescent proteins at nanometer resolution. *Science* 313:1642-5

64. Stephens DJ, Allan VJ. 2003. Light microscopy techniques for live cell imaging. *Science* 300:82-6

65. Sun Y, Sun Y, Stephens D, Xie H, Phipps J, et al. 2011. Dynamic tissue analysis using time-and wavelength-resolved fluorescence spectroscopy for atherosclerosis diagnosis. *Optics express* 19:3890-901

66. Calfon MA, Vinegoni C, Ntziachristos V, Jaffer FA. 2010. Intravascular near-infrared fluorescence molecular imaging of atherosclerosis: toward coronary arterial visualization of biologically high-risk plaques. *Journal of biomedical optics* 15:011107--6

67. Verbunt RJAM, Fitzmaurice MA, Kramer JR, Ratliff NB, Kittrell C, et al. 1992. Characterization of ultraviolet laser-induced autofluorescence of ceroid deposits and other structures in atherosclerotic plaques as a potential diagnostic for laser angiosurgery. *American heart journal* 123:208-16

68. Fitzmaurice M, Bordagaray JO, Engelmann GL, Richards-Kortum R, Kolubayev T, et al. 1989. Argon ion laser-excited autofluorescence in normal and atherosclerotic aorta and coronary arteries: morphologic studies. *American heart journal* 118:1028-38

69. Goergen CJ, Radhakrishnan H, Sakadžić S, Mandeville ET, Lo EH, et al. 2012. Optical coherence tractography using intrinsic contrast. *Optics letters* 37:3882-4

70. Yabushita H, Bouma BE, Houser SL, Aretz HT, Jang I-K, et al. 2002. Characterization of human atherosclerosis by optical coherence tomography. *Circulation* 106:1640-5

71. Li BH, Leung ASO, Soong A, Munding CE, Lee H, et al. 2013. Hybrid intravascular ultrasound and optical coherence tomography catheter for imaging of coronary atherosclerosis. *Catheterization and Cardiovascular Interventions* 81:494-507

72. Jang I-K, Bouma BE, Kang D-H, Park S-J, Park S-W, et al. 2002. Visualization of coronary atherosclerotic plaques in patients using optical coherence tomography: comparison with intravascular ultrasound. *Journal of the American College of Cardiology* 39:604-9

73. Doras C, Taupier G, Barsella A, Mager L, Boeglin A, et al. 2011. Polarization state studies in second harmonic generation signals to trace atherosclerosis lesions. *Optics express* 19:15062-8

74. Wang H-W, Le TT, Cheng J-X. 2008. Label-free imaging of arterial cells and extracellular matrix using a multimodal CARS microscope. *Optics communications* 281:1813-22

75. Kim S-H, Lee E-S, Lee JY, Lee ES, Lee B-S, et al. 2010. Multiplex coherent anti-Stokes Raman spectroscopy images intact atheromatous lesions and concomitantly identifies distinct chemical profiles of atherosclerotic lipids. *Circulation research* 106:1332-41

76. Matthäus C, Dochow S, Bergner G, Lattermann A, Romeike BFM, et al. 2012. In vivo characterization of atherosclerotic plaque depositions by Raman-probe spectroscopy and in vitro coherent anti-stokes Raman scattering microscopic imaging on a rabbit model. *Analytical chemistry* 84:7845-51

77. Vasan RS. 2006. Biomarkers of cardiovascular disease molecular basis and practical considerations. *Circulation* 113:2335-62

78. van der Wal AC, Becker AE, Van der Loos CM, Das PK. 1994. Site of intimal rupture or erosion of thrombosed coronary atherosclerotic plaques is characterized by an inflammatory process irrespective of the dominant plaque morphology. *Circulation* 89:36-44

79. Mermel LA, Allon M, Bouza E, Craven DE, Flynn P, et al. 2009. Clinical practice guidelines for the diagnosis and management of intravascular catheter-related infection: 2009 Update by the Infectious Diseases Society of America. *Clinical infectious diseases* 49:1-45

80. Wang P, Wang HW, Sturek M, Cheng JX. 2012. Bond-selective imaging of deep tissue through the optical window between 1600 and 1850 nm. *Journal of biophotonics* 5:25-32

81. Xu M, Wang LV. 2006. Photoacoustic imaging in biomedicine. *Review of scientific instruments* 77:041101

82. Xia J, Yao J, Wang LV. 2014. Photoacoustic tomography: principles and advances. *Electromagnetic waves (Cambridge, Mass.)* 147:1

83. Luke GP, Yeager D, Emelianov SY. 2012. Biomedical applications of photoacoustic imaging with exogenous contrast agents. *Annals of biomedical engineering* 40:422-37

84. Zhao Q, Ji L, Jiang T. 2007. Improving depth resolution of diffuse optical tomography with a layer-based sigmoid adjustment method. *Optics express* 15:4018-29

85. Kruger RA, Lam RB, Reinecke DR, Del Rio SP, Doyle RP. 2010. Photoacoustic angiography of the breast. *Medical physics* 37:6096-100

86. Ku G, Wang LV. 2005. Deeply penetrating photoacoustic tomography in biological tissues enhanced with an optical contrast agent. *Optics letters* 30:507-9

87. Kim C, Erpelding TN, Jankovic L, Pashley MD, Wang LV. 2010. Deeply penetrating in vivo photoacoustic imaging using a clinical ultrasound array system. *Biomedical optics express* 1:278-84

88. Rajian JR, Li R, Wang P, Cheng J-X. 2013. Vibrational photoacoustic tomography: Chemical imaging beyond the ballistic regime. *The journal of physical chemistry letters* 4:3211-5

89. Li R, Slipchenko MN, Wang P, Cheng J-X. 2013. Compact high power barium nitrite crystal-based Raman laser at 1197 nm for photoacoustic imaging of fat. *Journal of biomedical optics* 18:040502-

90. Beard PC, Mills TN. 1997. Characterization of post mortem arterial tissue using time-resolved photoacoustic spectroscopy at 436, 461 and 532 nm. *Physics in medicine and biology* 42:177

91. Allen TJ, Beard PC. Photoacoustic characterisation of vascular tissue at NIR wavelengths. *Proc. SPIE BiOS: Biomedical Optics*, *2009*:71770A-A-9: International Society for Optics and Photonics

92. Wang P, Rajian JR, Cheng J-X. 2013. Spectroscopic imaging of deep tissue through photoacoustic detection of molecular vibration. *The journal of physical chemistry letters* 4:2177-85

93. Qin H, Zhou T, Yang S, Chen Q, Xing D. 2013. Gadolinium (III)-gold nanorods for MRI and photoacoustic imaging dual-modality detection of macrophages in atherosclerotic inflammation. *Nanomedicine* 8:1611-24

94. Ma T, Zhou B, Hsiai TK, Shung KK. 2015. A Review of Intravascular Ultrasound–Based Multimodal Intravascular Imaging The Synergistic Approach to Characterizing Vulnerable Plaques. *Ultrasonic Imaging*:0161734615604829

95. Zhang X, Zhang HF, Jiao S. 2012. Optical coherence photoacoustic microscopy: accomplishing optical coherence tomography and photoacoustic microscopy with a single light source. *Journal of biomedical optics* 17:0305021-3

96. Zhang EZ, Laufer J, Považay B, Alex A, Hofer B, et al. Multimodal simultaneous photoacoustic tomography, optical resolution microscopy, and OCT system. *Proc. BiOS*, *2010*:75640U-U-7: International Society for Optics and Photonics

97. Song W, Wei Q, Liu W, Liu T, Yi J, et al. 2014. A combined method to quantify the retinal metabolic rate of oxygen using photoacoustic ophthalmoscopy and optical coherence tomography. *Scientific reports* 4:6525

98. Wang B, Su JL, Amirian J, Litovsky SH, Smalling R, Emelianov S. 2010. Detection of lipid in atherosclerotic vessels using ultrasound-guided spectroscopic intravascular photoacoustic imaging. *Optics express* 18:4889-97

99. Wang B, Karpiouk A, Yeager D, Amirian J, Litovsky S, et al. 2012. In vivo intravascular ultrasound-guided photoacoustic imaging of lipid in plaques using an animal model of atherosclerosis. *Ultrasound in medicine & biology* 38:2098-103

100. Wang B, Karpiouk A, Yeager D, Amirian J, Litovsky S, et al. 2012. Intravascular photoacoustic imaging of lipid in atherosclerotic plaques in the presence of luminal blood. *Optics letters* 37:1244-6

101. Jansen K, Van Der Steen AFW, van Beusekom HMM, Oosterhuis JW, van Soest G. 2011. Intravascular photoacoustic imaging of human coronary atherosclerosis. *Optics letters* 36:597-9

102. Sethuraman S, Amirian JH, Litovsky SH, Smalling RW, Emelianov SY. 2008. Spectroscopic intravascular photoacoustic imaging to differentiate atherosclerotic plaques. *Optics express* 16:3362-7

103. Sethuraman S, Amirian JH, Litovsky SH, Smalling RW, Emelianov SY. 2007. Ex vivo characterization of atherosclerosis using intravascular photoacoustic imaging. *Optics express* 15:16657-66

104. Wang H-W, Chai N, Wang P, Hu S, Dou W, et al. 2011. Label-free bond-selective imaging by listening to vibrationally excited molecules. *Physical review letters* 106:238106

105. Wu M, Jansen K, van der Steen AFW, van Soest G. 2015. Specific imaging of atherosclerotic plaque lipids with two-wavelength intravascular photoacoustics. *Biomedical optics express* 6:3276-86

106. Rouleau L, Berti R, Ng VWK, Matteau-Pelletier C, Lam T, et al. 2013. VCAM-1-targeting gold nanoshell probe for photoacoustic imaging of atherosclerotic plaque in mice. *Contrast media & molecular imaging* 8:27-39

107. Ha S, Carson A, Agarwal A, Kotov NA, Kim K. 2011. Detection and monitoring of the multiple inflammatory responses by photoacoustic molecular imaging using selectively targeted gold nanorods. *Biomedical optics express* 2:645-57

108. Ha S, Kim JS, Tripathy S, Carson A, Grata M, et al. Simultaneous photoacoustic detection of multiple inflammatory biomarkers using bioconjugated gold nanorods as selective targeting agents. *Proc. Ultrasonics Symposium (IUS), 2010 IEEE*, *2010*:499-502: IEEE

109. Hwang S-J, Ballantyne CM, Sharrett AR, Smith LC, Davis CE, et al. 1997. Circulating adhesion molecules VCAM-1, ICAM-1, and E-selectin in carotid atherosclerosis and incident coronary heart disease cases the atherosclerosis risk in communities (ARIC) study. *Circulation* 96:4219-25

110. Yeager D, Karpiouk A, Wang B, Amirian J, Sokolov K, et al. 2012. Intravascular photoacoustic imaging of exogenously labeled atherosclerotic plaque through luminal blood. *Journal of biomedical optics* 17:106016-

111. Wang B, Joshi P, Sapozhnikova V, Amirian J, Litovsky SH, et al. Intravascular photoacoustic imaging of macrophages using molecularly targeted gold nanoparticles. *Proc. BiOS*, *2010*:75640A-A-7: International Society for Optics and Photonics

112. Wang B, Yantsen E, Larson T, Karpiouk AB, Sethuraman S, et al. 2008. Plasmonic intravascular photoacoustic imaging for detection of macrophages in atherosclerotic plaques. *Nano Letters* 9:2212-7

113. Connor EE, Mwamuka J, Gole A, Murphy CJ, Wyatt MD. 2005. Gold nanoparticles are taken up by human cells but do not cause acute cytotoxicity. *Small* 1:325-7

114. Shashkov EV, Everts M, Galanzha EI, Zharov VP. 2008. Quantum dots as multimodal photoacoustic and photothermal contrast agents. *Nano letters* 8:3953-8

115. Jayagopal A, Su YR, Blakemore JL, Linton MF, Fazio S, Haselton FR. 2009. Quantum dot mediated imaging of atherosclerosis. *Nanotechnology* 20:165102

116. ApoE CARAH. 2000. Atherosclerosis and Lipoproteins.

117. Jayagopal A, Russ PK, Haselton FR. 2007. Surface engineering of quantum dots for in vivo vascular imaging. *Bioconjugate chemistry* 18:1424-33

118. Michalet X, Pinaud FF, Bentolila LA, Tsay JM, Doose S, et al. 2005. Quantum dots for live cells, in vivo imaging, and diagnostics. *science* 307:538-44

119. Choi HS, Liu W, Misra P, Tanaka E, Zimmer JP, et al. 2007. Renal clearance of quantum dots. *Nature biotechnology* 25:1165-70

120. Hardman R. 2006. A toxicologic review of quantum dots: toxicity depends on physicochemical and environmental factors. *Environmental health perspectives*:165-72

121. Tedgui A, Mallat Z. 2006. Cytokines in atherosclerosis: pathogenic and regulatory pathways. *Physiological reviews* 86:515-81

122. Levi J, Kothapalli SR, Ma T-J, Hartman K, Khuri-Yakub BT, Gambhir SS. 2010. Design, synthesis, and imaging of an activatable photoacoustic probe. *Journal of the American Chemical Society* 132:11264-9

123. Razansky D, Harlaar NJ, Hillebrands J-L, Taruttis A, Herzog E, et al. Multispectral optoacoustic tomography resolves smart probe activation in vulnerable plaques. *Proc. SPIE BiOS*, *2011*:789905--6: International Society for Optics and Photonics

124. Zhang R, Pan D, Cai X, Yang X, Senpan A, et al. 2015. αvβ3-targeted copper nanoparticles incorporating an Sn 2 lipase-labile fumagillin prodrug for photoacoustic neovascular imaging and treatment.

125. Zerda Adl, Liu Z, Bodapati S, Teed R, Vaithilingam S, et al. 2010. Ultrahigh sensitivity carbon nanotube agents for photoacoustic molecular imaging in living mice. *Nano letters* 10:2168-72

126. Pan D, Caruthers SD, Senpan A, Yalaz C, Stacy AJ, et al. 2011. Synthesis of NanoQ, a copper-based contrast agent for high-resolution magnetic resonance imaging characterization of human thrombus. *Journal of the American Chemical Society* 133:9168-71

127. Zhang R, Pan D, Cai X, Yang X, Senpan A, et al. 2015. αvβ3-targeted copper nanoparticles incorporating an Sn 2 lipase-labile fumagillin prodrug for photoacoustic neovascular imaging and treatment. *Theranostics* 5:124

128. Lewinski N, Colvin V, Drezek R. 2008. Cytotoxicity of nanoparticles. *small* 4:26-49

129. Altınogˇlu EI, Russin TJ, Kaiser JM, Barth BM, Eklund PC, et al. 2008. Near-infrared emitting fluorophore-doped calcium phosphate nanoparticles for in vivo imaging of human breast cancer. *Acs Nano* 2:2075-84

130. Kim G, Huang S-W, Day KC, O'Donnell M, Agayan RR, et al. 2007. Indocyanine-green-embedded PEBBLEs as a contrast agent for photoacoustic imaging. *Journal of biomedical optics* 12:044020--8

131. Singh MKA, Steenbergen W, Manohar S. 2016. Handheld Probe-Based Dual Mode Ultrasound/Photoacoustics for Biomedical Imaging. In *Frontiers in Biophotonics for Translational Medicine*:209-47: Springer. Number of 209-47 pp.

132. Sheu Y-L, Chou C-Y, Hsieh B-Y, Li P-C. 2011. Image reconstruction in intravascular photoacoustic imaging. *Ultrasonics, Ferroelectrics, and Frequency Control, IEEE Transactions on* 58:2067-77

133. Sun Z, Han D, Wang J. 2015. Review of Image Reconstruction for Intravascular Photoacoustic Imaging. *Opto-Electronic Engineering* 3:004

134. Cao Y, Hui J, Kole A, Wang P, Yu Q, et al. 2016. High-sensitivity intravascular photoacoustic imaging of lipid–laden plaque with a collinear catheter design. *Scientific Reports* 6

135. Karpiouk AB, Wang B, Emelianov SY. 2010. Development of a catheter for combined intravascular ultrasound and photoacoustic imaging. *Review of Scientific Instruments* 81:014901

136. Bai X, Gong X, Hau W, Lin R, Zheng J, et al. 2014. Intravascular optical-resolution photoacoustic tomography with a 1.1 mm diameter catheter. *PloS one* 9:e92463

137. Wang LV, Hu S. 2012. Photoacoustic tomography: in vivo imaging from organelles to organs. *Science* 335:1458-62

138. America LIo. 2014. American National Standard for Safe Use of Lasers.

139. America TLIo. 2005 Safe Use of Lasers in Health Care. ANSI Z136.3

140. Sampson UKA, Norman PE, Fowkes FGR, Aboyans V, Song Y, et al. 2014. Estimation of global and regional incidence and prevalence of abdominal aortic aneurysms 1990 to 2010. *Global Heart* 9:159-70

141. Sampson UKA, Norman PE, Fowkes FGR, Aboyans V, Song Y, et al. 2014. Global and regional burden of aortic dissection and aneurysms: mortality trends in 21 world regions, 1990 to 2010. *Global Heart* 9:171-80. e10

142. Vardulaki KA, Prevost TC, Walker NM, Day NE, Wilmink ABM, et al. 1999. Incidence among men of asymptomatic abdominal aortic aneurysms: estimates from 500 screen detected cases. *Journal of medical screening* 6:50-4

143. Wassef M, Baxter BT, Chisholm RL, Dalman RL, Fillinger MF, et al. 2001. Pathogenesis of abdominal aortic aneurysms: a multidisciplinary research program supported by the National Heart, Lung, and Blood Institute. *Journal of vascular surgery* 34:730-8

144. Vollmar JF, Pauschinger P, Paes E, Henze E, Friesch A. 1989. Aortic aneurysms as late sequelae of above-knee amputation. *The Lancet* 334:834-5

145. Lorenz M, Panitz K, Grosse-Furtner C, Meyer J, Lorenz R. 1994. Lower-limb amputation, prevalence of abdominal aortic aneurysm and atherosclerotic risk factors. *British journal of surgery* 81:839-40

146. Vorp DA, Raghavan ML, Webster MW. 1998. Mechanical wall stress in abdominal aortic aneurysm: influence of diameter and asymmetry. *Journal of Vascular Surgery* 27:632-9

147. Fillinger MF, Racusin J, Baker RK, Cronenwett JL, Teutelink A, et al. 2004. Anatomic characteristics of ruptured abdominal aortic aneurysm on conventional CT scans: implications for rupture risk. *Journal of vascular surgery* 39:1243-52

148. Finol EA, Keyhani K, Amon CH. 2003. The effect of asymmetry in abdominal aortic aneurysms under physiologically realistic pulsatile flow conditions. *Journal of biomechanical engineering* 125:207-17

149. Yeung JJ, Kim HJ, Abbruzzese TA, Vignon-Clementel IE, Draney-Blomme MT, et al. 2006. Aortoiliac hemodynamic and morphologic adaptation to chronic spinal cord injury. *Journal of vascular surgery* 44:1254-65. e1

150. Rodríguez JF, Ruiz C, Doblaré M, Holzapfel GA. 2008. Mechanical stresses in abdominal aortic aneurysms: influence of diameter, asymmetry, and material anisotropy. *Journal of biomechanical engineering* 130:021023

151. Crawford JD, Chivukula VK, Haller S, Vatankhah N, Bohannan CJ, et al. 2016. Aortic outflow occlusion predicts rupture of abdominal aortic aneurysm. *Journal of vascular surgery* 64:1623-8

152. Hoshina K, Sho E, Sho M, Nakahashi TK, Dalman RL. 2003. Wall shear stress and strain modulate experimental aneurysm cellularity. *Journal of vascular surgery* 37:1067

153. Sho E, Sho M, Hoshina K, Kimura H, Nakahashi TK, Dalman RL. 2004. Hemodynamic forces regulate mural macrophage infiltration in experimental aortic aneurysms. *Experimental and molecular pathology* 76:108-16

154. Sho E, Sho M, Nanjo H, Kawamura K, Masuda H, Dalman RL. 2004. Hemodynamic regulation of CD34+ cell localization and differentiation in experimental aneurysms. *Arteriosclerosis, thrombosis, and vascular biology* 24:1916-21

155. Busch A, Chernogubova E, Jin H, Meurer F, Eckstein H-H, et al. 2018. Four Surgical Modifications to the Classic Elastase Perfusion Aneurysm Model Enable Haemodynamic Alterations and Extended Elastase Perfusion. *European Journal of Vascular and Endovascular Surgery* 56:102-9

156. Updegrove A, Wilson NM, Merkow J, Lan H, Marsden AL, Shadden SC. 2017. SimVascular: an open source pipeline for cardiovascular simulation. *Annals of biomedical engineering* 45:525-41

157. Schneider CA, Rasband WS, Eliceiri KW. 2012. NIH Image to ImageJ: 25 years of image analysis. *Nature methods* 9:671

158. Abràmoff MD, Magalhães PJ, Ram SJ. 2004. Image processing with ImageJ. *Biophotonics international* 11:36-42

159. Busch A, Hartmann E, Grimm C, Ergün S, Kickuth R, et al. 2017. Heterogeneous histomorphology, yet homogeneous vascular smooth muscle cell dedifferentiation, characterize human aneurysm disease. *Journal of vascular surgery* 66:1553-64. e6

160. Berens P. 2009. CircStat: a MATLAB toolbox for circular statistics. *J Stat Softw* 31:1-21

161. Dua MM, Dalman RL. 2010. Hemodynamic influences on abdominal aortic aneurysm disease: Application of biomechanics to aneurysm pathophysiology. *Vascular pharmacology* 53:11-21

162. Van Vickle-Chavez SJ, Tung WS, Absi TS, Ennis TL, Mao D, et al. 2006. Temporal changes in mouse aortic wall gene expression during the development of elastase-induced abdominal aortic aneurysms. *Journal of vascular surgery* 43:1010-20

163. Juvonen J, Surcel H-M, Satta J, Teppo A-M, Bloigu A, et al. 1997. Elevated circulating levels of inflammatory cytokines in patients with abdominal aortic aneurysm. *Arteriosclerosis, thrombosis, and vascular biology* 17:2843-7

164. Choke E, Cockerill GW, Dawson J, Wilson RW, Jones A, et al. 2006. Increased angiogenesis at the site of abdominal aortic aneurysm rupture. *Annals of the New York Academy of Sciences* 1085:315-9

165. Azuma J, Wong RJ, Morisawa T, Hsu M, Maegdefessel L, et al. 2016. Heme oxygenase-1 expression affects murine abdominal aortic aneurysm progression. *PloS one* 11:e0149288

166. Goergen CJ, Azuma J, Barr KN, Magdefessel L, Kallop DY, et al. 2011. Influences of aortic motion and curvature on vessel expansion in murine experimental aneurysms. *Arteriosclerosis, thrombosis, and vascular biology* 31:270-9

167. Amirbekian S, Long Jr RC, Consolini MA, Suo J, Willett NJ, et al. 2009. In vivo assessment of blood flow patterns in abdominal aorta of mice with MRI: implications for AAA localization. *American Journal of Physiology-Heart and Circulatory Physiology* 297:H1290-H5

168. Correia M, Provost J, Tanter M, Pernot M. 2016. 4D ultrafast ultrasound flow imaging: in vivo quantification of arterial volumetric flow rate in a single heartbeat. *Physics in Medicine & Biology* 61:L48-L61

169. Sangwung P, Zhou G, Nayak L, Chan ER, Kumar S, et al. 2017. KLF2 and KLF4 control endothelial identity and vascular integrity. *JCI insight* 2:e91700

170. Westvik TS, Fitzgerald TN, Muto A, Maloney SP, Pimiento JM, et al. 2009. Limb ischemia after iliac ligation in aged mice stimulates angiogenesis without arteriogenesis. *Journal of vascular surgery* 49:464-73

171. Lareyre F, Clément M, Raffort J, Pohlod S, Patel M, et al. 2017. TGFβ (transforming growth factor-β) blockade induces a human-like disease in a nondissecting mouse model of abdominal aortic aneurysm. *Arteriosclerosis, thrombosis, and vascular biology* 37:2171-81

172. Gao F, Chambon P, Offermanns S, Tellides G, Kong W, et al. 2014. Disruption of TGF-β signaling in smooth muscle cell prevents elastase-induced abdominal aortic aneurysm. *Biochemical and biophysical research communications* 454:137-43

173. Dietz HC. 2010. TGF-β in the pathogenesis and prevention of disease: a matter of aneurysmic proportions. *The Journal of clinical investigation* 120:403-6

174. Pyo R, Lee JK, Shipley JM, Curci JA, Mao D, et al. 2000. Targeted gene disruption of matrix metalloproteinase-9 (gelatinase B) suppresses development of experimental abdominal aortic aneurysms. *The Journal of clinical investigation* 105:1641-9

175. Bhamidipati CM, Mehta GS, Lu G, Moehle CW, Barbery C, et al. 2012. Development of a novel murine model of aortic aneurysms using peri-adventitial elastase. *Surgery* 152:238-46

176. Lu G, Su G, Davis JP, Schaheen B, Downs E, et al. 2017. A novel chronic advanced stage abdominal aortic aneurysm murine model. *Journal of vascular surgery* 66:232-42

177. Busch A, Holm A, Wagner N, Ergün S, Rosenfeld M, et al. 2016. Extra-and intraluminal elastase induce morphologically distinct abdominal aortic aneurysms in mice and thus represent specific subtypes of human disease. *Journal of vascular research* 53:49-57

178. Assar AN, Zarins CK. 2009. Ruptured abdominal aortic aneurysm: a surgical emergency with many clinical presentations. *Postgraduate medical journal* 85:268-73

179. Paula-Ribeiro M, Garcia MMN, Martinez DG, Lima JRP, Laterza MC. 2015. Increased peripheral vascular resistance in male patients with traumatic lower limb amputation: one piece of the cardiovascular risk puzzle. *Blood pressure monitoring* 20:341-5

180. Padilla J, Jenkins NT, Laughlin MH, Fadel PJ. 2014. Blood pressure regulation VIII: resistance vessel tone and implications for a pro-atherogenic conduit artery endothelial cell phenotype. *European journal of applied physiology* 114:531-44

181. Vernon G, Baranova A, Younossi ZM. 2011. Systematic review: the epidemiology and natural history of non-alcoholic fatty liver disease and non-alcoholic steatohepatitis in adults. *Alimentary pharmacology & therapeutics* 34:274-85

182. Flegal KM, Carroll MD, Ogden CL, Curtin LR. 2010. Prevalence and trends in obesity among US adults, 1999-2008. *Jama* 303:235-41

183. Sangha GS, Goergen CJ. 2016. Photoacoustic tomography: applications for atherosclerosis imaging. *Journal of Optics* 18:1-16

184. Wang H-W, Chai N, Wang P, Hu S, Dou W, et al. 2011. Label-free bond-selective imaging by listening to vibrationally excited molecules. *Physical review letters* 106:1-4

185. Allen TJ, Hall A, Dhillon AP, Owen JS, Beard PC. 2012. Spectroscopic photoacoustic imaging of lipid-rich plaques in the human aorta in the 740 to 1400 nm wavelength range. *Journal of biomedical optics* 17:0612091-06120910

186. Li R, Phillips E, Wang P, Goergen CJ, Cheng JX. 2016. Label-free in vivo imaging of peripheral nerve by multispectral photoacoustic tomography. *Journal of biophotonics* 9:124-8

187. Iozzo P. 2011. Myocardial, perivascular, and epicardial fat. *Diabetes care* 34:S371-S9

188. Flurkey K, Currer JM, Harrison DE. 2007. Mouse models in aging research.

189. Damen FW, Adelsperger AR, Wilson KE, Goergen CJ. 2015. Comparison of traditional and integrated digital anesthetic vaporizers. *Journal of the American Association for Laboratory Animal Science* 54:756-62

190. Nakashima Y, Plump AS, Raines EW, Breslow JL, Ross R. 1994. ApoE-deficient mice develop lesions of all phases of atherosclerosis throughout the arterial tree. *Arteriosclerosis, thrombosis, and vascular biology* 14:133-40

191. Alvarado CM, Hawley AE, Wrobleski SK, Sigler RE, Myers DD. 2011. Male mice have increased thrombotic potential: sex differences in a mouse model of venous thrombosis. *Thrombosis research* 127:478-86

192. Goergen CJ, Barr KN, Huynh DT, Eastham-Anderson JR, Choi G, et al. 2010. In vivo quantification of murine aortic cyclic strain, motion, and curvature: implications for abdominal aortic aneurysm growth. *Journal of Magnetic Resonance Imaging* 32:847-58

193. Phillips EH, Yrineo AA, Schroeder HD, Wilson KE, Cheng J-X, Goergen CJ. 2015. Morphological and biomechanical differences in the elastase and AngII apoE−/− rodent models of abdominal aortic aneurysms. *BioMed research international* 2015:1-12

194. Deán-Ben XL, Gottschalk S, Mc Larney B, Shoham S, Razansky D. 2017. Advanced optoacoustic methods for multiscale imaging of in vivo dynamics. *Chemical Society Reviews* 46:2158-98

195. Beard P. 2011. Biomedical photoacoustic imaging. *Interface focus*:rsfs20110028

196. Sangha GS, Phillips EH, Goergen CJ. 2017. In vivo photoacoustic lipid imaging in mice using the second near-infrared window. *Biomedical optics express* 8:736-42

197. Wang B, Karpiouk A, Yeager D, Amirian J, Litovsky S, et al. 2012. In vivo intravascular ultrasound-guided photoacoustic imaging of lipid in plaques using an animal model of atherosclerosis. *Ultrasound in Medicine and Biology* 38:2098-103

198. Wang B, Su JL, Karpiouk AB, Sokolov KV, Smalling RW, Emelianov SY. 2010. Intravascular photoacoustic imaging. *IEEE Journal of selected topics in Quantum Electronics* 16:588-99

199. Li R, Wang P, Lan L, Lloyd FP, Goergen CJ, et al. 2015. Assessing breast tumor margin by multispectral photoacoustic tomography. *Biomedical optics express* 6:1273-81

200. Manohar S, Vaartjes SE, van Hespen JCG, Klaase JM, van den Engh FM, et al. 2007. Initial results of in vivo non-invasive cancer imaging in the human breast using near-infrared photoacoustics. *Optics express* 15:12277-85

201. Toi M, Asao Y, Matsumoto Y, Sekiguchi H, Yoshikawa A, et al. 2017. Visualization of tumor-related blood vessels in human breast by photoacoustic imaging system with a hemispherical detector array. *Scientific Reports* 7:1-11

202. Wang Z, Ha S, Kim K. 2012. A new design of light illumination scheme for deep tissue photoacoustic imaging. *Optics express* 20:22649-59

203. Yu J, Schuman JS, Lee J-K, Lee SG, Chang JH, Kim K. 2017. A light illumination enhancement device for photoacoustic imaging: in vivo animal study. *IEEE Transactions on Ultrasonics, Ferroelectrics, and Frequency Control* 64:1205 - 11

204. Nie L, Cai X, Maslov K, Garcia-Uribe A, Anastasio MA, Wang LV. 2012. Photoacoustic tomography through a whole adult human skull with a photon recycler. *Journal of biomedical optics* 17:110506-

205. Ash C, Dubec M, Donne K, Bashford T. 2017. Effect of wavelength and beam width on penetration in light-tissue interaction using computational methods. *Lasers in medical science* 32:1909-18

206. Held G, Preisser S, Akarçay HG, Peeters S, Frenz M, Jaeger M. 2014. Effect of irradiation distance on image contrast in epi-optoacoustic imaging of human volunteers. *Biomedical optics express* 5:3765-80

207. Jaeger M, Siegenthaler L, Kitz M, Frenz M. 2009. Reduction of background in optoacoustic image sequences obtained under tissue deformation. *Journal of biomedical optics* 14:054011--10

208. Jaeger M, Bamber JC, Frenz M. 2013. Clutter elimination for deep clinical optoacoustic imaging using localised vibration tagging (LOVIT). *Photoacoustics* 1:19-29

209. Singh MKA, Jaeger M, Frenz M, Steenbergen W. 2017. Photoacoustic reflection artifact reduction using photoacoustic-guided focused ultrasound: comparison between plane-wave and element-by-element synthetic backpropagation approach. *Biomedical optics express* 8:2245-60

210. Singh MKA, Steenbergen W. 2015. Photoacoustic-guided focused ultrasound (PAFUSion) for identifying reflection artifacts in photoacoustic imaging. *Photoacoustics* 3:123-31

211. Singh MKA, Jaeger M, Frenz M, Steenbergen W. 2016. In vivo demonstration of reflection artifact reduction in photoacoustic imaging using synthetic aperture photoacoustic-guided focused ultrasound (PAFUSion). *Biomedical optics express* 7:2955-72

212. Kedenburg S, Vieweg M, Gissibl T, Giessen H. 2012. Linear refractive index and absorption measurements of nonlinear optical liquids in the visible and near-infrared spectral region. *Optical Materials Express* 2:1588-611

213. Jonasz M, Fournier G. 2011. *Light scattering by particles in water: theoretical and experimental foundations*. Elsevier

214. Weber MJ. 2002. *Handbook of optical materials*. CRC press

215. Buiteveld H, Hakvoort JHM, Donze M. Optical properties of pure water. *Proc. Ocean Optics XII*, *1994*, 2258:174-84: International Society for Optics and Photonics

216. Kaniusas E. 2015. *Biomedical Signals and Sensors II*. Springer

217. Schnepf MJ, Mayer M, Kuttner C, Tebbe M, Wolf D, et al. 2017. Nanorattles with tailored electric field enhancement. *Nanoscale* 9:9376-85

218. Kharine A, Manohar S, Seeton R, Kolkman RGM, Bolt RA, et al. 2003. Poly (vinyl alcohol) gels for use as tissue phantoms in photoacoustic mammography. *Physics in Medicine & Biology* 48:357

219. Kolkman RGM, Hondebrink E, Steenbergen W, van Leeuwen TGJM, de Mul FFM. 2004. Photoacoustic mammography laboratory prototype: imaging of breast tissue phantoms. *Journal of biomedical optics* 9:1172-82

220. Kharine A, Manohar S, Seeton R, Kolkman RGM, Bolt RA, et al. 2003. Poly (vinyl alcohol) gels for use as tissue phantoms in photoacoustic mammography. *Physics in medicine and biology* 48:357

221. Vogt WC, Jia C, Wear KA, Garra BS, Pfefer TJ. 2016. Biologically relevant photoacoustic imaging phantoms with tunable optical and acoustic properties. *Journal of biomedical optics* 21:101405

222. Wang LV, Yao J. 2016. A practical guide to photoacoustic tomography in the life sciences. *Nature methods* 13:627-38

223. Benjamin EJ, Blaha MJ, Chiuve SE, Cushman M, Das SR, et al. 2017. Heart disease and stroke statistics-2017 update: a report from the American Heart Association. *circulation* 135:e146-e603

224. Bourantas CV, Garcia-Garcia HM, Naka KK, Sakellarios A, Athanasiou L, et al. 2013. Hybrid intravascular imaging: current applications and prospective potential in the study of coronary atherosclerosis. *Journal of the American College of Cardiology* 61:1369-78

225. Bourantas CV, Jaffer FA, Gijsen FJ, Van Soest G, Madden SP, et al. 2016. Hybrid intravascular imaging: recent advances, technical considerations, and current applications in the study of plaque pathophysiology. *European heart journal* 38:400-12

226. Jansen K, van Soest G, van der Steen AF. 2014. Intravascular photoacoustic imaging: a new tool for vulnerable plaque identification. *Ultrasound in medicine & biology* 40:1037-48

227. Jansen K, van der Steen AF, Wu M, van Beusekom HM, Springeling G, et al. 2014. Spectroscopic intravascular photoacoustic imaging of lipids in atherosclerosis. *Journal of biomedical optics* 19:026006

228. Yeager DE, Karpiouk AB, Wang B, Amirian JH, Sokolov KV, et al. 2012. Intravascular photoacoustic imaging of exogenously labeled atherosclerotic plaque through luminal blood. *Journal of biomedical optics* 17:106016

229. Kole A, Cao Y, Hui J, Bolad IA, Alloosh M, et al. 2019. Comparative quantification of arterial lipid by intravascular photoacoustic-ultrasound imaging and near-infrared spectroscopy-intravascular ultrasound. *Journal of cardiovascular translational research* 12:211-20

230. Galanzha EI, Sarimollaoglu M, Nedosekin DA, Keyrouz SG, Mehta JL, Zharov VP. 2011. In vivo flow cytometry of circulating clots using negative photothermal and photoacoustic contrasts. *Cytometry Part A* 79:814-24

231. Jawad HJ, Sarimollaoglu M, Biris AS, Zharov VP. 2018. Dynamic blood flow phantom with negative and positive photoacoustic contrasts. *Biomedical optics express* 9:4702-13

232. Dana N, Di Biase L, Natale A, Emelianov S, Bouchard R. 2014. In vitro photoacoustic visualization of myocardial ablation lesions. *Heart Rhythm* 11:150-7

233. Wright M, Harks E, Deladi S, Suijver F, Barley M, et al. 2011. Real-time lesion assessment using a novel combined ultrasound and radiofrequency ablation catheter. *Heart Rhythm* 8:304-12

234. Iskander-Rizk S, Kruizinga P, Van Der Steen AF, van Soest G. 2018. Spectroscopic photoacoustic imaging of radiofrequency ablation in the left atrium. *Biomedical optics express* 9:1309-22

235. Cao Y, Kole A, Hui J, Zhang Y, Mai J, et al. 2018. Fast assessment of lipid content in arteries in vivo by intravascular photoacoustic tomography. *Scientific reports* 8:2400

236. Wu M, Springeling G, Lovrak M, Mastik F, Iskander-Rizk S, et al. 2017. Real-time volumetric lipid imaging in vivo by intravascular photoacoustics at 20 frames per second. *Biomedical optics express* 8:943-53

237. Soepriatna AH, Yeh AK, Clifford AD, Bezci SE, O'Connell GD, Goergen CJ. 2019. Three-dimensional myocardial strain correlates with murine left ventricular remodelling severity post-infarction. *Journal of the Royal Society Interface* 16:20190570

238. Cebull HL, Soepriatna AH, Boyle JJ, Rothenberger SM, Goergen CJ. 2019. Strain Mapping From Four-Dimensional Ultrasound Reveals Complex Remodeling in Dissecting Murine Abdominal Aortic Aneurysms. *Journal of biomechanical engineering* 141:060907

239. Boyle JJ, Soepriatna A, Damen F, Rowe RA, Pless RB, et al. 2019. Regularization-Free Strain Mapping in Three Dimensions, With Application to Cardiac Ultrasound. *Journal of biomechanical engineering* 141:011010

240. Seki A, Iwai K, Katagiri T, Matsuura Y. 2016. Forward-viewing photoacoustic imaging probe with bundled ultra-thin hollow optical fibers. *Journal of Optics* 18:074015

241. Cai D, Li Z, Chen S-L. 2016. In vivo deconvolution acoustic-resolution photoacoustic microscopy in three dimensions. *Biomedical optics express* 7:369-80

242. Xiong K, Yang S, Li X, Xing D. 2018. Autofocusing optical-resolution photoacoustic endoscopy. *Optics letters* 43:1846-9

243. Sangha GS, Hale NJ, Goergen CJ. 2018. Adjustable photoacoustic tomography probe improves light delivery and image quality. *Photoacoustics* 12:6-13

244. Nam D, Ni C-W, Rezvan A, Suo J, Budzyn K, et al. 2009. Partial carotid ligation is a model of acutely induced disturbed flow, leading to rapid endothelial dysfunction and atherosclerosis. *American Journal of Physiology-Heart and Circulatory Physiology* 297:H1535-H43

245. Paigen B, Morrow A, Holmes PA, Mitchell D, Williams RA. 1987. Quantitative assessment of atherosclerotic lesions in mice. *Atherosclerosis* 68:231-40

246. Cheng C, Tempel D, Van Haperen R, Van Der Baan A, Grosveld F, et al. 2006. Atherosclerotic lesion size and vulnerability are determined by patterns of fluid shear stress. *Circulation* 113:2744-53

247. Khatri JJ, Johnson C, Magid R, Lessner SM, Laude KM, et al. 2004. Vascular oxidant stress enhances progression and angiogenesis of experimental atheroma. *Circulation* 109:520-5

248. Kumar A, Lindner V. 1997. Remodeling with neointima formation in the mouse carotid artery after cessation of blood flow. *Arteriosclerosis, thrombosis, and vascular biology* 17:2238-44

249. Go Y-M, Kim CW, Walker DI, Kang DW, Kumar S, et al. 2014. Disturbed flow induces systemic changes in metabolites in mouse plasma: a metabolomics study using ApoE−/− mice with partial carotid ligation. *American Journal of Physiology-Regulatory, Integrative and Comparative Physiology* 308:R62-R72

250. Ni C-W, Qiu H, Rezvan A, Kwon K, Nam D, et al. 2010. Discovery of novel mechanosensitive genes in vivo using mouse carotid artery endothelium exposed to disturbed flow. *Blood* 116:e66-e73

251. Merino H, Parthasarathy S, Singla DK. 2013. Partial ligation-induced carotid artery occlusion induces leukocyte recruitment and lipid accumulation—a shear stress model of atherosclerosis. *Molecular and cellular biochemistry* 372:267-73

252. Korshunov VA, Wang H, Ahmed R, Mickelsen DM, Zhou Q, et al. 2017. Model-based vascular elastography improves the detection of flow-induced carotid artery remodeling in mice. *Scientific reports* 7:12081

253. Glagov S, Weisenberg E, Zarins CK, Stankunavicius R, Kolettis GJ. 1987. Compensatory enlargement of human atherosclerotic coronary arteries. *New England Journal of Medicine* 316:1371-5

254. Bonthu S, Heistad DD, Chappell DA, Lamping KG, Faraci FM. 1997. Atherosclerosis, vascular remodeling, and impairment of endothelium-dependent relaxation in genetically altered hyperlipidemic mice. *Arteriosclerosis, thrombosis, and vascular biology* 17:2333-40

255. Korshunov VA, Berk BC. 2004. Strain-dependent vascular remodeling: the "Glagov phenomenon" is genetically determined. *Circulation* 110:220-6

256. Korshunov VA, Schwartz SM, Berk BC. 2007. Vascular remodeling: hemodynamic and biochemical mechanisms underlying Glagov's phenomenon. *Arteriosclerosis, thrombosis, and vascular biology* 27:1722-8

257. Mitra R, Qiao J, Madhavan S, O'Neil GL, Ritchie B, et al. 2018. The comparative effects of high fat diet or disturbed blood flow on glycocalyx integrity and vascular inflammation. *Translational medicine communications* 3:10

258. Ternacle J, Wan F, Sawaki D, Surenaud M, Pini M, et al. 2017. Short-term high-fat diet compromises myocardial function: a radial strain rate imaging study. *European Heart Journal-Cardiovascular Imaging* 18:1283-91

259. Sangha GS, Busch A, Acuna A, Berman AG, Phillips EH, et al. 2019. Effects of Iliac Stenosis on Abdominal Aortic Aneurysm Formation in Mice and Humans. *Journal of vascular research*:1-13

260. Shin IJ, Shon S-M, Schellingerhout D, Park J-Y, Kim J-Y, et al. 2013. Characterization of partial ligation-induced carotid atherosclerosis model using dual-modality molecular imaging in ApoE knock-out mice. *PLoS One* 8:e73451

261. Millon A, Sigovan M, Boussel L, Mathevet J-L, Louzier V, et al. 2015. Low WSS induces intimal thickening, while large WSS variation and inflammation induce medial thinning, in an animal model of atherosclerosis. *PloS one* 10:e0141880

262. Foss CA, Bedja D, Mease RC, Wang H, Kass DA, et al. 2015. Molecular imaging of inflammation in the ApoE-/-mouse model of atherosclerosis with IodoDPA. *Biochemical and biophysical research communications* 461:70-5

263. Yu W, Braz JC, Dutton AM, Prusakov P, Rekhter M. 2007. In vivo imaging of atherosclerotic plaques in apolipoprotein E deficient mice using nonlinear microscopy. *Journal of biomedical optics* 12:054008

264. Wang S, Lin J, Wang T, Chen X, Huang P. 2016. Recent advances in photoacoustic imaging for deep-tissue biomedical applications. *Theranostics* 6:2394

265. Wang LV, Yao J. 2016. A practical guide to photoacoustic tomography in the life sciences. *Nature methods* 13:627

266. Jansen K, Wu M, van der Steen AF, van Soest G. 2014. Photoacoustic imaging of human coronary atherosclerosis in two spectral bands. *Photoacoustics* 2:12-20

267. Felton C, Crook D, Davies M, Oliver M. 1997. Relation of plaque lipid composition and morphology to the stability of human aortic plaques. *Arteriosclerosis, thrombosis, and vascular biology* 17:1337-45

268. Tong J, Cohnert T, Regitnig P, Holzapfel GA. 2011. Effects of age on the elastic properties of the intraluminal thrombus and the thrombus-covered wall in abdominal aortic aneurysms: biaxial extension behaviour and material modelling. *European journal of vascular and endovascular surgery* 42:207-19

269. Phillips EH, Yrineo AA, Schroeder HD, Wilson KE, Cheng J-X, Goergen CJ. 2015. Morphological and biomechanical differences in the elastase and AngII apoE−/− rodent models of abdominal aortic aneurysms. *BioMed research international* 2015

270. Cuomo F, Ferruzzi J, Humphrey JD, Figueroa CA. 2015. An experimental–computational study of catheter induced alterations in pulse wave velocity in anesthetized mice. *Annals of biomedical engineering* 43:1555-70

271. Gaddum NR, Alastruey J, Beerbaum P, Chowienczyk P, Schaeffter T. 2013. A technical assessment of pulse wave velocity algorithms applied to non-invasive arterial waveforms. *Annals of biomedical engineering* 41:2617-29

272. Humphrey JD, DeLange S. 2015. *An introduction to biomechanics: solids and fluids, analysis and design*. pp 1-692. Springer-Verlag New York. 692 pp.

PUBLICATIONS

The following list provides comprehensive view of all published manuscripts and their scientific impact as quantified by number of citations. * denotes co-first author publications.

1. Lin, J., Phillips, E., Riggins, T. A., **Sangha, G. S.***, Chakraborty, S., Lee, J., ... & Yrineo, A. (2015). Imaging of small animal peripheral artery disease models: recent advancements and translational potential. *International journal of molecular sciences*, *16*(5), 11131-11177. – Citations 18

2. **Sangha, G. S.**, & Goergen, C. J. (2016). Photoacoustic tomography: applications for atherosclerosis imaging. Journal of Optics, 18(8), 084005. – Citations 6

3. Wodicka, J., Chambers, A., **Sangha, G. S.**, Goergen, C., & Panitch, A. (2017). Development of a glycosaminoglycan derived, selectin targeting anti-adhesive coating to treat endothelial cell dysfunction. *Pharmaceuticals*, *10*(2), 36. – Citations 4

4. **Sangha, G. S.**, Phillips, E. H., & Goergen, C. J. (2017). In vivo photoacoustic lipid imaging in mice using the second near-infrared window. *Biomedical optics express*, *8*(2), 736-742. – Citations 9

5. **Sangha, G. S.**, Hale, N. J., & Goergen, C. J. (2018). Adjustable photoacoustic tomography probe improves light delivery and image quality. *Photoacoustics*, *12*, 6-13. – Citations 4

6. **Sangha, G. S.**, Busch, A., Acuna, A., Berman, A. G., Phillips, E. H., Trenner, M., ... & Goergen, C. J. (2019). Effects of Iliac Stenosis on Abdominal Aortic Aneurysm Formation in Mice and Humans. *Journal of vascular research*, 1-13. – Citations 0